SAPIENZA
UNIVERSITÀ DI ROMA

Facoltà di Ingegneria

Dipartimento di Ingegneria Civile, Edile e Ambientale

Dottorato di Ricerca in Ingegneria Idraulica

XXV Ciclo

Tesi di Dottorato

Quantitative precipitation estimates from dual-polarization weather radar in Lazio region

Coordinatore: Prof. Ing. Francesco Gallerano

Relatore: Prof. Ing. Francesco Napolitano

Correlatore: Prof. Ing. Fabio Russo

Correlatore esterno: Dott. Luca Baldini

Dottorando: Ing. Stefano Sebastianelli

Roma, dicembre 2012

Abstract

Many phenomena (such as attenuation and range degradation) can influence the accuracy of rainfall radar estimates. They introduce errors that increase as the distance from the radar increases, thereby decreasing the reliability of radar estimates for applications that require quantitative precipitation estimation. The aim of the present work is to develop a range dependent error model called adjustment factor, that can be used as a range error pattern for allowing to correct the mean error which affects long-term quantitative precipitation estimates. A range dependent gauge adjustment technique was applied in combination with other processing of radar data in order to correct the range dependent error affecting radar measurements. Issues like beam blocking, path attenuation, vertical structure of precipitation related error, bright band, and incorrect *Z*-*R* relationship are implicitly treated with this type of method. In order to develop the adjustment factor, radar error was determined with respect to rain gauges measurements through a comparison between the two devices, based on the assumption that gauge rain was real. Therefore, the *G*/*R* ratio between the yearly rainfall amount measured in each rain gauge position during 2008 and the corresponding radar rainfall amount was calculated against the distance from radar. Trend of the *G*/*R* ratio shows two behaviors: a concave part due to the melting layer effect close to the radar location, and an almost linear increasing trend at greater distance. Then, a linear best fitting was used to find an adjustment factor, which estimates the radar error at a given range. The effectiveness of the methodology was verified by comparing pairs of rainfall time series that were observed simultaneously by collocated rain gauges and radar. Furthermore, the variability of the adjustment factor was investigated at the scale of event, both for convective and stratiform events. The main result is that there is not an univocal range error pattern, as it is also a function of the event characteristics. On the other hand, the adjustment factor tends to stabilize over long periods of observation as in the case of a whole year of measures.

Sommario

Molti fenomeni (come ad esempio l'attenuazione del segnale e la degradazione in range) possono influenzare l'accuratezza delle stime radar di pioggia. Essi introducono degli errori che aumentano all'aumentare della distanza dal radar, riducendone quindi l'affidabilità riguardo ad applicazioni che richiedono stime quantitative di precipitazione. Lo scopo di questo lavoro è sviluppare un modello dell'errore variabile con la distanza detto adjustment factor, che consenta di correggere l'errore che mediamente inficia le stime quantitative di pioggia a lungo termine. L'adjustment factor è stato applicato in combinazione con altre elaborazioni di dati al fine di correggere l'errore variabile con la distanza che altera le stime radar di pioggia. Errori dovuti a blocco del fascio, attenuazione, struttura verticale della precipitazione, presenza dello strato fondente e relazione *Z-R* non corretta sono implicitamente trattati con questa metodologia. Per mettere a punto l'adjustment factor l'errore del radar è stato valutato rispetto alle misure pluviometriche mediante un confronto che si basa sull'ipotesi che la misura di pioggia fornita dal pluviometro sia reale. Quindi, il rapporto G/R fra la cumulata annuale di pioggia ottenuta in ciascun sito pluviometrico per l'anno 2008 e la corrispondente cumulata radar è stato calcolato in funzione della distanza. L'andamento trovato mostra due diversi comportamenti: un tratto concavo dovuto all'effetto dello strato fondente relativamente vicino al sito del radar e un andamento all'incirca lineare crescente per distanze maggiori. Successivamente l'adjustment factor è stato stimato fittando l'andamento di $\log(G/R)$, i cui valori sono stati convertiti in dB. L'efficacia della metodologia è stata verificata confrontando coppie di serie storiche di pioggia osservate simultaneamente dai pluviometri e dal radar. In oltre, è stata investigata la variabilità del modello di errore a scala di evento, considerando sia eventi convettivi che stratiformi. Ciò ha mostrato che non esiste un univoco modello di errore, ma esso varia in funzione delle particolari caratteristiche dell'evento. D'altra parte, l'adjustment factor tende a stabilizzarsi su lunghi periodi di osservazione come nel caso di un intero anno di misure.

Table of contents

Chapter 1

Introduction

A weather radar is able to provide, in real time and over a wide region, high spatial and temporal resolution rainfall intensity estimates. Therefore, it plays a significant role in the rainfall field estimation and consequently in the improvements of hydrograph simulation (Lopez et al., 2005), which is necessary for providing flood forecasting and forewarning (with a safety margin) and for the design of drainage systems (Clothier and Pegram, 2002).

Weather radar has been established as an invaluable tool for provision of weather services, as it facilitates monitoring of precipitation events and predicts their short time evolution. However, it is not as well established as a tool for the quantitative estimation of precipitation (Delrieu et al., 2009). Thus, for many applications (especially applications that require long-term quantitative precipitation estimates, such as those related to hydraulic risk assessment) conventional measurements from a network of sparse rain gauges are still preferred. In fact, when comparing data from rain gauges with the corresponding radar estimates, errors are found that depend on the distance of the rain gauges with respect to the radar position. Many sources of error affect radar rainfall estimates at ground level: these include radar miscalibration, range degradation (including beam broadening and sampling of precipitation at increasing altitude), path attenuation, ground clutter, instrument sensitivity, vertical variability of the precipitation system, vertical air motion, precipitation drift, temporal sampling error, anomalous propagation and beam-blocking (Brandes et al., 1999; Villarini and Krajewski, 2010). These produce an overall error, which tends to increase as the distance from radar increases. As a consequence, the spatial structure of a rain field derived from weather radar measurements, that are collected at low elevation angles, is affected by the way that the radar samples precipitation and is therefore dependent both on height and size of the radar's sample volume (which increase as the distance from radar increases) and on orography (the latter influences errors due to ground clutter and beam-blocking).

As noted above, the accuracy of radar estimates has been traditionally assessed by performing a comparison with rain gauges measurements at ground. Factors producing discrepancies between radar and rain gauge data can produce the following errors (Zawadzki, 1984): (1) random errors, such as the error associated with the transformation from reflectivity to rain rate due to the variability of drop size distribution (DSD); (2) systematic errors (Villarini et al., 2008b) due to

radar miscalibration; (3) range-dependent errors, such as sampling uncertainties associated with the beam broadening and the increase in height with range of the sample volume (Berenguer and Zawadzki, 2008; Berenguer and Zawadzki, 2009), which cause temporal and spatial sampling differences of the two devices (Villarini et al., 2008a).

Radar reflectivity factor (Z) and rainfall intensity (R) both depend on the hydrometeor water phase distribution within the sampled volume. Saltikoff et al. (2000) applied individually at each radar pixel in real time an optimal relation between the reflectivity factor and the precipitation intensity, by using water-phase adjusted radar data. Finally they compared the values of accumulated precipitation obtained from both rain gauge and radar data.

Giangrande and Ryzhkov (2003; 2005) and Wang and Chandrasekar (2010) demonstrated (at S and X-band respectively) a statistical improvement in rainfall radar estimates by utilizing polarimetric algorithms based on the specific differential phase K_{DP}-R instead of the Z-R conventional algorithm. In fact, the specific differential phase is immune to radar miscalibration, path attenuation, and partial beam-blocking and is less sensitive to drops size distribution variability, but measurement error is quite high especially for light precipitation (Vulpiani et al., 2012). To provide precipitation estimates at long ranges Giangrande and Ryzhkov (2008) investigated also the quality of polarimetric rainfall estimation at far distances from an S-band polarimetric weather radar. Recently, to overcome errors due to range degradation and attenuation, a low-power, short-range, dense radar network has been used. In particular, the dense network approach allows to the radars that comprise a network to sample at low altitude, with higher spatial resolution and increased sensitivity. Moreover, the different radar measures available can be combined to estimate the signal attenuation (Junyent and Chandrasekar, 2009).

The ratio between rain gauge readings and the corresponding radar estimates has been often employed to correct the main field bias due to uncertainties in Z-R relationship and system non-optimal calibration (Seo et al., 2000; Borga and Tonelli, 2000; Gjertsen et al., 2004; Krajewski et al., 2011). Through this technique, the mean error which affects radar rainfall accumulations with respect to the corresponding rain gauge measurements, is removed by multiplying radar rainfall accumulations by the ratio of the sum of gauge rainfall accumulations to that of radar rainfall accumulations. Then, from this ratio the multiplicative constant in the Z-R relationship is estimated (Seo et al., 2000). However, its use is reasonable only at short ranges, where the effects of range degradation are negligible, and G/R ratio is relatively low and constant, or if a dense rain gauge network is available in the radar domain.

Often rain fields are composed of a convective part and a stratiform one. In fact, during convective events, the oldest part of precipitation tends to become stratiform. In this case, there are cores of convection embedded in larger stratiform precipitation regions (Houze, 1997; Vignal et al., 2000; Zhang et al., 2008; Zhang and Qi, 2010). On the other hand, coefficients of the *Z-R* relation depend on the DSD and, therefore, they vary in time and space, as well as *Z-R* relation varies geographically depending on the type of precipitation (Koistinen and Puhakka, 1986; Saltikoff et al., 2000; Villarini and Krajewski, 2010). Thus, the error introduced by *Z-R* relationship is a random error which varies in space. Therefore, in this work, it has not been represented through an invariant with space multiplicative bias *M*, namely main field bias. But we are estimated *M* only to correct systematic error due to radar miscalibration. Moreover, rain gauge data utilized for this issue are collected only at short ranges, as detailed in Chapter 5. A further consequence is that comparison between rain gauge and radar rains at the same location depends on the selected *Z-R* relationship (Koistinen and Puhakka, 1986). If *G*/*R* ratio varies too rapidly with distance main field bias adjustment method must be coupled with a procedure for removing range-dependent bias due to non-uniform vertical profile of reflectivity (VPR). VPR is the ratio between reflectivity at a given altitude and reflectivity at the lowest elevation. Sources of non-uniform VPR are well known in the literature (Seo et al. 2000; Krajewski et al., 2011), which offers a number of procedures for real-time adjustment of range-dependent biases (Seo et al. 2000; Borga and Tonelli, 2000; Vignal et al., 2000; Vignal et Krajewski, 2001; Gjertsen et al., 2004; Zhang et al., 2008; Zhang and Qi, 2010; Krajewski et al., 2011).

The aim of the present work is to develop a range dependent error (RDE) model called adjustment factor (*AF*) that can be used as a range error pattern, which allows to correct the mean error affecting long-term quantitative precipitation estimates (QPE). Processing of data is performed by two separate analyzes. A range dependent gauge adjustment technique is applied in combination with other processings of radar data (Michelson et al., 2000; Gjertsen et al., 2004) for both analyses. Issues like beam blocking, attenuation, VPR related error, bright band, and incorrect *Z-R* relationship are implicitly treated with this type of method (Gjertsen et al., 2004). In a first analysis the *AF* represents the effects of range degradations (beam broadening and sampling precipitation at increasing altitude, which include beam overshooting and sampling of ice particles above the freezing level), as well as of other sources of uncertainties such as path attenuation, radar sampling precipitation within the melting layer, and the VPR structure. The methodology is coupled with a radar calibration performed with rain gauge data.

A subsequent analysis is performed to highlight the effect of signal attenuation. Therefore, the gauge adjustment technique is coupled with two processing of radar data, namely a procedure to remove the path attenuation, and, subsequently, a radar calibration with rain gauge, both performed before the *AF* computation, which, therefore, does not take into account the effect of path attenuation. In both analyzes, radar calibration based on rain gauges data is performed before the *AF* estimate. In the latter analysis, correction of path attenuation is carried out before radar calibration.

In order to develop the *AF*, a comparison between radar and rain gauges rainfall fields is done, based on the assumption that gauge rain is real. This hypothesis is formulated because a rain gauge can directly measure the rain, whereas a weather radar derives rain rate from back-scattered power measurements. As a consequence, radar error is determined with respect to rain gauges measurements. Then, the overall sampling radar error is estimated through the evaluation of the *G*/*R* ratio between radar estimates and corresponding rain gauge measurements against the distance from radar. Afterwards, a regression line is used to find the *AF*. Since the spatial differences between radar and rain gauges samplings (radar samples in a volume aloft while rain gauge data are collected in a point when the raindrops reach the ground) affect the comparison between the two devices, a whole year of measurements is used to estimate the *G*/*R* ratios. In fact, *G*/*R* ratio becomes more stable for longer accumulation times, because the influence of uncertainty caused by mismatches in time and space performed by the two devices is reduced (Gabella and Amitai, 2000; Gabella et al., 2001; Gjertsen et al., 2004; Ozturk and Yilmazer, 2007). Errors arising from orography are not considered.

In this way, yearly precipitation amounts (mm) obtained for each rain gauge location, are corrected. To verify the effectiveness of methodology, the correspondence between pairs of rainfall processes observed simultaneously by radar and by each rain gauge at the rain gauge position is investigated through the analysis of trend with distance from radar of Fractional Standard Error (FSE) index, slope of the scatter plots regression lines between *G* and *R* and the *G*/*R* ratio between rain gauges and radar rainfall amounts.

For this study, rainfall intensity maps, derived from reflectivity measurements collected with the Polar 55C weather radar in 2008 and 2009, are utilized. The radar calibration is performed by using only year 2008 radar and rain gauge data sets, as well as the *AF* estimate.

To verify the effectiveness of the methodologies, the synthetic index, the slope of the scatter plots' regression lines and the *G*/*R* ratio behaviours are analysed in dependence on the distance, for both the 2008 data sets and for 2009 data sets. In particular, for the second methodology,

only rain gauges approximately aligned along a radius are chosen, and events are selected so that the path from radar to the rain gauges is always located in a very intense rainy area. In this way, an optimal rain gauge network configuration for emphasizing the effects of the signal attenuation is carried out.

Finally, the *AF* variability depending on the event type is investigated at the scale of event. Initially, the rainfall events collected by Polar 55C during the 2008 – 2009 period, are split into convective and stratiform cases, through a Radar Convective Parameter (*RCP*) which takes into account the distribution of the VPR that characterizes each type of event (Steiner et al., 1995; Bechini et al., 2012). All the events are chosen in such a way that the rain field covers the whole radar scanning area so that each rain gauge available is able to record rainfall. As a consequence, despite several convective events are recognized (following the method above mentioned) during the summer season, we did not considered them because they are formed by few isolated rain cells. However, the methodology above explained allows to classify as convective others events that occur during cold season. Investigating these events, we found that they are frequently formed by young cores of convective precipitation embedded into very wide stratiform rain areas, as it is largely confirmed in the literature. Conversely, a stratiform rain field is almost homogeneous (Yuter and Houze, 1995; Houze, 1997; Vignal et al., 2000; Zhang et al., 2008; Zhang and Qi, 2010).

1.1 – Thesis outline

Chapter 2 deals with origin of precipitation and devices able to measuring it. Moreover, the distinction between convective and stratiform events is introduced. In Chapter 3 radar meteorology principles are explained. Chapter 4 is a review of the different sources of uncertainties affecting radar-based estimates of rainfall. In Chapter 5, features of Polar 55C weather radar are described, as well as the used procedure for estimating rainfall from reflectivity maps. Chapter 6 presents the methodologies for RDE estimation by defining the *AF*. In Chapter 7 the adjustment procedures are verified, and the *AF* variability is investigated at the scale of event. Finally, Chapter 8 summarizes the results and presents guidelines for further developments.

Chapter 2

Origin and measurement of precipitation

2.1 – The atmosphere

The atmosphere is the envelope of gas that envelops the earth's surface. It consists of a mixture of many gases including nitrogen (78%), oxygen (21%), argon (1%), water vapor (0 – 7 %), ozone (0.02 – 0.01 %), and carbon dioxide (0.01 – 0.1 %).

The density of the atmosphere decreases with altitude up to about absolute vacuum of space. But the characteristics of that envelope of gas depend on the altitude. As a consequence, taking into account the temperature, the chemical composition, the air motion and the air density, the atmosphere can be divided into five main layers: Troposphere, Stratosphere, Mesosphere, Thermosphere and Exosphere.

In the Troposphere are concentrated about the 3/4 of the whole gaseous mass. The Troposphere also contains almost all the water vapor. It is the layer where the most weather effects occur, due to the movement of air masses, caused by the solar radiation.

The Troposphere is mainly warmed by the earth, which is warmed in turn by the sun. It follows that in it the temperature decreases with altitude, with a mean vertical gradient of 6.5°/1 km. The temperature becomes constant when it reaches about -55 °C in the Tropopause, that is the zone that separates the Troposphere from the Stratosphere. The Tropopause altitude depends on the latitude, and, therefore, on the amount of heat to be dissipated received from the sun, which is greater at the equator and lesser at the poles. Hence, at the poles the Tropopause is situated at an altitude of about 5-6 km, whereas close to the equator it can reach an altitude of 10-12 km.

The Stratosphere is situated above the Tropopause. Within it the temperature rises with altitude, due to the dissociation of ozone (into molecular and atomic oxygen), which interacts with ultraviolet radiation. Since gases become less dense when both their temperature increases and their pressure decreases, in the upper part of the Stratosphere there are the lighter gases, whereas heavier ones are located in the lower (equilibrium condition very stable). Therefore, the vertical air motions are almost nonexistent. It extends up to an altitude of about 50 km, where the temperature is close to that of the earth surface. Above the Stratosphere there is the Stratopause, which is the zone that separates the Stratosphere from the Mesosphere.

The Mesosphere extends from about 50 km to about 80 km in altitude. It is very rarefied and it contains the lighter gaseous elements. In the Mesosphere the temperature decreases as the altitude increases up to about 80 km, where it reaches a minimum value, which ranges from -70 to -90 °C.

The Thermosphere is situated between the Mesosphere and the Exosphere, and it extends up to 500 km altitude. This region essentially consists of hydrogen and ions produced by low wavelength radiations. It is characterized by a continuous increase in temperature with height (up to hundreds of degrees) due to the absorption by ions of the radiations.

The Exosphere is the outermost layer of the atmosphere. Within it gaseous particles are dispersed in space because they exceed the escape velocity (11.2 km/s). Generally the lighter elements (hydrogen and helium) leave most frequently the atmosphere. The atmosphere ends when its density being equal to that of interstellar space (2000-2500 km above the earth's surface).

2.2 - The energy balance

Most of the energy necessary to the natural phenomena that occur on the earth's surface or in the atmosphere is provided by solar radiation. The solar energy reaching the earth is distributed between atmospheric and oceanic circulation, and then it is radiated back to outer space. Therefore, the earth is in a situation of energy balance, because the amount of energy absorbed is equivalent to the amount of energy radiated in outer space. The intensity of solar radiation depends on the thickness of the atmosphere traversed by the rays, the earth-sun distance, and the orientation of the earth's surface. It is reduced when the rays pass through the atmosphere both by absorption and by diffusion. This reduction increases as the thickness of the atmosphere traversed by the rays increases and as its transparency decreases. Moreover, the absorption depends also on the wavelength. The ultraviolet radiation is almost completely absorbed by the ozone. Instead, the infrared is absorbed by water vapor. Nevertheless, a high fraction of solar radiation (especially in the visible spectrum) reaches the earth's surface. As a consequence, the ground is heated, and in turn emits radiant energy (whose spectrum lies almost entirely in the infrared). Water vapor and carbon dioxide content in the atmosphere absorb infrared radiation. So, only a little part of the energy radiated by the earth is lost in space. Therefore, the atmosphere absorbs radiant energy from both the sun and the earth, and it warms emitting energy partly to the earth and partly to the space. As a consequence, the earth's surface warms more than it would in the absence of atmosphere, because it receives heat from both the sun and the atmosphere. Hence, the earth's surface must reach a temperature higher than that which would

have in absence of atmosphere in order that it maintains thermal equilibrium. This causes the greenhouse effect that enables life on earth's surface.

Energy exchanges also take place between areas of the earth at different temperatures. There is in fact a flow of energy from the areas which receive more radiant energy to those who receive less. Due to the solar radiation, the tropics receive throughout the year an amount of energy greater than the temperate zones, which in turn receive more energy than polar regions. Therefore, tropical regions reach highest temperatures, and in consequence, they emit towards space an amount of energy greater than that emitted by the other regions, but lesser than the received energy. Consequently, there is an energy flow from tropical to polar regions. The energy flow from equator to polar regions is intensified in the winter months, when the thermal imbalance is greater. For this reason meteorological phenomena are generally more intense in winter.

2.3 - Atmospheric currents

The water and the atmosphere are present on the surface of the earth in the form of thin layers. They are able to redistribute on the surface of the earth the energy that it receives from the sun. The water forms the oceans that cover more than two-thirds of the planet's surface. The atmosphere is a thin layer of gas, which remains nearby to the ground because of the earth's gravitational field. Therefore, the transport of heat from equatorial to polar zones is due to both atmospheric and marine currents. The atmospheric currents carry about 85% of the total heat in the form of sensible heat and latent heat of the air water vapor. Sea currents carry the remaining 15% of the total heat.

Atmospheric circulation can be divided into general circulation (which presides over the balance of the pole-equator thermal gradient) and secondary circulation (at local scale).

For each hemisphere, the general circulation in turn can be divided into three large macrocells: the Hadley cell (which extends from the equatorial up to the tropical region), the Ferrel cell (which is present in the middle latitudes), and the polar cell (which extends from the pole to the respective polar circle). Each of these cells interacts with the neighboring through the exchange of air masses at different temperature and humidity.

Atmospheric currents consist of vertical air motions (or convection currents) and horizontal atmospheric currents (or advection currents). A pressure difference between two points that are located at the same height causes a horizontal atmospheric current. Vertical air motions depend on the atmospheric instability that depends on the temperature distribution in the atmosphere

(that is on the heat exchanges). The air that rises is subject to decreasing pressures, for which it expands and cools. At the contrary, the air moving down compresses and heats.

An air mass is stable if it assumes a lower temperature than that of the surrounding air when it moves upwards (and therefore it assumes a greater density). Hence, it tends to return to the starting position. Instead, an air mass is unstable if it assumes a greater temperature than that of the surrounding air when it moves upwards (and therefore a lesser density). So, it tends to move away from its original position and it move further upwards. It is necessary that the air is saturated with water vapor so that the condensation occurs and the clouds can be grow. So, in case of atmospheric instability, the rising air is subject to lower pressures thus it expands and cools. Moreover, when the temperature decreases a condensation occurs with the transfer of latent heat of evaporation to the atmosphere.

2.4 - The precipitations

In Meteorology the term precipitation means the transfer of water (in liquid or solid) from the atmosphere to the ground (rainfall, snowfall, hailstorm, dew, frost etc.).

The water vapor condenses under any of the conditions of saturation, that is through cooling of moist air, or through moistening of an air mass, or if both phenomena occur (Chow et al., 1988). The water vapor condenses when the relative humidity reaches the unit value. Indeed the condensation can begin before saturation as long as the water vapor is in contact with submicroscopic solid particles (whose dimensions range from 10^{-3} µm to 10 µm) aloft. So, very small drops form, whose diameter ranges from 10 to 20 µ.

The increase of the relative humidity of the air may depend on two causes:

- the increasing of absolute humidity of the air, which causes fogs due to evaporation above the sea surface or, generally, above bodies of water warmer than the air, whose temperature is not sufficient to maintain in the form of water vapor the water which evaporates;
- the decreasing of the air temperature due to the contact with cold surfaces, or due to the mixing with cooler air, or alternatively for raising and expansion of the air.

In the latter case if only the air that is in immediate contact with cold surfaces cools it would have dew or frost. Instead, if the entire layer of air cools, fog is generated when cooling takes place near the ground, or alternatively stratiform clouds are mainly generated when the phenomenon occurs aloft.

When the air cooling is caused by the expansion (due to the lifting) clouds form. The clouds are

collections of microscopic particles of water in the liquid or solid state suspended in the atmosphere and transported by air motions (updrafts). The droplets are due to the water vapor condensation. The water vapor is generated by the water evaporation on the earth's surface (contained in bodies of water, such as the seas, the lakes, the rivers, etc.), due to the solar radiation, which causes an increasing of the earth's surface temperature.

Two kinds of rainfall events mainly exist:

- convective events;
- stratiform events.

2.4.1 - Stratiform events

Stratiform precipitations occur generally whenever there is a saturated upward air motion, which induces vapor deposition onto the ice particles which grow in the upper levels. But the updraft must be weak enough to allow ice particles to fall out while they grow. The definition of stratiform precipitation is based on the vertical air motion velocity. Stratiform conditions are present when (Yuter and Houze, 1994; Steiner et al., 1995):

$$|w| << |V_{ice}| \qquad (2.1)$$

where w is the vertical air velocity, and V_{ice} is the terminal fall speed of ice crystals and snow particles (~ 1-3 m s^{-1}). If this condition is not verified the precipitation is considered as convective. Under this condition, ice particles in the upper levels of the clouds must fall, because the vertical air motions are too weak to keep aloft them. When the particles drift down from upper levels, they melt and fall to the earth's surface as raindrops, although, under certain cold conditions, they can reach the surface exclusively as snow. In particular, stratiform precipitations occur in midlatitude cyclones, where ice particles grow predominantly by vapor deposition in a stable nimbostratus cloud layer, due to the widespread lifting in the regions of large-scale warm advection, which is concentrated in the vicinity of fronts.

Stratiform precipitation is fairly homogeneous in the horizontal, giving it a layered structure in vertical cross sections of radar reflectivity (see Chapter 3). In particular, it often (depending on the vertical profile of temperature) exhibits a pronounced layer of high reflectivity called the "bright band," which identifies the layer where the ice particles are melting while they fall toward the ground (Battan 1970; Houze 1993; Steiner et al., 1995; Houze, 1997).

Figure 2.1 shows a rainfall field of a stratiform event which occurred on 7 March 2008, and collected by the Polar 55C weather radar. It can be to note the bright band disguised as a ring of

high rainfall rate placed at a certain distance all around the radar location, depending on the elevation angle.

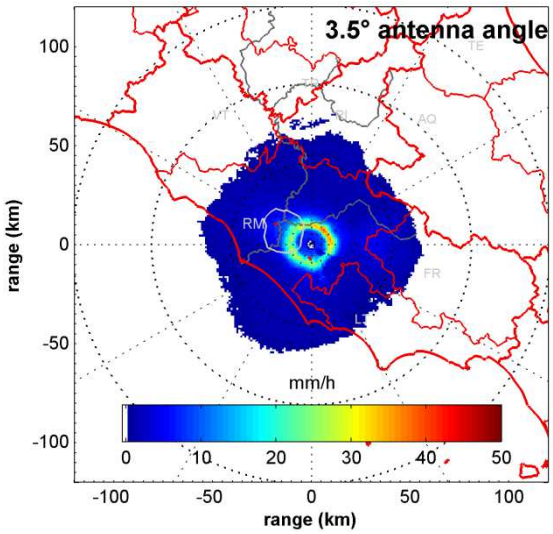

Figure 2.1 – PPI collected by Polar 55C weather radar during the stratiform event of 7 March 2008 at 3.5° elevation.

However, radar echoes are stratiform also in regions of older convection, where the vertical air motions are generally weaker, and the precipitation particles drift downward, while their mass increases by vapor diffusion. Thus, stratiform precipitations occur in older, less active convection regions that are adjacent to regions of younger convective showers. These regions typically have radar echoes formed by convective rain alongside stratiform precipitation, the latter covering great areas (up to 100 km or more) with weak horizontal gradients (weak and almost uniform reflectivity areas) and/or a bright band. Therefore, into the same convection-generated cumulonimbus cloud system there are both stratiform and convective precipitation areas (Yuter and Houze, 1994; Houze, 1997). Examples of events occurring as cores of convective precipitations embedded into a widespread stratiform precipitation area are discussed in Chapter 7.

2.4.2 – Convective events

Convective precipitations processes differ sharply from stratiform processes. The vertical air motion ranges from 1 to 10 m s^{-1} or more (Steiner et al., 1995; Houze, 1997) and is required to neutralize an unstable vertical distribution of moist static energy. In young, vigorous convective regions of the cumulonimbus, the particles fall out in heavy showers, which correspond to radar echoes consisting of localized patches of intense radar reflectivity, named cells. In a vertical

cross section, a cell is a tall, and thin column of high reflectivity. Since the greater rainfall rate, convective events are characterized by duration less than the duration of stratiform events. Moreover, convective processes are localized to restricted areas. So, the bulk of the precipitation mass falls out within a few kilometers from the updraft centers (Houze, 1997; Moisello, 1999). Figure 2.2 shows a rainfall field of convective events which occurred on 31 July 2008, and collected by the Polar 55C weather radar.

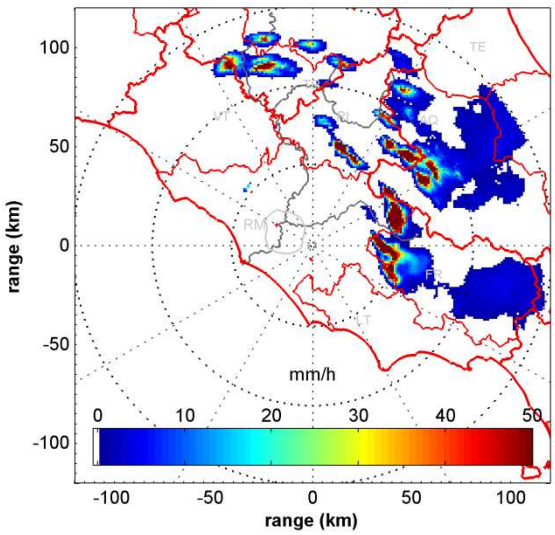

Figure 2.2 - Typical warm rain cells detected by the Polar 55C weather radar the 31 July 2008 at 1.5° elevation.

By observing Fig. 2.2, it can be noted that the convective region appears in the radar echo as a field of localized rain rate maxima.

2.4.3 – Rain cell

The solar heating, the moisture in the air and the presence of relatively cold air in the upper layers of the Troposphere contribute to the development of a storm cell.

The solar radiation causes the soil heating. Therefore, the layer of air in contact with the soil warms. Since warm air is lighter than cold air, the hot and humid air moves upwards generating an updraft. While the hot and humid air moves upwards it expands and cools adiabatically (adiabatic expansion) by about 1°C/100 m, reaching the saturation point. So, the water vapor is transformed into a myriad of minute water droplets that float in the air, forming the clouds. If the temperature is particularly low, microscopic ice crystals are formed.

The condensing water vapor transfers latent heat to the surrounding air. Therefore, the cooling of the air decreases as the altitude increases. Consequently, the acceleration of the updraft (which

holds in suspension the microscopic droplets and the ice crystals of the cloud) decreases as the altitude increases.

For convective events, the acceleration of the updraft due to the condensation of the water vapor causes a warm-humid current of air from the surrounding, that enters the cell from below. This current is said inflow, and it becomes the updraft. The rising of the hot and humid air lead to the formation of a cumulonimbus (typical thundercloud shaped towering with vertical development). Due to the updraft the cloud can reach a maximum altitude of about 7-9 km depending on the thickness of Troposphere, which in turn depends on the latitude. The humid air in lifts transfers all its latent heat, reaching thermal equilibrium with the surrounding air. In this way it becomes heavier than warmest air masses coming from below. That causes currents that move downwards, which are said downdraft.

The minute water droplets forming the clouds have a diameter not exceeding 0.1 mm, whereas the raindrops can reach a diameter of 6 mm or more (see Sect. 3.4.4). To begin the precipitation, the droplets forming the clouds have to increase their mass reaching the raindrops dimensions. In convective regions of the cumulonimbus, precipitation particles increase their mass mainly by collection of cloud water. The larger drops and/or ice particles sweep out the cloud water in their fall paths, and the particles fall out in heavy showers. This process is known as coalescence or riming for growing water drops or in the case of collection by ice particles, respectively. Whereas, if the vertical air motions are weaker, as in stratiform precipitations, the ice particles in the upper level of the clouds cannot be suspended aloft by the air motions. Hence, the growth of the precipitating particles occurs when they are falling. At higher levels the ice particles increases their mass by vapor diffusion. At lower altitudes aggregation or riming can occur (Steiner et al., 1995; Houze, 1997).

Until to the updraft is able to keep aloft the particles, they tend to increase their dimensions and weight. When the weight of the particles exceeds the aerodynamic resistance due to airflow, the raindrop fall from the cloud originating the rain. The precipitating particles originate the cold downdrafts, which tend to eliminate updrafts. When this happens the cloud dissolves starting from the top, and the temperature of the cloud tends to assume the same value of the surrounding air.

The rain cell is divided into three regions: the inflow region (close to the ground, where warm moist air is drawn through the cell), the uplift region (in the central part, where moisture condenses while the air rise up, resulting in the precipitation), the out flow region (in the upper part, where the outflow of the cold and dry air occurs). Outside the cell the air descends over a

wide area, draws moisture and enters into the cell again from below. Figure 2.3 shows the storm cell pattern.

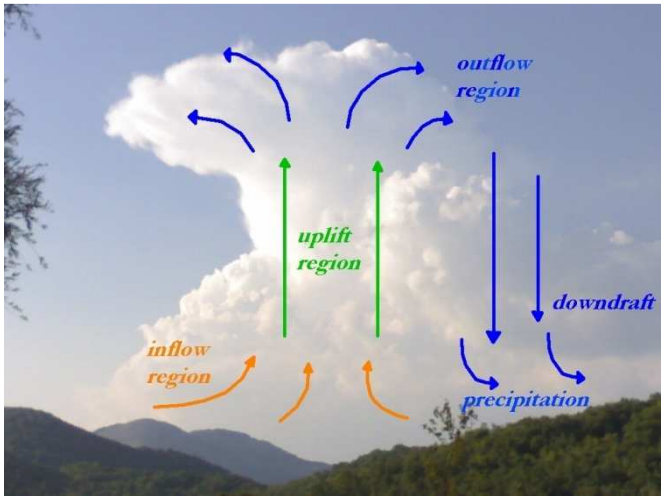

Figure 2.3 – Storm cell pattern with a cumulonimbus, which is the typical storm cloud.

The extension of a rain cell ranges from 10 to 30 km^2, while their duration can be up to 30 minutes. The storm cells tend to cluster together, since new cells tend to form in the immediate vicinity of preexisting cells (Amorocho and Wu, 1977). The cold air which descends from the active rain cell causes the development of a new storm cell. Each new cell grows in front of the oldest cell and it develops when the latter is originating the rain. The cells are localized along the wind direction, and they develop along a line of thunderstorms.

Within a storm cell the rain rate assume the greatest values in small areas. But it decreases as the distance from the point of highest rain intensity increases.

The initial lifting of the moist air may be caused by the presence of a front, by the presence of reliefs or by convective motions. Therefore, frontal storms, orographically enhanced storms and typical warm rain cells can occur.

An air mass is said cold (warm) if it has a temperature lower (higher) relative to that of the adjacent air mass. When two air masses having different origin (i.e. with different temperature and humidity) are in contact a weather front occurs. There are three types of fronts: warm front, cold front, and occluded front. Each front follows the previous by rotating around the centers of low pressure. There is a warm front when a mass of relatively warm and moist air reaches a mass of more cold and dry air, that is heavier and more stable. Warmer air tends to overcome the colder. Clouds ahead of the warm front are mostly stratiform, and rainfall gradually increases as the front approaches. If the warm air mass is unstable, thunderstorms may be embedded among

the stratiform clouds. There is a cold front when a mass of relatively cold air reaches a mass of more warm air. The cooler air is wedged below the warmest, which is raised triggering the convective motion that will lead to the formation of thundercloud. Due to the turbulence, cumulonimbus form at low altitude, and close to the front. So, heavy but short duration rains are generated. Typically, a warm front is followed by a cold front. Since the cold front moves faster than the warm front, the two fronts tend to join toward the center of cyclonic area, originating an occluded front. In this case, initially the persistent and low intensity rain of the warm front occurs, which can saturate the stratums. Then, heavy rain occurs due to the cold front, which results in a large surface runoff due to imbibition of the ground.

The typical warm rain convective cells are caused by a strong solar heating of a limited portion of territory during daylight hours. These storms affect restricted areas and have a short duration and their origin is typical of the most common summer storms.

The orographically enhanced precipitations are generated by a forced lifting of a mass of warm and moist air pushed by the prevailing winds close to the mountains. They are located along the mountain ranges, where they cause severe turbulence and strong precipitations.

2.5 - Traditional devices for measurement of precipitation

Rain gauges are traditional devices for measurement of the rainfall amount. A rain gauge is used to collect rainfall and to measure its volume reported at a height in mm and a surface area of 1 m^2. The rain gauges collect necessarily water falling on a surface of very small size. Thus, the traditional precipitation measurements are point measurements. The position of the device must be carefully chosen to avoid that, in the presence of wind or in the presence of trees or buildings, the rain gauge measurements can be distorted, so that the precipitation intercepted by the rain gauge can be different from the effective precipitation.

Since the characteristics of a recipient influence the amount of water that it has collected, the characteristics of the rain gauges are standardized.

There are various types of rain gauge according to the type of measurement to be carried out. The ordinary rain gauge measures the height of precipitation in a fixed time interval equal to one day (Calenda and Margaritora, 1993). The measurement is carried out every day at 7 am by an operator who empties the rain gauge. In this way we obtain the daily rainfall amount (mm). However there is not information about the distribution of the precipitation in such a period of time.

Recording rain gauges allow the continuous recording of the precipitation. In this way it is possible to know the distribution and the duration of any precipitation over a fixed period of time. It is thus possible to calculate the mean rain rate, which is considered instantaneous when the time interval of measurement is very short. A recording rain gauge is equipped with a sensor that detects at each instant the rain amount and a recording apparatus. The support on which data is recorded can be paper or, more frequently, magnetic. There are two types of pluviographs: the tilting siphon rain gauge and the tipping bucket rain gauge.

Due to particular environmental conditions, if it is not possible to perform measurements in the short period, totalizer rain gauges are used, which are able to collect and detain precipitation relating to a very long period of time (ranging from several months up to a year).

As above-mentioned, the observations done by a single rain gauge are representative of a restricted area at around of the instrument. So, to evaluate the rainfall amount over an extended surface, it is necessary to install many instruments (Moisello, 1999). The position of the instruments must be carefully chosen to reduce their number and to make the measurement as much as possible independent from the surrounding environment. The number of the rain gauges depends on the precipitation distribution according also to the type of study to be carried out. Obviously, the number of the devices affects the accuracy of the estimate of rain. The accuracy about the knowledge of the precipitation distribution depends on the rain gauge network density, and also on the non-uniformity of the rain gauge network, as there are various types of rain gauges as above mentioned. Particularly, the density of the rain gauge network must be greater in areas where usually heavy rainfall occurs. In fact, very intense and of short duration rains affecting an area much smaller the greater is the intensity of rain, and are the main cause of floods in small size basins, as in mountain areas.

2.6 - The weather radar

Despite all the efforts made to improve the performance of a rain gauge network, an intrinsic limit of these devices remains: the punctual data. In most of the points of a catchment basin precipitation is not measured through a rain gauge. As a consequence, to obtain pluviometric data in these points, interpolation methods have to be applied, starting from measurements referred to points very distant among themselves. Moreover, a lot of atmospheric phenomena, can be represented at the convective scale (0.2-20 km), or at the mesoscale (20-2000 km), and are too little wide to be studied through synoptic surfaces or observations in the high atmosphere. But they are too much wide to be observed locally (Houze, 1993). Therefore, at these scales, it

is necessary to use the weather radar, which can provide, in real time and over a wide area (at the mesoscale), measurements of the rainfall rate with high temporal and spatial resolution (at the convective scale). Its main advantage is the possibility to acquire tridimensional data; in fact, it is possible to monitor a volume until to 200 km from radar and up to a height of 10 km above the ground within few minutes.

The word radar is an acronym for radio detection and ranging. The weather radar is an electronic device which is able to radiate one electromagnetic pulse every T_R seconds (Battan, 1970; Peebles, 1998). The reciprocal of the pulse interval T_R is the pulse repetition frequency (PRF), defined as follows:

$$f_R = 1/T_R \tag{2.2}$$

This sequence of pulses is named the radar beam, and it is transmitted through a region of the free space defined by a beam solid angle Ω. This sequence of pulses interacts with a certain number of objects, which reflects the radio waves. In radar meteorology the word object indicates anything in the atmosphere, which backscatters toward a receiver a detectable quantity of radio energy (Russo, 2004). In the case of weather radar these objects are the hydrometeors (raindrops, snowflakes, hail or graupel). The targets scatter the energy in all directions. But a target reflects some of the wave's energy also back toward the radar receiver, which develops the received signal obtaining information about the intercepted targets.

The radar is born for belligerent aim during World War II, but then was utilized also in others fields, for instance in meteorological field. Due to the weather radar, it can be possible to observe in real time the structure of the precipitation field, with high both spatial and temporal resolutions. The radar allows also detecting phenomenon very localized, such as the storm cells. Moreover, the storm cells can be monitored identifying the regions that could be interested by precipitation in nearby future.

2.7 – Weather radars' features

The more typical types of weather radar is certainly the monostatic, that is a surface-based radar that have a single antenna located on land, which is used both during transmission and receiving.

The monostatic pulsed radar is most widely used. In this case, the radar is formed by: a transmitter, which produces the radio energy; an antenna, which irradiates the energy and intercepts the back-scattered power; a receiver, which pick up, amplifies and convert the received signal; a radar display, which is a device utilized for visual presentation of

target information to an operator, and a mass memory to the storage of data. When the transmitter is fired, a duplexer routes the high power pulse to the antenna. It also protects the receiver from the transmitted power. In particular, the antenna is a reciprocal device, which, during transmission, functions as a transducer, converting the electrical waveform from the transmitter to an electromagnetic wave for transmission. On reception, the antenna performs the inverse function. It converts the arriving electromagnetic wave into an electrical waveform (Battan, 1970; Peebles, 1998; Bringi and Chandrasekar, 2001).

The Pulse Repetition Frequency ranges from 1500 up to 30000 MHz or more. Each pulse move away from radar location at a speed, which depends by the refractive index n_r of the medium in which the pulse propagates. The medium is the atmosphere, and the propagation velocity is close to the speed of light in vacuum *c*, that is about $3 \cdot 10^8$ m/s (see Chapter 3).

The weather radars' wavelengths belong to the band of frequencies of the microwaves (3, 5 or 10 cm, corresponding to the X, C, and S-band respectively, which are the most common wavelengths).

Frequence (Ghz)	Wavelength (cm)	Band
12 – 40	0,75 – 2,5	K
8 - 12	2,5 – 3,75	X
4 - 8	3,75 – 7,3	C
2 - 4	7,5 – 15	S
1,5	20	L

Table 2.1 - Wavelengths and corresponding frequencies for weather radars.

Furthermore, the smaller the sizes of the particles, the shorter the wavelength necessary to detect them (see Sect. 3.1). Therefore, the wavelengths are chosen based on the objects to detect. For example, an S-band radar can usually detect the raindrops, but not the droplets that compose the clouds. Whereas, a K-band radar can detect many clouds without precipitations (Battan, 1970).

An important feature of weather radar is the maximum distance, which is defined as the product between the half time interval between two consecutive pulses multiplied by the speed velocity *c*. At this distance the objects can be detected only if they radiate a sufficient power to be detected (Battan, 1970).

Only the targets should interact with the pulses. But the pulses weaken when they propagate in the atmosphere, having a phenomenon which is said the signal attenuation. The longer the path of

the signal through the precipitation, the greater the attenuation. Furthermore, the higher is the rainfall rate, the greater is the attenuation. The signal attenuation causes a rainfall underestimation by the radar, especially very far from its location or in cases of heavy rainfall (Sect. 4.2.8).

Due to the signal attenuation and to the geometric effect (Sect. 3.2), the part of the incident power, which is reflected by the hydrometeors toward the receiver, is very little. For this reason, an important feature of a radar receiver is the least detectable signal over the noise level, which is the so-called minimum detectable signal (Sect. 5.4), which must be as low as possible. The minimum detectable signal ranges from 10^{-12} to 10^{-13} W for most of receivers, whereas the transmitted power is about 100 kW (Battan, 1970).

Others features are the antenna aperture, and the antenna elevation angle. The narrower the beam, the lesser the antenna aperture. Therefore, the narrower the beam, the better the resolution of the measures. However, narrow beams have the disadvantage to scan only a small part of the target in a certain time interval. As a consequence, the better shape of the radar beam depends on the purpose of the measure, and it is a function of the shape, the dimension of the antenna, as well as the wavelength (Battan, 1970).

Therefore, radar detects the presence of a target by measuring the power back-scattered. The target position is retrieved in terms of azimuth (coinciding with the direction of the radar beam) and range, which is defined as follows:

$$r = c\tau_i / 2 \qquad (2.3)$$

where τ_i is the time between the transmission of the signal and the reception of the corresponding echo, and c is the speed of light. Important parameters of the received echo are:

- the received power, which depends on the reflectivity (see Chapter 3);
- the frequency variation due to the Doppler effect, from which the radial velocity of the target is obtained;
- the signal polarization, from which the shape and the spatial orientation of the target can be retrieved.

Conventional radar, named also non-coherent, measures only the range and the reflectivity factor (Z). A Doppler radar is able to measure also the radial velocity (V_r), which is the component of the target's velocity along the radar beam. V_r is calculated based on the difference between the frequency of the transmitted pulse and the frequency of the corresponding echo. Polarimetric radars provide also information about the signal polarization, and operate with wavelengths ranging from 1 to 30 cm (usually 3.5 or 10 cm).

The lesser the wavelength λ, the greater the sensitiveness with regard to the lower reflectivity values. Therefore, the lesser the wavelength, the greater the interact between the radar beam and the hydrometeors, and the lesser the antenna diameter needed to concentrate power in a narrow beam. However, the lesser the wavelength, the greater the signal attenuation. Vice versa, if greater wavelengths are utilized (in order to reduce the attenuation), to have a good resolution, it need to utilize most wide devices. The 10 cm wavelength (S-band) represents the shorter wavelength for which the attenuation is almost negligible. But to concentrate a power with λ = 10 cm, a very wide parabolic antenna occurs (almost 8 m diameter). So, the radar is voluminous and expensive (see also Sect. 3.3). Therefore, X-band or C-band radars are often employed, with wavelengths about to 3 cm and 5 cm respectively. S-band, C-band or X-band radars can detect precipitations at distances of 200-300 km from the radar location, but good reliability of the measures can be obtained until to a distance of 100-150 km from the radar. Radars with wavelengths ranging from 1 to 8 mm also exist, which are useful to detect the droplets which compose the clouds. However, these bands cannot be utilized to study the intense precipitations, because they are too much subject to attenuation.

2.8 - Radiant energy from a radar antenna

A radar antenna is a fine cylindrical electric wire, which length is equal to the half wavelength of the electromagnetic waves transmitted by the radar. Inside the antenna, current, voltage and electric charge density oscillate at the frequency *f* of the generated electromagnetic waves. As a consequence, the electric field (**E**) intensity and the magnetic field (**H**) intensity oscillate with the same frequency (see also Sect. 3.4.1).

The magnetic streamlines are circumferences that lie in orthogonal planes with respect the antenna, and that are concentric to it, whereas the electric streamlines lie on the antenna plane, and are symmetric with respect it. As a consequence, the electric and the magnetic fields are always orthogonal among themselves. The energy divides between electric and magnetic fields. In particular, when the electric flux reaches the maximum value, all the energy is in the magnetic field. But, when the potential difference is maximum all the energy is in the electric field.

Moreover, part of the energy is irradiated, and a negligible quantity is dispersed in the antenna in the form of thermal energy. The energy irradiated during each cycle is lesser than the energy in the induction field, which intensity decreases quickly as the distance from the antenna increases. The radiation fields are the radiated parts of the electric and magnetic fields. The radiation fields propagate over long distances in all directions all around the antenna, and the intensities of the

electric and magnetic fields is in inverse relation to the square of the distance from the antenna. The wavelength of the transmitted pulses is:

$$\lambda = {}^{c}\!/_{f} \qquad (2.4)$$

where f is the frequency of both intensity and direction of the antenna fields. The electric and magnetic fields remain orthogonal among themselves. The magnetic streamlines remain both circular and concentric to the antenna. Moreover, they lie on planes that are perpendicular to the antenna, whereas the electric streamlines lie on the antenna plane. In each point of the space, the amplitude of **E** and **H** are sinusoidal quantities. Moreover, **E** and **H** are orthogonal among themselves, and both are orthogonal to the direction of propagation, along a ray.

Each field periodically originates the other one, and they propagate together (Battan, 1970).

Chapter 3

Radar meteorology principles

3.1 – Radar range equation

Weather radar allows detecting a rainfall event in real time, providing a quantitative estimation of rainfall that derives from certain variables that it can measure. A fundamental component of weather radar is the antenna. The radar antenna is a reciprocal device. During transmission the antenna functions as a transducer, converting the electrical waveform from the transmitter to an electromagnetic wave for transmission. On reception the antenna converts the arriving electromagnetic wave into an electrical waveform.

If the electromagnetic wave is transmitted through a nondirective (isotropic) radar antenna, the power is scattered on a spherical surface, which area is:

$$A = 4\pi r^2 \tag{3.1}$$

where A is the area of the sphere of radius r on which the power transmitted is distributed and r is the distance from radar. The power density of the wave would be:

$$S = {}^{p_t}\!/_{A} \tag{3.2}$$

In this case, the radiation pattern of the antenna shows a pattern of lobes at various directions where the radiated signal intensity reaches a maximum, separated by directions at which the radiated signal intensity falls to zero. Instead, weather radar uses directive antennas which are conceived to emit the radio waves in one direction. The lobe in that direction, named main lobe, has a larger field strength than the others (Fig. 3.1).

For direction outside the main beam, a typical radiation intensity pattern has sidelobes that usually have maximums much smaller than that of the main lobe. The sidelobes represent unwanted radiation in undesired directions. The larger the antenna (that is the larger the wavelength), the greater the magnitude of its radiation intensity, and the more numerous and narrow the sidelobes are (Peebles, 1998). Antennas most capable to concentrate power in a narrow beam are built to minimize the signal intensity of side lobes.

A fundamental parameter of an antenna is the directive gain g that represents the capability of the antenna to concentrate the transmitted power at a direction. g is dimensionless and can be equal or greater than one, and it is defined as follows:

$$g = P_a / P_t \tag{3.3}$$

where P_a is the power transmitted by a directive antenna and P_t is the power transmitted by an isotropic antenna. For the most part of the antennas g has very great values. Therefore, it is expressed in decibel:

$$G = 10 \log\left(P_a / P_t \right) \tag{3.4}$$

The directive gain gives the increase of the wave's power density at a direction. For this reason it is measured correspondingly to the direction where the antenna transmits the maximum power.

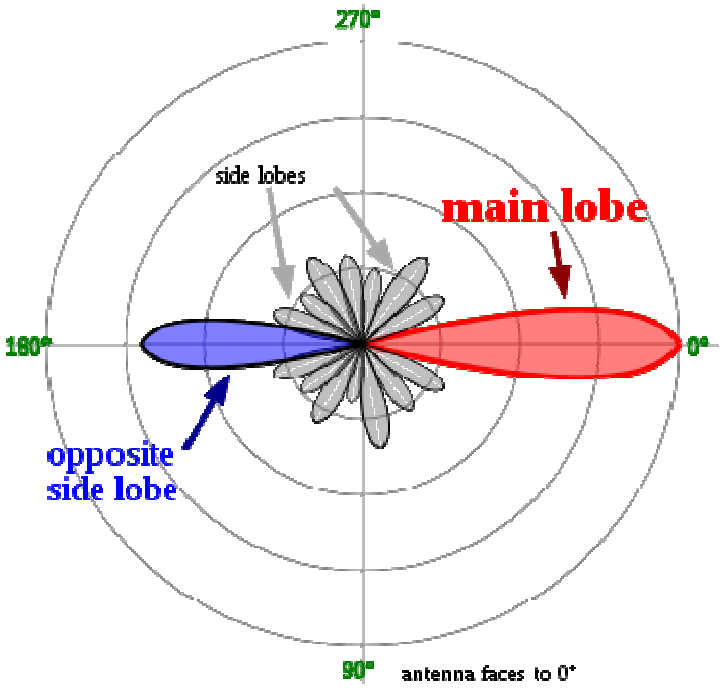

Figure 3.1 - A typical directional antenna radiation pattern in polar coordinate system representation, showing side lobes.

The amount of power intercepted by a target at a certain distance is given by the product of the power density emitted by radar, which is calculated in the position of the target, multiplied by the target area A_σ. Therefore, considering a radar antenna with a directive gain g, it has:

$$P_\sigma = \frac{P_t g A_\sigma}{A} \tag{3.5}$$

The energy absorbed by the target is converted in part in the form of thermal energy, and in part is re-irradiated isotropically in all directions and, therefore, in part also to the radar. As a consequence, the amount of energy emitted by the target and detected by the radar is given by:

$$P_r = \frac{P_\sigma A_e}{A} \tag{3.6}$$

being A_e the effective area of the receiving antenna, which can be expressed in terms of both the antenna gain and the wavelength of the radar as:

$$A_e = \frac{g\,\lambda^2}{4\pi} \tag{3.7}$$

Introducing Eq. (3.7) and Eq. (3.5) into the Eq. (3.6) we obtain:

$$P_r = \frac{P_t\, g\, A_\sigma\, A_e}{A^2} = \frac{P_t\, g^2\, \lambda^2\, A_\sigma}{(4\pi)^3\, r^4} \tag{3.8}$$

which, as already mentioned, is the amount of energy emitted by the target and detected by the radar.

The physical dimensions of the target are not necessarily those with which it is seen from the radar, therefore, a new parameter called the Radar Cross Section (RCS) σ is defined. The RCS of an object is the cross-sectional area of a perfectly reflecting sphere that would produce the same strength reflection as would the object in question. The RCS defines the effective size under which the target is seen by the radar. σ is a function of the form, the type and particle size considered, as well as the wavelength of the radar.

It follows that the final form of the radar equation, valid for a point target, can be written as:

$$P_r = \frac{P_t\, g\, \sigma\, A_0}{A^2} = \frac{P_t\, g^2\, \lambda^2\, \sigma}{(4\pi)^3\, r^4} \tag{3.9}$$

The backscattering section cannot always be calculated analytically, since many targets have a complex shape, however, the shape of the objects considered in radar meteorology is well approximated by a sphere. Consequently, for the calculation of this surface area, three main cases can be distinguished, depending on the diameter D of the spheres (Rinehart, 1997). When the sphere is large compared to the wavelength of the radar ($D/\lambda > 10$), it belongs to the optical region and the RCS of the target is equal to the geometric surface, i.e.:

$$\sigma = \pi r^2 \tag{3.10}$$

When the size of the sphere is small, in comparison to the wavelength of the radar ($D/\lambda < 0.1$), the sphere belongs to the so-called region of Rayleigh. In this region σ is proportional to the sixth power of the diameter:

$$\sigma = \frac{\pi^5 |K|^2 D^6}{\lambda^4} \tag{3.11}$$

where λ is the wavelength, D_i is the diameter of the sphere, $|K|^2 = (m_r^2-1)/(m_r^2+2)$ is the dielectric factor, which depends on the complex refractive index $m_r = n_r - jk_a$, and then by the

material, the temperature and the wavelength. k_a is the absorption index and n_r is the refractive index of the medium in which the pulse propagates. For a weather radar the propagation medium is the atmosphere, and propagation velocity is quite close to the propagation velocity of the light in the empty space, *c*, which is equal to about $3 \cdot 10^8$ m/s. For the most part of the frequency of the radars and to the usual temperatures, the value of $|K|^2$ ranges from $|K_w|^2 = 0.930$ for the water to $|K_i|^2 = 0.197$ for the ice. These two values differ by about 7 dB (a factor of 5 in linear terms). The intermediate region ($0.1\lambda < D < 10\lambda$) is called the region of resonance or Mie region, who is the physicist who has determined in 1908 the radar cross section for the raindrops (spherical) of any diameter. The majority of targets analyzed in radar meteorology belongs to the region of Rayleigh, because of the typical wavelengths of the weather radars. However, sometimes the particles belong to the region of Mie (especially considering the X-band radars, for which $\lambda = 3$ cm).

The radar equation for point targets (Eq. (3.9)) is valid when there is a single target in the radar sampling volume. But the meteorological targets consist of radar sampling volumes containing billions of hydrometeors. For which the total radar cross section of a sampling volume is given by the summation extended to all the radar cross sections within the same volume, as follows:

$$\sigma_t = \sum_{i=1}^{n_p} \sigma_i \tag{3.12}$$

where n_p is the number of particles present in the sampling volume V_c (incoherent target), which is given by (Doviak and Zrnić, 1993):

$$V_c = \frac{\pi}{2\ln(2)} \frac{r\vartheta}{2} \frac{r\varphi}{2} \frac{h_i}{2} \tag{3.13}$$

where θ and φ are respectively the horizontal and vertical amplitude of the radar beam, *r* is the distance from the radar, h_i is the pulse length and the factor in the denominator *2ln (2)* takes into account the actual shape of the radar beam, which depends on the type of antennas used.

Normally θ and φ are measured in degrees but in Eq. (3.13) are expressed in radians. In Eq. (3.13) is used $h_i/2$ since the duration τ_i represents the time delay of the received signal after the transmitted signal. Therefore, the pulse length h_i represents the total distance from transmitter to the target and back to the receiver, and can be expressed as the product of the speed of light and the delay time τ_i (Peebles, 1998). The duration usually ranges from 0.5 to 2 microseconds, and can be expressed as:

$$\tau_i = h_i \diagup c \tag{3.14}$$

Since the term *c* is equal to $3 \cdot 10^8$ m/s, h_i ranges from 150 to 600 m (see also Eq. (2.3)).

The radar samplings are usually averaged over several radar pulses otherwise, given the high PRF (see next section), the samples would be not independent. Moreover, they are positioned along the beam at certain points in space called range-bins or range-gates. Usually there are from 500 to 4000 range-bins depending on the type of radar. So, as regards the estimation of the rain at ground, the range-bins represent sampling intervals, which length is a function of both the duration and, therefore, the length of the pulse. Since the radial resolution of the radar is equal to half the length of the pulse, the range-bin have a length of $h_i/2$.

For example, considering a ray of the scanning circle equal to 120 km and a range bin 75 m long, 120/0.075 = 1600 range bins would be available. Instead, for a ray 150 km long 150/0.075 = 2000 range bin would be available. Increasing the radius but keeping constant h_i, if the number of range-bins exceeds the intrinsic limit of the device, it would increase the length of the range-bin, increasing the duration and, therefore, the length of a single pulse. However, increasing the pulse length, from short pulse to long pulse, there would be a lower spatial resolution.

To calculate the radar cross section of a sampling volume, it is necessary to determine the radar cross section per unit volume, which must be multiplied by the total volume:

$$\sigma_t = V_c \sum_i \sigma_i \tag{3.15}$$

where the summation is extended to single sections contained in a unit volume.

Thus, to determine the equation concerning to a radar wave which intercepts many meteorological targets, it is enough to replace, in Eq. (3.9) the expressions of the sampling volume (3.13) and of the total section of backscattering (3.15), obtaining:

$$P_r = \frac{P_t g^2 \lambda^2 \vartheta\phi h_i \sum_i \sigma_i}{1024 \ln(2) \pi^2 r^2} \tag{3.16}$$

One of the problems encountered solving the Eq. (3.16) is the determination of the section σ_i of the reference sphere. For most of the weather radar (i.e. radar with wavelengths greater than 3 cm), almost all of the hydrometeors belong within the scope of validity of the approximation of Rayleigh.

Usually it is assumed that each part of the observed storm cell is composed of water. Therefore, it is used the value $|K_w|^2$ for the calculation of the backscattering power by the Eq. (3.16). The value $|K_i|^2$ is utilized when certainly the sampling volume contain only ice, in order to avoid a significant underestimation.

Substituting the expression of the σ_i given by the Eq. (3.11) in Eq. (3.16) is obtained:

$$P_r = \frac{\pi^3 p_t g^2 \theta\phi h_i |K|^2 Z}{1024 \ln(2) \lambda^2 r^2} \tag{3.17}$$

By definition, $Z = \Sigma_i N_i D_i^6$ indicates the radar reflectivity factor, which depends on both the sixth power of the diameters (mm^6) of raindrops and the Drop Size Distribution DSD (which represents the number of drops N_i of each diameter D_i in the unit volume of reference). Units of Z are in fact (mm^6/m^3). From the Eq. (3.17) it is evident that the possibility of a radar to detect a cloud depends largely on both the size of the particles which diffuse the energy and their distance. The Eq. (3.17) can be applied to each radar and each target, provided that the particles satisfy the condition of Rayleigh.

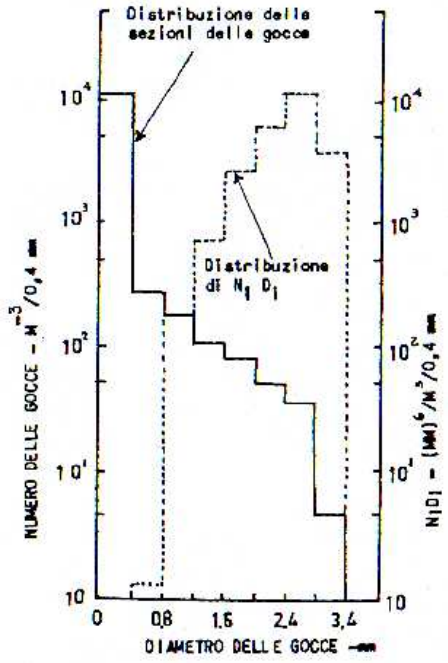

Figure 3.2 - Typical distribution of raindrops size and influence of the droplets by intervals of 0.4 mm on the reflectivity factor *Z*.

By observing Fig. 3.2, it can easily be deduced that a number, albeit small, of greater raindrops, provides most of the power of backscattering (Battan, 1970).

A critical parameter of the radar, as it is evident from Eq. (3.17), is the wavelength λ. In fact, depending on the chosen λ, the radar is capable of detecting particles with different sizes. For example, the lesser is λ, the smaller are the particles which can be detected by the radar, provided that its other characteristics are not significantly changed.

Equation (3.17) can be greatly simplified. All parameters associated with a specific radar (p_t, g, θ, φ, h_i, and λ), as well as the numerical terms π and $1024ln(2)$, can be grouped into a constant C specific to each radar, which is named radar constant. Moreover, if the hydrometeors are formed exclusively by water and not by ice, it can replace the appropriate value of K, obtaining:

$$P_r = CZ/r^2 \tag{3.18}$$

Therefore, the power received by the radar is proportional to the reflectivity factor and inversely proportional to the square of the distance from the radar.

The reflectivity factor has a wide range of variability. It ranges from $1x10^{-3}$ mm^6/m^3 for fog up to $5x10^7$ mm^6/m^3 for heavy hailstorms. Consequently, it is often preferred to express the reflectivity factor in logarithmic scale, defining:

$$Z = 10\log_{10}\left(\frac{z}{1 mm^6 m^{-3}}\right) \tag{3.19}$$

where z is the reflectivity factor in linear scale, already described above. Z is measured in dBZ, which means decibels relative to a reflectivity of 1 $mm^6 \cdot m^{-3}$. The values assumed by the reflectivity factor Z are:

- -30 ÷ 0 dBZ signal scarcely detectable;
- 0 ÷ 10 dBZ for drizzle and light snow;
- 10 ÷ 30 dBZ for moderate rainfall and heavy snowfall;
- 30 ÷ 55 dBZ for heavy rain;
- > 55 dBZ for hail.

Furthermore, in case of wet hail, the Eq. (3.17) is not suitable to estimate the rain rate. The wet hail is frequent at latitudes corresponding to the area examined in this thesis (see Chapter 5). It consists of both raindrops and hailstones covered by a coat of melt water (mixed phase). The hailstone is much larger than the raindrops, and the water that surrounds it reflects electromagnetic pulses. Consequently, the radar interprets the returned signal as the one scattered by a very large raindrop, but not by a hailstone. It follows that, since the backscattered power depends on the sixth power of the diameter of raindrops (p. 39), even a few hailstones in precipitation have a large weight in the determination of the reflectivity, which is strongly overestimated. This is because the Eq. (3.17) is based on the assumption that the hydrometeors have diameters not greater than a certain value, which is lower, however, compared to the size of the hail. Therefore, for larger diameters than those of raindrops, Eq. (3.17) is not suitable for the estimation of the reflectivity (and therefore of the intensity of rain).

If the particles were formed only by ice, the Rayleigh approximation would be valid for particles much larger. However, due to the lower refractive index, the diffusion would be five times less than that which would occur with drops of water of the same mass (Battan, 1970).

3.2 – Geometric effect

As above-mentioned (see Sect. 3.1), the reflectivity of a sampling volume is a function of both the diameters and the DSD of the hydrometeors present inside of it. It is therefore independent on the distance from the radar. Therefore, the reflectivity will be the same regardless of the spatial location of the considered sampling volume. The weather radar transmits a power that is absorbed by the hydrometeors. Subsequently, this power is re-emitted by hydrometeors in a way isotropic (i.e. in the same way in all directions). Therefore, the power is distributed widely on a spherical surface. This sphere size becomes greater the more distant is the receiver. Thus, the greater the distance between the radar and the sampling volume the lesser the energy density on the spherical surface which intercepts the receiver. In addition, since the radar intersects the surface at a point, the backscattering power P_r will be only a small part of the scattered power which is distributed widely on the spherical surface. In conclusion, the greater the distance from the radar, the lower the backscattering power P_r, which depends on both the reflectivity and the distance through Eq. (3.18).

Because of this geometric effect the backscattering power P_r decreases as the square of the distance increases (in linear scale). That is, it decreases as $20\ log(r/r_{end})$ (logarithmic scale). By expressing the power P_r in decibels and substituting the expression of P_r given by Eq. (3.18), we have:

$$p = 10\log_{10}(P_r) = 10\log_{10}\left(CZ/r^2\right) = 10\log_{10}(CZ) - 20\log_{10}(r) \qquad (3.20)$$

in which the first term in the right side is constant, while the second term is a function of distance from the radar.

To compensate for the geometric effect, i.e. to obtain a P_r independent on the distance from the radar, it is assumed a reflectivity which decreases as the distance decreases. Consequently, ΔZ being the variation of the reflectivity factor Z, and expressing the reflectivity in logarithmic scale, we obtain:

$$\Delta Z = Z - Z_{end} = 10\log_{10}\left(Z/Z_{end}\right);[dBZ] \qquad (3.21)$$

where Z_{end} is the reflectivity for the last range-bin on the considered radius, and the reflectivities in the brackets are expressed in mm^6/m^3. In this way, P_r is a function only of the properties of the hydrometeors (shape, size and spatial orientation). Substituting the expression of Z given by Eq. (3.18) in Eq. (3.21) we have:

$$\Delta Z = 20\log_{10}\left(r / r_{end}\right) \tag{3.22}$$

where r_{end} is the radius of the radar scan circle.

3.3 - Doppler radar

As above-mentioned, the backscattering power is used to determine the reflectivity of the precipitation, and the reflectivity will be used subsequently to determine the rain rate (Sect. 5.4). Many radars are also able to provide direct measurements of the radial velocity of the targets, by using the Doppler effect. That is, if a sound source and a receiver are moving relative to one another, the frequency perceived by the receiver does not coincide with the frequency emitted by the source, and their difference is proportional to the velocity of motion. For the electromagnetic radiation is the same.

Concerning the radars, the typical situation is that in which the radar is in a fixed position and the observed objects are moving. Each target varies the frequency of the signal emitted by the radar by an amount that depends on its radial velocity with respect to the radar.

Since the signal is emitted by the radar and subsequently received by it, the total distance that the signal must cover to intercept the target is equal to $2r$ (where r is the distance of the target from the radar). The number of wavelengths contained in $2r$ is $2r/\lambda$ (λ being the wavelength of the signal). The distance $2r$ may also be expressed in radians as $(2r/\lambda)\cdot 2\pi$ (where $\lambda = 2\pi$ rad). So, if the signal is transmitted with an initial phase φ_0, the phase of the returning echo is equal to:

$$\varphi_r = \varphi_0 - 4\pi r / \lambda \tag{3.23}$$

The variation of the phase by a radar pulse to the next is equal to:

$$\frac{d\varphi_r}{dt} = -\frac{4\pi}{\lambda}\frac{dr}{dt} = -\frac{4\pi}{\lambda}V_r \tag{3.24}$$

where V_r is the radial velocity of the target, which is considered positive for the targets that move away and negative for those that move toward the radar (Sauvageot, 1992).

The variation of the phase by a radar pulse to the next is also equal to:

$$\frac{d\varphi_r}{dt} = 2\pi f_D \tag{3.25}$$

where f_D (in Hz) is the difference between the frequency received by the radar and that transmitted.

Combining equations (3.24) and (3.25) we have:

$$f_D = -\frac{2V_r}{\lambda} \tag{3.26}$$

which represents the variation of the frequency for Doppler effect, and it is expressed as a function of target velocity with respect to the radar. f_D is obtained by considering both the target velocity much smaller than the velocity of light ($V_r << c$), and the distance between radar and target much greater than the wavelength ($r >> \lambda$), as in the case of weather radar.

From the Eq. (3.26) it can deduce that the Doppler radar must be able to measure the variation in time of the phase of the received signal to obtain f_D and finally V_r. To reach this aim, the radar must maintain constant both the transmitted frequency and the phase of each pulse (klystron transmitter type, coherent, as that used by the Polar 55C radar). It can be also measure the phase of each transmitted pulse (magnetron type transmitters). However, there is a limit to the maximum target velocity observable by a Doppler radar. It is named Nyquist velocity, which is the velocity which produces a difference of phase (between two consecutive pulses) equal to π radians. In fact, to cause a phase deviation of π radians, the target must move with speed such as to cover a space equal to $\lambda/2$ between two consecutive pulses. In this way, it would not be able to understand whether the target is moving towards or away from the radar. For higher speeds, also the magnitude of the radial velocity is indeterminate. For example, if the velocity was such that the distance covered between two pulses would be exactly equal to λ, the difference in phase detected by the radar would be zero. This would lead to erroneously think that the target has no radial velocity. Putting in the Eq. (3.25) $d\phi_r = \pi$ and dt = 1/PRF (time between two consecutive pulses), and replacing in Eq. (3.26), the analytical expression of the Nyquist velocity is obtained, whose intensity is:

$$V_{r\_\max} = PRF\lambda/4 \tag{3.27}$$

where PRF is the Pulse Repetition Frequency defined as in Eq. (2.2). Since the Nyquist velocity is proportional to the wavelength λ, to detect high velocities it is necessary to use large wavelengths and / or PRF.

Furthermore, there is a maximum distance where the radar is capable of determining the position of a target without ambiguity. If the radar emits a single pulse waiting for its return echo, the position of a target may be determined correctly regardless of its distance. But in the reality there are many reasons against this practice. For example, the maximum distance at which the meteorological targets can be detected depends on the earth curvature. Therefore, the rainfall events beyond about 400-500 km away from the radar location are not detectable. Moreover, since the power received by the radar is inversely proportional to the square of the distance (Eq.

(3.18)), for great distances, the received power may be so weak as not to be detected. Thus, the targets placed far away from the radar location are poorly localizable. For these and other reasons radars are designed to emit pulses at fairly frequent intervals.

The time interval elapsing between two consecutive pulses is equal to 1/PRF. Therefore, it is possible to determine the maximum distance covered by a radar pulse before the next one is emitted. Since this distance is covered by the signal twice, it has:

$$r_{\max} = \frac{c}{2PRF} \tag{3.28}$$

Equations (3.27) and (3.28) imply two constraints that must be considered in the choice of the PRF for a Doppler radar. Since for a non Doppler radar only the Eq. (3.28) is valid, the problem is solved by choosing appropriate low PRFs (usually equal to about 150-300 Hz). Instead, for the Doppler radar, being valid also Eq. (3.27), there is the so-called Doppler dilemma.

In fact, from Eq. (3.27) and (3.28) it has:

$$V_{r\_\max} r_{\max} = \frac{c\lambda}{8} \tag{3.29}$$

where c is the light velocity and λ is the radar wavelength.

The term on the second member of Eq. (3.29) is constant for a given radar. So, if high radial velocities are measured, low $r_{\max}$ will be obtained. Vice versa, if targets located very far away from the radar must to be correctly detected, only low radial velocities can be measured. For meteorological targets it can be necessary to measure velocities up to about ±50 m/s for distances over 200 km (Rinehart, 1997). But these are too much high values for the usual wavelengths of the weather radars.

The problem can be partially solved choosing longer wavelengths. In fact, for an S-band radar (λ = 10 cm) with PRF = 1000 Hz, it has $r_{\max}$ = 150 km and V_{r_max} = ±25 m/s; whereas, for an X-band radar (λ = 3 cm) with the same PRF, it has $r_{\max}$ = 150 km and V_{r_max} = ±8 m/s.

Unfortunately, radars with high wavelengths are both much expensive and larger. For this reason the C-band radar is a good compromise.

3.4 - Polarimetry

Polarimetric weather radars can lead to an improve of quantitative estimation of precipitation. For example, they can measure both the horizontal and the vertical reflectivity factor. If the horizontal reflectivity factor differs too much from the vertical reflectivity factor, it means that the raindrops are very large, that is they are very oblate. Therefore, they are able to define with a

better approximation the shape and consequently the size of the hydrometeors that compose the precipitation structures observed. To improve the precision level, so-called dual-polarized radar systems are used, which evaluate the reflectivity on two orthogonal planes.

3.4.1 – Polarization of electromagnetic waves

The electromagnetic waves are electric field vectors **E** and magnetic field vectors **H** that propagate through space at light velocity. Polarization is an electromagnetic waves feature, which indicate the electric field vector (or the magnetic field vector) oscillation direction.

Both **E** and **H** are sinusoidal vectorial quantities and they are perpendicular to each other. Moreover, since waves in the far field of a radiator are approximately plane waves, **E** and **H** lie in a plane (named the polarization plane), which is perpendicular to **r**, which is the propagation direction of the electromagnetic wave.

To establish the orientation of an electromagnetic wave in space, it is necessary to establish the orientation of one of the electromagnetic field vectors. Since **H** is always orthogonal to **E**, it is sufficient to know the orientation of **E** to determinate the wave orientation (Battan, 1970).

Since **E** can have any direction in the plane, in general, it is usually defined by its two orthogonal components E_x and E_y in whatever coordinate system is in use (Peebles, 1998). Here is used a Cartesian coordinate system (xyz) located at the radiator (radar at the origin). The total electric field is the vector sum of the components E_x and E_y. The intensity and the direction of **E** depend on both the amplitude and the phase of E_x and E_y, which vary sinusoidally with time. In general, it has:

$$E_x = E_{0x}\sin\left(\omega_0 t + \varphi_x\right) \tag{3.30a}$$

$$E_y = E_{0y}\sin\left(\omega_0 t + \varphi_y\right) \tag{3.30b}$$

where ω_0 is the angular frequency of the wave, E_{0x} and E_{0y} are the peak amplitudes of E_x and E_y, respectively, and φ_x and φ_y are the phases of E_x and E_y, respectively. Based on the difference between the two phases φ_x and φ_y different types of wave's polarization are characterized:

• linear polarization: the difference between φ_x and φ_y is equal to zero (or equal to an integer multiple of π), and E_x and E_y assume both their maximum value and the minimum value at the same instant. The angle between **E** and the abscissa axis is always the same, while its intensity ranges from E to 0. Therefore, the tip of the total electric field trace out a line once for each cycle

of the wave's frequency. The linear polarization can be horizontal or vertical when **E** has only the horizontal component ($E_{0y} = 0$) or **E** lies in the vertical plane ($E_{0x} = 0$), respectively;

• elliptical polarization: when the tip of the total electric field trace out a line once for each cycle of the wave's frequency. In particular, if $\varphi_x - \varphi_y = \pm \pi/2$ and $E_{0x} = E_{0y}$, the trace shape of the total electric field is circular. Therefore, the wave's polarization is circular and E_x assumes positive and negative maximums when $E_y = 0$ and vice versa. If $\varphi_x - \varphi_y = \pi/2$ and $E_{0x} = E_{0y}$, the polarization is named circular clockwise (vector **E** rotates clockwise as seen by a viewer positioned at the wave's source). If $\varphi_x - \varphi_y = -\pi/2$ and $E_{0x} = E_{0y}$, the polarization is named circular counterclockwise.

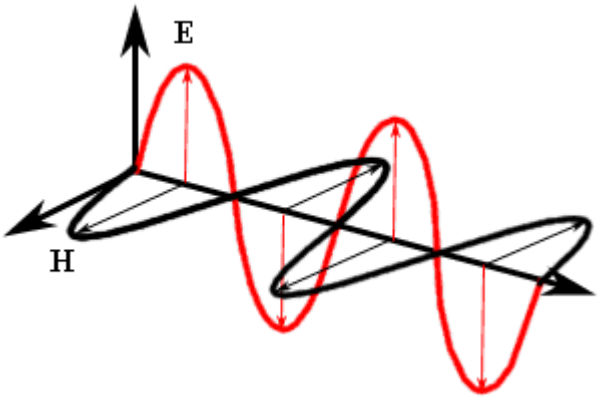

Figure 3.3 – Electromagnetic wave's polarization.

Polarimetric weather radar is able to emit circular or linear polarized pulses, and, consequently, it can detect the scattered signal's polarization.

3.4.2 – The scattering matrix

The scattered field components in the far-field are related to the incident field components through a 2 x 2 amplitude scattering matrix [**S**] which describes the polarization features of a single hydrometeor at a distance r from the radar site (Doviak and Zrnić, 1993; Bringi and Chandrasekar, 2001). The scattering matrix is defined as:

$$\begin{bmatrix} \mathbf{E}_h \\ \mathbf{E}_v \end{bmatrix}^s = \begin{bmatrix} s_{hh} & s_{hv} \\ s_{vh} & s_{vv} \end{bmatrix} \begin{bmatrix} \mathbf{E}_h \\ \mathbf{E}_v \end{bmatrix}^i \frac{e^{-jk_0 r}}{r} \qquad (3.31)$$

where both the incident electric field $[\mathbf{E}]^i$ and the scattered electric field $[\mathbf{E}]^s$ are written in terms of their two components as 2 x 1 column matrices, $k_0 = 2\pi/\lambda$ is the wave number of the free space, λ being the wavelength, while the subscripts h and v refer to the two orthogonal

polarization (horizontal and vertical polarizations as in this case, or circular clockwise and counterclockwise polarizations). The subscript h refers to the polarization of the scattered electric filed, whereas the subscript v refers to the polarization of the incident field. In a reciprocal medium, such as the precipitation, the scattering matrix is symmetrical ($s_{hv} = s_{vh}$).

The scattering matrix as in Eq. (3.31) takes into account the scattering properties of a single hydrometeor in the absence of signal propagation effects (see Sect. 4.4). The elements of [**S**] are termed the complex scattering amplitudes, and depend on scatterer size, shape, orientation, and dielectric constant. Each component of the scattering matrix is related to the radar cross section σ, which changes depending on the polarization of the incident wave. Therefore, the polarization of the back-scattered wave depends on shape, size, and spatial orientation of the raindrop when it is intercepted by the radar beam. Assuming a horizontal polarized incident wave, the raindrop can back-scatter a pulse which can be polarized horizontally or vertically. But the raindrop can also back-scatter two pulses for each of the two linear polarizations. In the latter case, the scattering matrix terms of interest are s_{hh} and s_{vh}. If in a subsequent instant the radar changes the transmitted polarization state (polarization agility), then the terms of interest become s_{vv} and s_{hv}.

For example, assuming a horizontal polarized incident wave (see Sect. 3.4.4), and if the raindrop considered was of spherical shape, the scattered wave would be horizontally polarized too. In this case, the only nonzero term of the scattering matrix would be s_{hh}. Instead, assuming a vertically polarized incident wave, if the back-scattered wave was vertically polarized, the only nonzero term of the scattering matrix would be s_{vv}.

3.4.3 – Covariance matrix and polarimetric measurables

In the present study we consider an orthogonal linear polarization. Moreover, the propagation effects are initially neglected, that will be considered in Sect. 4.2.8.

As above-mentioned, the electric field scattered by a generic hydrometeor depends on the incident electric field, when the scattering matrix is note. However, the radar analyses the complex voltages *v* that are generated in output by the receiver, when the electric field scattered by a hydrometeor is intercepted by the antenna. Assuming a linear polarized electric field scattered by each hydrometeor, the overall voltage $V_{i,j}$ is equal to the sum of the voltages $v_{i,j}$ due to each hydrometeor in a sampling volume:

$$V_{i,j} = \sum_n v_{i,j} = \sum_n s_{i,j}(n) F(r_n) e^{-j2k_0 r_n} \qquad (3.32)$$

where n indicates the nth-hydrometeor, $s_{i,j}$ is an element of the scattering matrix for the nth-hydrometeor (subscripts i and j refers to the incident field polarization and to the scattered field polarization respectively), r_n is the distance between the nth-hydrometeor and the radar site, and $F(r_n)$ is a proportionality factor which takes into account several parameters such as the distance and the attenuation (Jameson, 1985; Doviak e Zrnić, 1993; Lombardo, 2007). Since the mean value of the voltage is equal to zero, the second-order moments of $V_{i,j}$ are calculated, which characterize the polarimetric signals. The generic moment of the second order $\langle V_{i,j} V_{k,l}^* \rangle$ (where brackets $\langle\rangle$ are related to the expected value operator and the symbol * indicates the complex conjugate) is:

$$\left\langle V_{i,j} V_{k,l}^* \right\rangle = \left\langle s_{i,j} s_{k,l}^* \right\rangle \int \left| F(r_n) \right|^2 dV_c \tag{3.33}$$

where the integral is extended to the whole sampling volume, and $\langle s_{i,j} s_{k,l}^* \rangle$ is the generic element of the so-called covariance scattering matrix. The moments of the second order of $V_{i,j}$ are the coefficient of a 4 x 4 matrix termed the voltage covariance matrix, defined as follows:

$$E\begin{bmatrix} \left|V_{hh}\right|^2 & V_{hh}(V_{vh})^* & V_{hh}(V_{hv})^* & V_{hh}(V_{vv})^* \\ V_{vh}(V_{hh})^* & \left|V_{vh}\right|^2 & V_{vh}(V_{hv})^* & V_{vh}(V_{vv})^* \\ V_{hv}(V_{hh})^* & V_{hv}(V_{vh})^* & \left|V_{hv}\right|^2 & V_{hv}(V_{vv})^* \\ V_{vv}(V_{hh})^* & V_{vv}(V_{vh})^* & V_{vv}(V_{hv})^* & \left|V_{vv}\right|^2 \end{bmatrix} \tag{3.34}$$

But, being valid the reciprocity theorem (Bringi and Chandrasekar, 2001), the voltage covariance matrix is a symmetric matrix (being $V_{ij} = V_{ji}$), and it become a 3 x 3 matrix. Equation (3.33) shows that the voltage covariance matrix is proportional to the covariance scattering matrix (Lombardo, 2007), defined as follows:

$$\begin{bmatrix} \left\langle \left|s_{hh}\right|^2 \right\rangle & \left\langle s_{hv} s_{hh}^* \right\rangle & \left\langle s_{vv} s_{hh}^* \right\rangle \\ \left\langle s_{hh} s_{hv}^* \right\rangle & \left\langle \left|s_{hv}\right|^2 \right\rangle & \left\langle s_{vv} s_{hv}^* \right\rangle \\ \left\langle s_{hh} s_{vv}^* \right\rangle & \left\langle s_{hv} s_{vv}^* \right\rangle & \left\langle \left|s_{vv}\right|^2 \right\rangle \end{bmatrix} \tag{3.35}$$

Each coefficient of the covariance scattering matrix depends on the probability density of the hydrometeors properties (shape, size and spatial orientation), as follows:

$$\left\langle s_{i,j} s_{k,l}^* \right\rangle = \int N(\mathbf{X})\, s_{i,j} s_{k,l}^*\, d\mathbf{X} \tag{3.36}$$

where $N(\boldsymbol{X})$ is the probability density of the hydrometeors properties. As showed by Eq. (3.35) the covariance scattering matrix has 9 coefficients. These coefficients are the real variables that

can be measured by a polarimetric radar (Ioannidis and Hammers, 1979; Bringi and Chandrasekar, 2001; Lombardo, 2007). Between the polarimetric variables most commonly used in literature, obtained from some of these 9 quantities, there are:

- the reflectivity factor at horizontal polarization (between the transmitted *hh* and the *hh* return):

$$Z_h = \left(\frac{4\lambda^4}{\pi^4 |K_w|^2} \right) \left\langle |s_{hh}|^2 \right\rangle ; \left[mm^6 \cdot m^{-3} \right] \tag{3.37}$$

- the reflectivity factor at vertical polarization (between the transmitted *vv* and the *vv* return):

$$Z_v = \left(\frac{4\lambda^4}{\pi^4 |K_w|^2} \right) \left\langle |s_{vv}|^2 \right\rangle ; \left[mm^6 \cdot m^{-3} \right] \tag{3.38}$$

- the differential reflectivity:

$$Z_{DR} = 10 \log_{10} \left(\frac{\left\langle |s_{hh}|^2 \right\rangle}{\left\langle |s_{vv}|^2 \right\rangle} \right) ; \left[dB \right] \tag{3.39}$$

- the copolar correlation coefficient between the *hh* and *vv* return, assuming that they are received simultaneously:

$$\rho_{hv}(0) = \frac{\left\langle s_{vv} s_{hh}^* \right\rangle}{\sqrt{\left\langle |s_{hh}|^2 \right\rangle \left\langle |s_{vv}|^2 \right\rangle}} \tag{3.40}$$

3.4.4 – Shape of hydrometeors

Information about the shape of raindrops is critical for estimating rainfall rate with dual polarization radar (Gorgucci and Baldini, 2009). The assumption of spheroidal shape is somewhat simplicistic considering the wide distribution of shapes of natural hydrometeors (Bringi and Chandrasekar, 2001). The shape of a raindrop which falls at its terminal velocity is determined by the balance between the forces due to the gravitational field, the surface tension and hydrostatic and aerodynamic pressures due to airflow around the raindrop (Green, 1975; Gorgucci et al., 1999). Figure 3.4 shows the equilibrium form depending on the size of the raindrops, which fall on their terminal velocity.

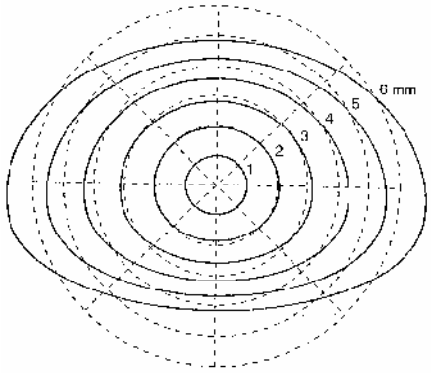

Figure 3.4 – Equilibrium shape of the raindrops.

For radar polarimetry application, raindrops are modeled as spheroids characterized by the ratio r between the semiminor and the semimajor axis lengths. A shape-size model identifies the relationship between r and the equi-volume drop diameter D_e, which is the diameter of the sphere whose volume equals that of the equivalent oblate spheroid. For small raindrops (D_e <0.28 mm), r ~ 1 and monotonically decreases as D_e increases, meaning that raindrop oblateness increases as D_e increases.

In the absence of air motion, the raindrops fall with the semiminor axis in vertical position, and the eccentricity depends only by D_e (Green, 1975). For D_e > 1 mm the raindrops begin to flatten out until the ratio between width and thickness is not almost 2:1, and this occurs when D_e reaches the maximum limit of 8 mm. Beyond this limit the droplet breaks. To determine the coefficients of the scattering matrix for oblate hydrometeors, considering incident waves both linearly and vertically polarized, the Gans (1912) simplifying theory is utilized, which extends the Rayleigh theory regarding the spheres to the case of oblate spheroids. For spheroids oriented as in Fig. 3.5 the scattering matrix elements are given by (Bringi and Chandrasekar, 2001):

$$s_{hh} = -\frac{k_0^2}{4\pi\varepsilon_0}\left[\alpha\cos^2\psi + \sin^2\psi\left(\alpha_z\sin^2\beta + \alpha\cos^2\beta\right)\right] \qquad (3.41a)$$

$$s_{vh} = -s_{hv} = \frac{k_0^2}{4\pi\varepsilon_0}\left[\frac{(\alpha_z-\alpha)}{2}\sin^2\psi\sin 2\beta\right] \qquad (3.41b)$$

$$s_{vv} = \frac{k_0^2}{4\pi\varepsilon_0}\left[\alpha\cos^2\psi + \sin^2\psi\left(\alpha_z\cos^2\beta + \alpha\sin^2\beta\right)\right] \qquad (3.41c)$$

where ε_0 is the permittivity of empty space, α is the polarizability of a sphere, α_z is the polarizability of a spheroid along its symmetry axis, ψ is the angle between the incidence direction and the symmetry axis, β is the canting angle. The canting angle is the angle between the incident electric field and the projection of the symmetry axis on the polarization plane. Figure 3.5 showed an oriented oblate spheroid, which symmetry axis is given by the angles θ_b

and ϕ_b. The incident plane wave is along the direction k_i, being $0 \leq \theta_i \leq 90°$ the incident angle. The plane of polarization of the incident wave is defined as the plane orthogonal to k_i.

Several researches have been effectuated to determining a proper equation to describe the shape-size relation. It has been established in the literature that the relation expressing r as a function of D_e in non linear. However there is still no consensus regarding the most appropriate equation to use to describe the shape-size relation for radar applications (Pruppacher and Beard, 1970; Goddard et al., 1982; Beard and Chuang, 1987; Gorgucci et al., 2006; Gorgucci and Baldini, 2009).

In conclusion, the power back-scattered at both the horizontal and vertical polarization depends on both the distribution of size and shape and the canting angle of the raindrops in the sampling volume. Therefore, Z_{DR} can be used to detect the shape and the size of the oriented oblate raindrops when the incident beam is at a low elevation angle (θ_i~90°).

In fact, the differential reflectivity can be defined as follows:

$$Z_{DR} = 10\log_{10}\left(Z_h \big/ Z_v\right);[dB] \tag{3.42}$$

depending on the axis ratio b/a of the raindrop. The axis ratio can be expresses by an empirical relation (Gorgucci et al., 1999):

$$b \big/ a = 1.03 - 0.062\, D_e \tag{3.43}$$

As showed in Fig. 3.6, tiny drops (D ≤ 1 mm) are spherical with b/a = 1, while larger drops have axis ratios that decrease nearly linearly with increasing D, and thus Z_{DR} can be related to D for single drops. Since the raindrops are oblate and they fluctuate during falling, the power back-scattered is different from horizontal to vertical polarization, and, therefore, $Z_{DR} \neq 0$, being $Z_h \neq Z_v$. Raindrops produce positive values of Z_{DR}, because they are an oblate shape as above-mentioned. So, the greater values of Z_{DR} correspond to the presence of larger raindrops. In the case of rainfall, Z_{DR} values range from 0 up to 4 dB or more, as showed by Fig. 3.6.

In the case of hail, the raindrops are prolate and they are subject to tumbling motions. Therefore Z_{DR} is quite close to zero, ranging from -1 to 0.5 dB. In the case of snowfall Z_{DR} ranges from -1 to 0 dB.

If the raindrops would be spherical and in the absence of tumbling motions or oscillations $Z_h = Z_v$ and Z_{DR} = 0. In this case, for a single hydrometeor, the polarization of the incident pulse is the same as the polarization of the scattered pulse, and the power back-scattered is the same at both the orthogonal polarizations. As a consequence, the scattering matrix is the following:

$$\frac{k_0}{4\pi}\left(\frac{\varepsilon_r - 1}{\varepsilon_r + 2}\right) 3V \begin{bmatrix} 1 & 0 \\ 0 & 1 \end{bmatrix} \tag{3.44}$$

where ε_r is the relative permittivity of a dielectric.

If the radar is able to change the transmitted polarization state between the two orthogonal states on a pulse-to-pulse basis (polarization agility), it can determinate the shape and the size of the hydrometeors, by measuring the difference between Z_h and Z_v, that is Z_{DR}.

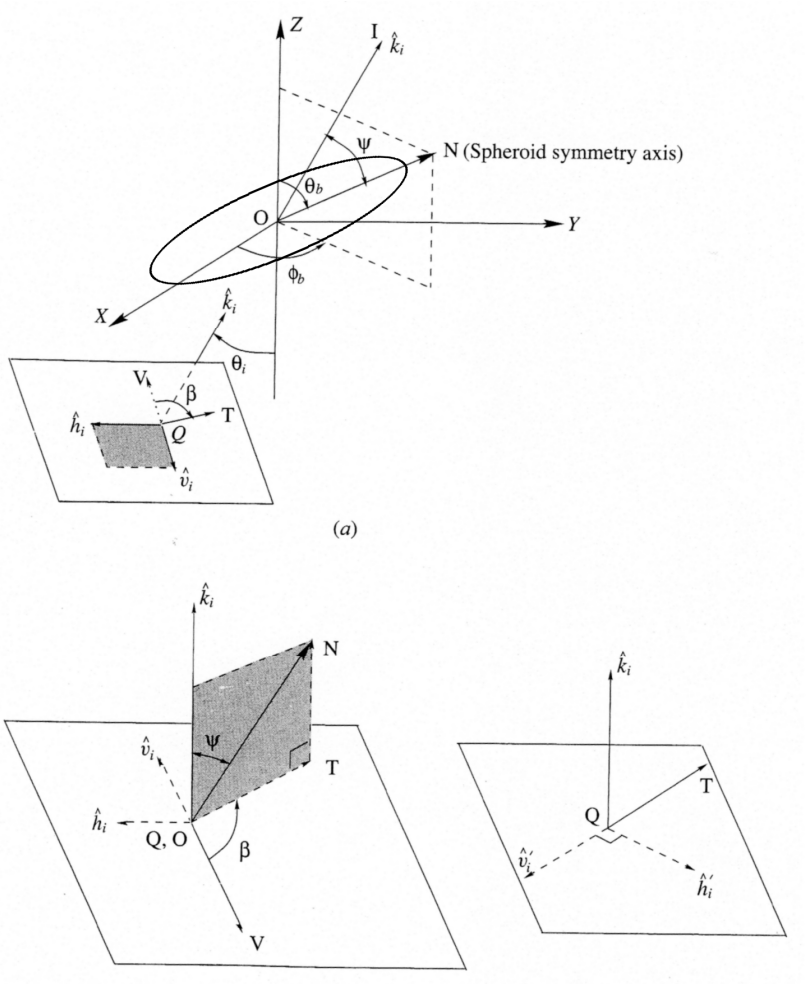

Figure 3.5 – Orientation of the symmetry axis of a spheroid described by the orientation angles (θ_b and f_b) of the symmetry axis wave's polarization. Also showed is the horizontal incidence θ_i as well as the canting angle β, and the angle ψ between the incidence direction and the symmetry axis.

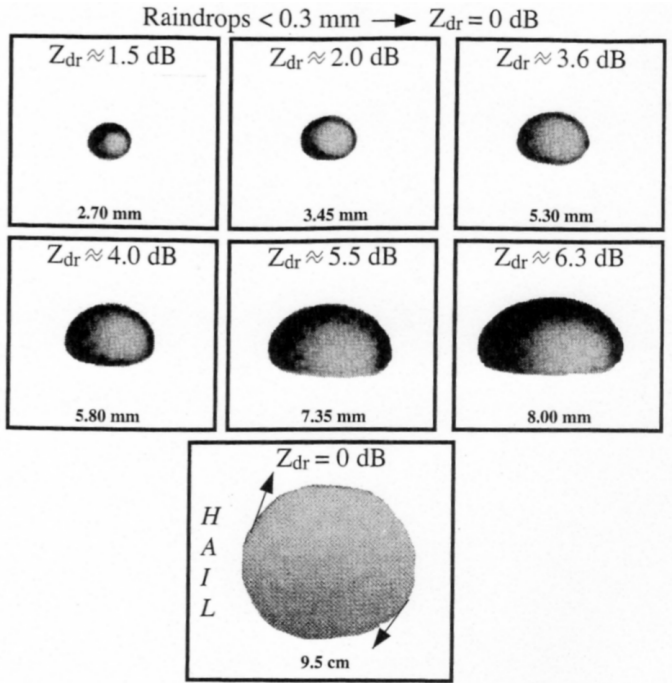

Figure 3.6 – Z_{DR} values in relation to the size of the hydrometeors.

Chapter 4

Sources of error in radar-based estimates of rainfall

4.1 - Sampling differences between weather radar and rain gauge

The possibility to predict the rainfall events is very important for taking suitable measures to reduce the damages due to heavy storms. The precipitation measurements are the starting point for studying the hydrological processes. Precipitation estimates are utilized as input in hydrological simulation models indispensable to correct territorial planning and to the adequate management of hydraulic systems. As a consequence, a key factor for accurate flood estimates is to know accurate rainfall input to drive hydrological models.

It is well known that radar and rain gauges go through fundamentally different processes to estimate rain. Rain gauges collect water over a period of time, whereas radar obtains instantaneous snapshots of electromagnetic backscatter from rain volumes that are then converted to rainfall via some algorithms (Russo et al., 2005). In this paragraph the sampling differences between radar and rain gauge will be detailed.

Rain gauges measurements are a major input of hydrological models, but they are affected by errors ascribable to several causes, such as: internal frictions and occasional imperfections of the rain gauge, reading errors, wind action which deflects the precipitation, and presence of buildings, trees, or others human-made artifacts close to the rain gauge, which change locally the characteristics of the rain field, or do not allow to the device to collect the raindrops. Furthermore, since the rain gauges are scattered along a territory, it is always difficult and expensive to assure their correct operation, due to the difficult of monitoring and maintenance. Moreover it is necessary to consider how much the rain gauge can reconstruct a pattern of precipitation.

One of the most important limits of hydrological prediction is due to the low resolution of input of hydrological models (Vaes et al., 2001). Since usually in small catchments only one rain gauge is available, its pointwise measurement is considered uniform over the whole of the area. But, it is well-known that assume a homogeneous precipitation over an area lead to a strong underestimation of the discharges. Therefore, in order to estimate the rainfall fields over an

entire basin, the rain gauge pointwise measurements need to be interpolated and the small-scale variability of rainfall fields can lead to biases in the rain rate estimation over an entire basin, above all for small or medium size mountainous and urban catchments (Borga et al., 2000; Todini, 1995). Techniques have been proposed to estimate area-average rainfall over an area or a region from point measurements, such as arithmetic mean method, Thiessen polygon method, and isohyetal method (Chow et al., 1988; Calenda and Margaritora, 1993). But different interpolation methods can give significant differences in rainfall field estimates (Dirks et al., 1998). For these reasons, the input of hydrological models is often subject to strong uncertainty (Paoletti, 1993; Vaes et al., 2001). As a consequence, several rain gauges should be installed in different places in order to determine the spatial rainfall distribution during the evolution of the natural phenomena over the selected area (Paoletti, 1993). In fact, the accuracy of flood estimates depends essentially on the rain gauges network density, configuration and on the instrument precision (Maheepala et al., 2001).

Many observational studies of rainfall identify some specific elements of rainfall fields in space by underlining the trend of rain cells to cluster inside larger-scale structures called small mesoscale areas (SMSA), contained inside large mesoscale areas (LMSA), which, in turn, are contained inside synoptic areas (Austin and Houze, 1972). These regions are all characterized by different rainfall intensities where rain cells have the highest intensities. Because of this particular precipitation structure we can observe both high intensity rainfall clustering in small areas and rainfall intensity decreasing with distance from the point of highest rain intensity (Lombardo et al., 2006).

The reduction of high intensity rainfalls with increasing areas is a key issue in many hydrological problems, e.g. in designing hydraulic structures for flood control as in urban drainage systems (Bacchi and Ranzi, 1996). In fact, it is very probable to observe a heavy rainfall for short length of time and over a restricted area (Moisello, 1999). As a consequence, during a rainfall event, the point of highest rain intensity could not interest the rain gauge site. Hence, the not homogeneous density of a rain gauge network causes loss of information, especially in the case of heavy rainfall, and where the rainfall fields are more unhomogeneous in space. Homogeneous precipitations can occur for small catchment, in not-mountainous district, or during stratiform events. Vice versa, in wide areas the characteristics of the rainfall field could be often not homogeneous in space, and that occurs particularly in mountainous regions (Moisello, 1999), where the number of rain gauges should be greater. Instead, mountainous areas are almost without rain gauges.

Furthermore, due to the different types of rain gauges in a rain gauge network, the information they provide is not-homogeneous both in space and time. For example, in Italy there are often both ordinary rain gauge and recording rain gauges (see Chapter 2).

In this context weather radars have several advantages since a single site is able to obtain coverage over a wide area with very high temporal and spatial resolution. In fact, radar sampling area can be many orders of magnitude greater than the area above which rain gauge collects precipitation, which are over 10000 km^2 (depending on the distance) and 0.1 m^2 respectively. Assuming a range of 150 m, a beam width of 1°, and a ray of the scanning circle equal to 150 km, this means that more than 300 thousands rain gauges should be necessary to replace the whole of range-bins. Furthermore, radars can provide quick updates of the tridimensional structure of precipitation by making scanning with different elevation angles, which are made about every minute (time necessary to the antenna to make a sweep).

Therefore, weather radars play a significant role in the rainfall field estimation and consequently in the improvements of hydrograph simulation (Lopez et al., 2005), which is necessary for the hydraulic risk assessment, for providing flood forecasting and forewarning (with a safety margin), for the design of drainage systems (Clothier and Pegram, 2002), and for statistical characterization of extreme rainfall frequency (Krajewski and Smith, 2002). A very high space–time rainfall resolution is needed especially in small catchments, like urban catchments, which have a short time of concentration, in order to obtain, with sufficient accuracy, flash flood nowcasting as well as monitoring of sewer systems.

In consequence, the rain gauges are less able than radar to capture well the spatial variability of rainfall with time, which is particularly evident at short timescales. Whereas, as the period of accumulation increases, the expected spatial variability is reduced and rain gauges provide improved spatial rainfall estimates (Pegram and Clothier, 1999; Sinclair and Pegram, 2005).

For these reasons, the importance of radar estimates of precipitation tends gradually to increase both for operational and research purposes (Lombardo, 2007).

Moreover, radar estimates of precipitation can significantly integrate the information provided by the rain gauge network, both to correct errors in radar estimates and to reconstruct the rainfall fields. Techniques are proposed for utilizing rain gauge data to correct bias (Koistinen and Puhakka, 1986; Saltikoff et al. 2000; Russo, 2004) as well as range dependent error in rainfall radar estimates (Zawadzki, 1975; Borga and Tonelli, 2000; Gabella et. Al, 2001; Ozturk and Yilmazer, 2007). These methods consider rain gauges direct rainfall measurements as “ground truth”. Furthermore, rainfall is estimated by combining information from both radar and rain gauge network through merging techniques (Ehret, 2002; Pegram, 2002; Sinclair and

Pegram, 2005). But, in order to reach these purposes, sampling differences between radar and rain gauge, which lead to discrepancies between radar-derived rainfall estimates and rain gauges data (Zawadzki, 1984), must be considered. Uncertainties in radar estimates of rain are due to temporal and spatial sampling differences of the two devices (Villarini et al., 2008b). The temporal uncertainties which affect radar estimates are due to the temporal gaps between rain gauges and radar observations, depending on the sampling volume height above the rain gauges. But the effects due to these gaps decrease as the accumulation time increases (Krajewski, 1995; Steiner et al., 1999; Russo et al., 2005). Factors producing discrepancies between radar and rain gauge data can produce the following errors (Zawadzki, 1984): (1) random errors, such as the error associated with the transformation from reflectivity to rain rate due to the variability of drop size distribution; (2) systematic errors (Villarini et al., 2008b) due to radar miscalibration; (3) range-dependent errors, such as the sampling uncertainties that are associated with beam broadening and the increase in height with range of the sample volume (Berenguer and Zawadzki, 2008; Berenguer and Zawadzki, 2009), which cause temporal and spatial sampling differences of the two devices (Villarini et al., 2008a).

Weather radar has been established as an invaluable tool for provision of weather services, as it facilitates monitoring of precipitation events and predicts their short time evolution. However, it is not as well established as a tool for the quantitative estimation of precipitation (Delrieu et al., 2009). Thus, for many applications (especially applications that require long-term precipitation estimates, such as those related to hydraulic risk assessment) conventional measurements from a network of sparse rain gauges are still preferred (Sebastianelli et al., 2013).

4.2 - Errors associated with radar estimate of rainfall

Despite the weather radars have several advantages in rainfall estimates, with respect to the rain gauges, many sources of error affect radar measurements. These include radar miscalibration, range degradation (including beam broadening and sampling of precipitation at increasing altitude), attenuation, ground clutter, variability of the *Z-R* relation, instrument sensitivity, vertical variability of the precipitation system, vertical air motion, precipitation drift, temporal sampling error, anomalous propagation and beam-blocking (Villarini and Krajewski, 2010). These produce an overall error, which tends to increase as the distance from radar increases. As a consequence, the spatial structure of a rain field that is derived from weather radar measurements is affected by the way that the radar samples precipitation. Therefore, the rainfall rate estimated by weather radars differs from the precipitation collected at the ground by a rain gauge. This

means that to correctly estimate the precipitation at the ground it is necessary that the reflectivity data must be corrected. As noted above, the accuracy of radar rainfall estimates has been traditionally assessed by performing a comparison with rainfall measurements at ground obtained by rain gauges. Following this purpose, errors are found that depend on the location of the rain gauges (Sebastianelli et al., 2013).

As already mentioned, weather radar indirectly provides estimates of the rain rate, because it directly measures the back-scattered power P_r, that, subsequently, is related to the rainfall intensity R by means of the reflectivity factor Z (Sect. 5.4.1). The P_r measure is affected by several errors, which can be independent from time and space, such as the systematic error, or range related, such as the error due to the beam broadening, the radar sampling height, and the signal attenuation. In the following sections the main sources of errors in rainfall radar estimates will be accounted.

4.2.1 – Range degradation of radar measurements

As above-mentioned, the radar measures precipitation at a given height, whereas rainfall is registered by the rain gauge below the radar sample volume with a delay with respect to the radar. This question is named the ground truth problem (Rinehart, 1997). The delay depends on the time needed for the raindrops to precipitate. In other words it depends on the radar sampling height.

The range degradation of radar estimates of rainfall is due to the fact that the radar beam tends to widen as the distance from it increases, and, consequently, at great distance the rain rate is obtained with a less spatial resolution. This fact leads to a rain rate underestimation by the radar, which increases as the distance increases.

Furthermore, in some cases the rain gauge cannot measure any precipitation, whereas the radar can detect the presence of the raindrops in the atmosphere. In fact, due to the earth's curvature and to the positive elevation angles (which must be used to avoid beam interceptions by obstacles or relieves), at great distance from the radar antenna, the radar beam can overshoot the clouds, and does not intercept precipitation.

Hence, due to the beam broadening, the radar sampling height, and the signal attenuation (see Sect. 4.2.8) the signal returned from precipitation can be quite close to the minimum detectable signal at great distance, also at low elevations. In this case the radar receives only noise, and it cannot detect precipitation unlike a rain gauge situated below the radar sampling volume. As a consequence, the spatial sampling of precipitation performed by the radar is not uniform and the

same precipitation produces a return characterized by a signal to noise ratio that decreases with increasing distance.

So, the spatial and temporal sampling differences between the two devices cause a range-dependent error which increases as the distance from radar increases, because of the increasing altitude and width of the radar beam with distance from the radar site.

4.2.2 – Variability of the *Z-R* relation

As already mentioned, the reflectivity is a function of the DSD (See Sect. 3.1) and, therefore, also rainfall rate depend on it through a *Z-R* relation (see Sect. 5.4.1). Moreover, the DSD influences the coefficients of the *Z-R* relationship (Eq. (5.3)), and varies geographically, depending on the characteristic of the rainfall event (stratiform or convective), and even within the same rain field with rainfall intensity (Villarini and Krajewski, 2010).

4.2.3 – Vertical variability of the precipitation system and bright band

Weather radars measure the reflectivity in sampling volumes aloft, at a certain distance from the earth's surface. For a certain elevation angle this distance increases as the range increases. As a consequence, considerable effects occur because of the vertical variability of the precipitation systems, which is due to the factor $|K|^2$ (see Eq. (3.11)), but also to evaporation, collision, coalescence, and break-up of the rain drops aloft.

Depending on the distance, the type of precipitation, and the elevation angle, the radar beam can moves through the melting layer, intercepting ice particles that are melting. As showed by Fig. 4.1, these particles are formed by a core of ice covered by a coat of water. The ice particles are greater than the raindrops, and the water layer on their surface reflects the radar waves. Therefore, they behave like raindrops that are greater than usual raindrops (Sebastianelli et al., 2013). The bright band is the region just below the 0° isotherm where snow melts and presents enhanced reflectivity with respect to the rain below or the snow above. This imply a strong overestimation of the reflectivity, and, consequently, of the rainfall rate by the radar. Moreover, the bright-band is displayed on a PPI display, as a bright ring, placed almost all around the radar site at a distance which depends on the antenna angle. The bright band can occur during stratiform precipitations, depending on the vertical profile of temperature. However, the absence of a bright band does not imply the absence of stratiform precipitation structure. Furthermore, even if a bright band occurs, the vertical resolution of the radar could be not sufficiently fine to observe it. Hence, the bright band is a property of the radar data (Houze, 1997). Instead, within

convective cells, bright band is not defined, because the intense updraft can stop the formation of a melting layer, or the transition between snow and rainfall is chaotic and undetectable (Steiner et al., 1995; Villarini and Krajewski, 2010). There are also events occurring as cores of convective precipitations embedded into a widespread stratiform precipitation area, the latter may exhibit a bright band, as better detailed in Chapter 7. For a stratiform event, due to the melting layer, weather radar overestimates rainfall close to its location, depending on the elevation angle (Sebastianelli et al., 2013). As already mentioned in Chapter 3, the reflectivity depends on the 6th power of the diameter of the raindrops, and, therefore, even a few ice particles that are melting in the sampling volume are sufficient to cause an overestimation of the rainfall rate by the radar.

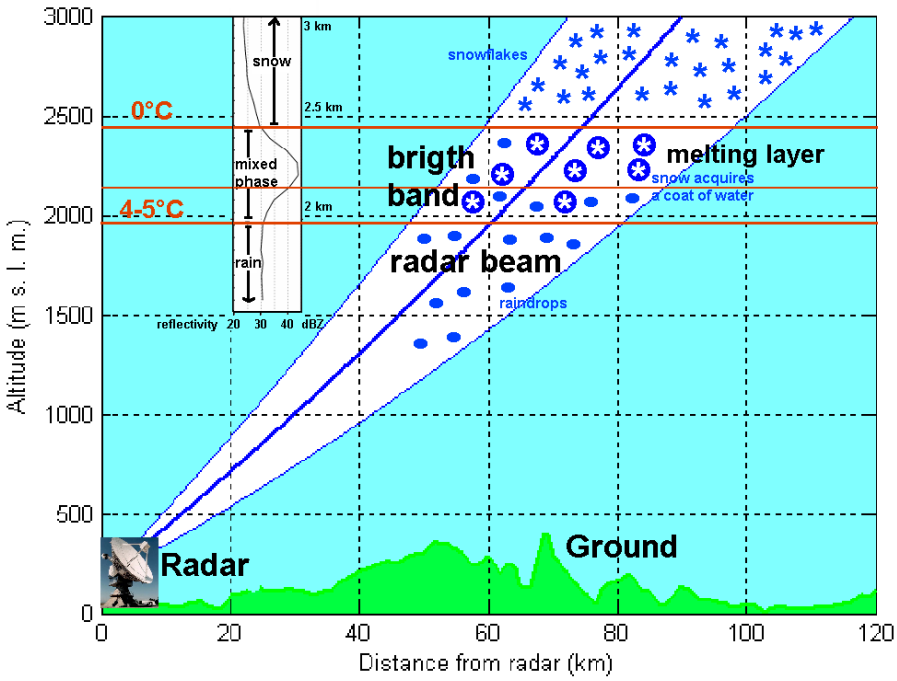

Figure 4.1 – The bright-band.

To correct for range dependent bias due to the vertical variability of the precipitation system, several approaches have been proposed. Each methodology aims to identify and correct for the vertical profile of reflectivity (hereafter VPR). VPR is related to changes in the shape and size distribution of hydrometeors as well as to their phase transition. It is usually defined as the ratio between the reflectivity at a certain altitude and the reflectivity at the ground (Andrieu and Creutin, 1995; Andrieu et al, 1995; Vignal et al., 1999; Vignal et al., 2000; Mittermaier and Illingworth, 2003; Zhang et al., 2008; Kirstetter et al., 2010; Bordoy et al., 2010).

4.2.4 – Air Motion

Vertical air motion is a source of uncertainty extremely variable both in space and time. The updraft can delay or block the precipitation, resulting in a decrease in rain rate. At the contrary, the downdraft causes an increase of the rainfall intensity. Both the updraft and the downdraft affect the drop size distribution, which has an impact on the *Z-R* relations. Moreover, the wind can move away the raindrops from the rain gauge, because they fall in a non-straight vertical line. The precipitation drift influences the drop size distribution too. Furthermore, the higher the radar beam the higher the probability that larger drops increase their mass by collection of cloud water in their fall paths (coalescence), or the small diameter raindrops evaporate in the atmosphere before reaching the ground. But the droplets also breaks beyond the maximum limit of D_e (see Sect. 3.4.4), so that the distribution of hydrometeors size at ground is different from that aloft, which is sampled by weather radar. This means also that the difference between radar estimates and rain gauge measurements of rain increases as the range increases, due to the increasing impact of the air motion with increasing distance. In conclusion, the air motion has an impact on the vertical variability of the precipitation system, the *Z-R* relation (due to the variability of the DSD), and the differences between radar and rain gauge estimates of rain, that tends to be greater as the distance from radar increases.

4.2.5 – Ground clutter

The ground clutter is an intense non-meteorological radar echo caused by scattering in the antenna sidelobes hitting the ground close to the radar site as well as by fixed objects (e.g., buildings, trees, terrain) obstructing the radar beam. Non-meteorological echoes are still a significant problem, especially when they are embedded in meteorological returns, as they lead to a rain rate overestimation by the radar (Villarini and Krajewski, 2010). The ground clutter is removed through the methodology specified in the Chapter 4 (Lombardo et al., 2006).

4.2.6 – Beam-blocking

The beam-blocking, can be total or partial, and it is due to mountains or other obstacles that intercept the radar beam (Bringi and Chandrasekar, 2001). The total beam-blocking doesn't allow to the radar to detect the hydrometeors that are situated beyond the obstacles. But, the same particles could be collected by a rain gauge placed at the ground. Instead, the partial beam-blocking causes signal attenuation and, consequently, an underestimation of the rain rate by the radar with respect to the real rainfall field. Moreover, in the case of partial beam-blocking,

spurious returns occur, because the row reflectivity, that is the reflectivity without corrections (see Chapter 5), is affected by ground clutter, as showed by Fig. 4.2.

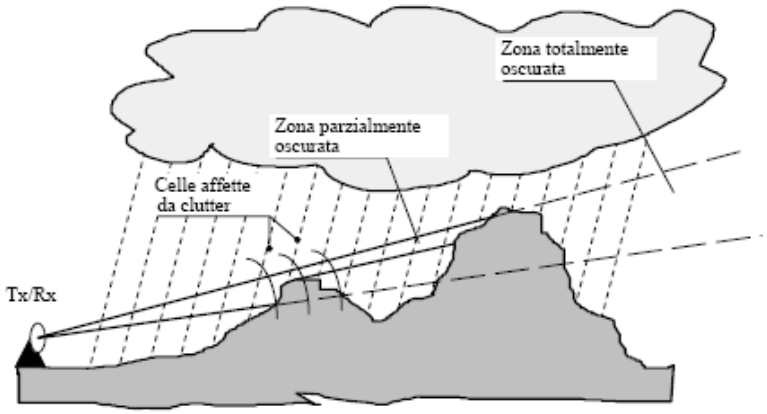

Figure 4.2 - Beam-blocking.

4.2.7 – Anomalous propagation

Since the atmosphere is a not-homogeneous medium, in which temperature, pressure, and humidity change with height, the atmosphere's index of refraction *n* decreases with height, and, therefore, the wave rays bending (or refraction) occurs.

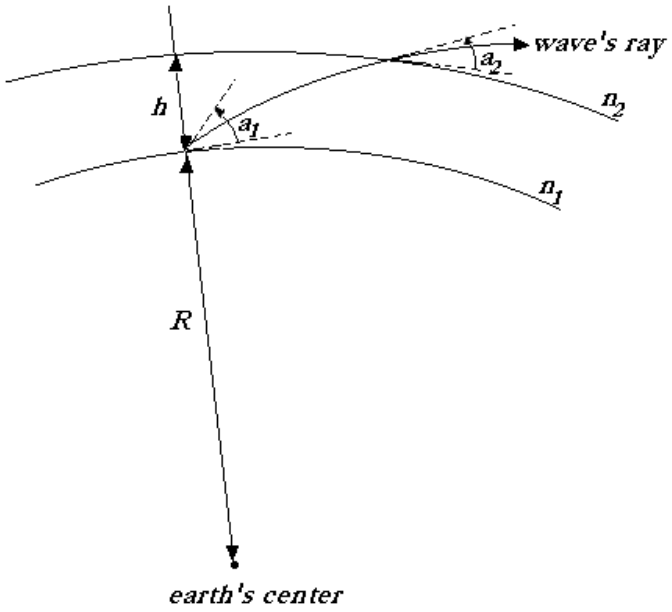

Figure 4.3 - Wave propagation in a standard atmosphere.

Considering a ray that propagates from a point P_1 on the surface of the earth, where the index of refraction is n_1, to a point P_2 above the surface at an altitude h, where refractive index is smaller and equal to n_2 (see Fig. 4.3), Snell's law states that:

$$n_2(R+h)\cos(a_2) = n_1 R\cos(a_1) \tag{4.1}$$

where R is the radius of the earth, and a_1 and a_2 are the angles between the ray and the local horizontals. As a consequence, when the altitude increases, for the same angle of incidence i, the refraction angle r decreases, and the ray bends downward. In fact, it results that:

$$n = \sin(i) \diagup \sin(r) \tag{4.2}$$

where n is the atmosphere's index of refraction, i and r are respectively the angle of incidence and the refraction angle with respect to the normal. In the standard atmospheric conditions n decreases linearly with altitude, and the paths of the waves are close to arcs of circumference not-concentric with respect to the earth. In not-standard atmospheric conditions, n changes not-linearly with the altitude. As a consequence, the waves diverge from their standard propagation direction. In this case, there is anomalous propagation consisting of abnormal bendings downward (superrefraction), or abnormal bendings upward (subrefraction). Superrefraction occurs in the presence of inversion at the ground, when the humidity decreases strongly with the altitude, or when warm and dry air moves on contact with cold water. Superrefraction occurs less frequently during storms too. Instead, subrefraction occurs for example in case of fog, or when cold air passes above a warm soil.

Moreover, in case of anomalous propagation the beam can be guided through a narrow layer along hundreds of kilometers. As a consequence, on a PPI display rain cells can be displayed which are situated in fact beyond the bound of the radar scanning circle.

4.2.8 – Signal attenuation

In this section the effects of both the signal attenuation and the phase shift of the waves will be examined. These effects are caused by the interaction between the waves and the medium precipitation along the propagation path.

Attenuation is a phenomenon which leads to a reduction of the power of an electromagnetic wave that propagates in a medium, and it is due to both the absorption and the scattering by the targets. In radar meteorology the attenuation causes the loss of a polarimetric wave's power when it propagates along a path through rain, and it is due partly to the absorption, partly to the scattering by the hydrometeors. Therefore, it causes a reduction of the power of the pulse which

passes through the hydrometeors, that depends on the type and density of the material, and on the frequency of the incident wave. In case of the weather radars working frequencies, the water absorption along the propagation path is the main cause of attenuation, which increases as the signal frequency increases. However, even at relatively low frequencies (S-band, f = 3 GHz), the radar signal can be affected by relevant two-path attenuation, which will considerably reduce the observed Z and thus the estimated R, when the waves propagate through very intense precipitations (as summer convective events). When the radar beam passes through an intense storm cell it is weakened and therefore the rainfall intensity due to the cell is underestimated (Pegram and Clothier, 1999).

Due to the effects of the airflow around the hydrometeors, falling raindrops have an oblate shape that becomes more pronounced as its size increases, being it preferentially oriented in the horizontal plane (see Sect. 3.4.4). This physical effect influences both the propagation of an incoming electromagnetic wave and the back-scattered wave. For this reason the radar echo from raindrops is larger in polarization H, than in polarization V. This effect is more evident as the size of the drops increases (Testud et al., 2000). A significant advantage of polarimetric radars is the possibility to measure the differential propagation phase shift φ_{DP} between H and V polarizations, which can be utilized for estimate the total attenuation along the propagation path through rain.

Apart from the weakening of the signal, the attenuation causes also a phase shift of the back-scattered wave. In fact, considering an incoming radioelectric wave, which is transmit by the radar with a certain polarization, and assuming a spherical shape of the hydrometeors, in a generic point P intercepted by the radar beam, it results that there is a phase shift between the back-scattered wave and that transmitted by the radar. The phase variation is due to the overlapping of the forward scattered wave with the incoming wave transmitted by the radar. These two waves have different origins, and, as a consequence, different phases. The phase shift is named propagation phase shift $\phi_{l,j}$ and it is a function of the polarization of the incoming electromagnetic wave transmitted by the radar, due to the fact that also the forward scattered wave's phase depends on it.

In case of linear orthogonal polarization, the differential propagation phase shift φ_{DP} is defined as the difference between the copolar propagation phase shifts, given by:

$$\varphi_{DP} = \phi_{hh} - \phi_{vv} \tag{4.3}$$

where ϕ_{hh} is the phase shift of the horizontal polarized wave, and ϕ_{vv} is the phase shift of the vertical polarized wave, being the effect more important in polar H than in polar V. This differential

effect is again due to the oblateness of raindrops (Testud et al., 2000). In case of spherical objects, the differential propagation phase shift φ_{DP} should be equal to zero because $\varphi_{hh} = \varphi_{vv}$.

Therefore, in case of motionless spherical object, the differential propagation phase shift φ_{DP} should be equal to zero, as well as the signal frequency variation. In case of spherical object which moves with respect to the radar location it would have only a frequency variation (Doppler effect). In case of motionless oblate object it would have a differential propagation phase shift different from zero, but a signal frequency variation equal to zero. In case of not-spherical object which moves with respect to the radar, it would have both a variation of the signal transmitted frequency and a different from zero φ_{DP}.

Only φ_{DP} can provides a measure of the along-path attenuation because both it is a cumulative quantity, which increases as the distance from radar increases, and it doesn't suffers the effects of attenuation due to propagation through rain or beam-blocking. The φ_{DP} measured in a generic point intercepted by the radar beam takes into account of the total attenuation along the path from the radar antenna site until the considered point.

Being P_1 and P_2 two points at distances r_1 and r_2 from the radar site, both located along the same ray, it is defined the specific differential propagation phase shift K_{DP} as follows:

$$K_{DP} = \frac{\varphi_{DP}(r_2) - \varphi_{DP}(r_1)}{2(r_2 - r_1)} \tag{4.4}$$

where φ_{DP} is the differential propagation phase shift. K_{DP} is a very important parameter because it can provide rain rate estimates (see Sect. 5.4.1) as it is nearly proportional to the rainfall rate, and the relation $R(K_{DP})$ is only slightly dependent on the drop size distribution. So, the K_{DP} algorithm behaves better than the classic with the Marshall–Palmer DSD because it is not affected by attenuation (Testud et al., 2000). Moreover, K_{DP} allows for identifying the structure of the scattering medium (for example, the location of heavy precipitation regions), and of the water content in a liquid state (Doviak and Zrnić, 1993), that is the body of water in a unit volume.

Assuming oblate hydrometeors, it follows that the differential propagation phase shift φ_{DP} between copular signals received by the radar is (Bringi and Chandrasekar, 2001):

$$\psi_{DP} = \varphi_{DP} + \delta_{co} \tag{4.5}$$

where $\delta_{co} = \delta_{vv} - \delta_{hh} \approx 0°$ assuming valid the Rayleigh-Gans approximation, δ_{ij} is the phase of the coefficient s_{ij} of the back-scattering matrix.

4.2.9 – Radar miscalibration

The radar miscalibration is the source of an uncertainty in radar estimates of rain rate named bias. The bias is a systematic error which occurs whenever the weather radar makes a measure of back-scattered power, apart from the location of the sampling volume. Once the radar is correctly calibrated, it is able to measure exactly the back-scattered power that remains, however, affected by the signal attenuation and the other sampling errors. In fact the bias is independent from other types of errors. The calibration is the procedure that allows to obtain the system bias, and consist of modify the radar constant so that the systematic error which affects the reflectivity can be compensate (see Eq. (3.18)). The bias must be added to reflectivity factor Z (dBZ).

The bias can be determinated through several methodologies:

- use of standard targets;
- receiver static calibration;
- use of the sun as source of energy;
- calibration of radar using polarimetric techniques (self-consistency principle);
- calibration with rain gauges (Koistinen e Puhakka, 1986; Saltikoff et al., 2000; Russo, 2004).

The receiver static calibration consists of injecting pulses of know amplitude, and, subsequently, measuring the power detected by the receiver, which is different from the transmitter pulse power (Bringi and Chandrasekar, 2001).

The calibration of radar using polarimetric techniques is based on the principle that the rainfall rate estimated by using the reflectivity factor at horizontal polarization Z_h and the differential reflectivity Z_{DR} is the same as that obtained from specific differential phase K_{DP}. Scarchilli et al. (1996) have showed that Z, Z_{DR}, and K_{DP} lie in a three-dimensional space. This constraint permits the parametrization of K_{DP} in terms of Z_H and Z_{DR}. In other words, K^*_{DP}, which is the parameterized estimate of K_{DP} based on Z_H and Z_{DR}, can approximate K_{DP} fairly well in the absence of measurements errors. To calibrate Z_{DR} measurements vertical-looking radar observations are used. K_{DP} is derived from the differential phase measurement Φ_{DP}, which is unaffected by systematic errors (Gorgucci et al., 1999). This means that any bias in the absolute calibration (error on the radar constant) translates into a bias in all the measured values of the reflectivity Z_h. In the absence of bias in a scatter plot of K_{DP} and K^*_{DP} the slope of the regression line is about 45°. However, in the presence of bias the angular deviation of the best fit line from 45° is a measure of the bias (Gorgucci et al., 1992; Gorgucci et al., 1999).

The calibration that uses rain gauge measurements can integrate other kind of calibrations, improving the precision in the bias estimate, and it is based on the assumption that the rain field derived from rain gauges measurements is real. Once the bias is added to reflectivity, the rain gauge measure R_{pluv} must be equal to the corresponding radar estimate, that is:

$$R_{pluv} = a \cdot 10^{(b(Z+C)/10)} = a \cdot 10^{(bZ/10)} \cdot 10^{(bC/10)} \tag{4.6}$$

where Z is the reflectivity factor (dBZ), C is the bias, while a and b are the coefficients of the assumed Z-R relation (see Eq. (5.11)). The terms $a \cdot 10^{(bZ/10)}$ represents the rain rate (mm/h) estimated by the radar and the factor $10^{(bC/10)}$ is a dimensionless multiplicative error obtained as follows:

$$M = \frac{\sum_{i=1}^{E}\sum_{j=1}^{P} G_{i,j}}{\sum_{i=1}^{E}\sum_{j=1}^{P} R_{i,j}} \tag{4.7}$$

where $G_{\text{i,j}}$ and $R_{\text{i,j}}$ are the rain gauges and the radar rainfall amount respectively for i-th event and j-th rain gauge, E is the number of rainfall events observed, P is the number of rain gauges utilized. The simplest method is to calculate the mean bias by considering all the rain gauges scattered along the catchment (Russo, 2004). Or alternatively rain gauges can be selected so that radar errors in rain gauges sites are likely due only to radar miscalibration, to avoid the influence of the other kinds of errors on bias calculation (Sebastianelli et al., 2013). In any case the same M is applied uniformly to each rainfall value estimated by the radar in the scanning area. The existence of a multiplicative bias that characterizes the Z-R relation is the same as a bias C (dB) which must be added to reflectivity Z. C can be calculated as follows (Russo, 2004):

$$C = \frac{10}{b}\log_{10}(M) \tag{4.8}$$

where b has the same meaning as in Eq. (4.6). C is a factor that must be added to the reflectivity data to correct the effects of radar miscalibration.

By utilizing Eq. (4.6) each rain gauge has a weight proportional to the precipitation amount collected. Alternatively, M can be calculated as in Eq. (4.8) so that each rain gauge has the same weight in the bias determination:

$$M = \frac{1}{E \cdot P}\frac{\sum_{i=1}^{E}\sum_{j=1}^{P} G_{i,j}}{\sum_{i=1}^{E}\sum_{j=1}^{P} R_{i,j}} \tag{4.9}$$

Chapter 5

The Polar 55C weather radar

5.1 – Features presently available in the Polar 55C radar

Precipitation data processed in the present work are collected by the Polar 55C weather radar. The Polar 55C is a coherent C-band (5.6 GHz) Doppler dual polarization weather radar, with polarization agility, managed by the CNR-ISAC (Institute of Atmospheric Sciences and Climate of the National Research Council) in Italy (Gorgucci et al., 2002). Since it is a Doppler radar, Polar 55C is able to measure in real time the variations of the signal received phase, from which the mean radial velocity of the hydrometeors depends. Therefore it can measure the mean velocity (v) and the second central moment of the Doppler Spectrum (σ_v). Moreover, Polar 55C is capable of transmitting and receiving horizontally and vertically polarized signals on alternate pulses providing, among others, in real time measures of Reflectivity Factor (Z_h), Differential Reflectivity (Z_{DR}) and Differential Phase Shift (Φ_{DP}). The radar beam has an azimuth beamwidth of 0.92° and an elevation beamwidth of 1.02°. Radome is not used in order to avoid beam blocking by stalls, even if it would increase the stress of the mechanics of the servo antenna. The frequency of the signal emit belong to the C-band (5.5 GHz, λ = 5.4 cm), that, in Europe, is considered as the better compromise between the problems due to the antenna's dimensions (as already mentioned in Sects. 2.7 and 3.3, radars with a great wavelength are much expensive because they need a great antenna to focus the beam) and the accuracy in the rainfall estimates, mainly concerning the signal attenuation. In Tab. 5.1 features of Polar 55C radar are summarized.

Antenna	
Type	Offset fed Paraboloid
Feed	Corrugated horn
Aperture diameter	4.57 m
Polarization	Horizontal and Vertical
Azimuth beamwidth	0.92 deg
Elevation beamwidth	1.02 deg
Gain	45.5 dB
Sidelobe level	-32 dB
Cross Polarization	-27 dB
Transmitter	
Power Amplifier	Klystron VCK 7762
Frequency	Fixed, selectable in the band 5600-5650 MHz
Peak Power	500 kW
Pulse width (maximum)	0.5 – 1.5 - 3.0 μs
PRF	1200 – 600 – 300 Hz
Average Power	300 – 450 – 450 W
Available polarizations	H and V
Receiver	
Number of channels	2: (RX and TX sample down conversion to IF)
Noise figure	2.0 dB from the input of the first down conversion module.
Image Rejection	> 50dB
Dynamic range	> 100dB at 1dB compression
IF	60 MHz
IF bandwidth	2.0 – 0.7 – 0.5 MHz

Table 5.1 – Features of Polar 55C weather radar.

5.2 – Location of Polar 55C weather radar

Polar 55C weather radar is located 20 km South-East of downtown Rome and installed on the roof of the tower of the ISAC building. The exact position of the Polar 55C corresponds to North Latitude 41.84°, East Longitude 12.65° and a height of 102 m ASL. Figure 5.1 shows the buildings of the Tor Vergata Research area surmounted by the Polar 55C antenna.

From the current site, the Polar 55C can monitor precipitation over the farthest part of the Tevere basin, the urban area of Rome, and the central Apennines. Figure 5.2 shows the Polar 55C position in relation to the Rome urban area (grey line), the hydrographical network of the Tiber River (blue lines), the Lazio region boundary line (in black) and the coast-line. The black rings in Fig. 5.2 represent points at the same distances from Polar 55C, that is at 40 km, at 80 km and at 120 km from radar.

Figure 5.1 – Polar 55C antenna installed over the top of the building of ISAC, in the Tor Vergata Area of the National Council of the Research.

The position of Rome can be referenced by the grey circle, which represents the highway that surrounds it.

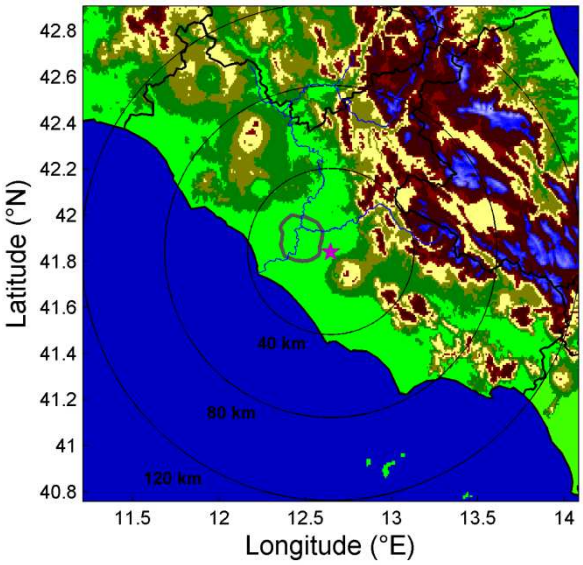

Figure 5.2 – Polar 55C scanning area.

The observable region includes a mountainous districts, due to the presence of several mountain chains (the Colli Albani Hills, the Prenestini Mountains, the Tiburtini Mountains and the Sabini Mountains), which cause limitations to visibility. When the beam is completely blocked by mountains there will be no radar echo received from the farther targets in the range, and this

feature can easily be spotted on radar pictures. However, when the beam is partially blocked the echo received from the ranges farther than the blocking target will be reduced and the radar reflectivity (Z_h) will also be correspondingly reduced proportionally to the amount of the beam blockage. Particularly, as showed in Fig. 5.3, the occultation constituted by Monte Cavo (which belongs to the Colli Albani Hills) is total and determines the presence of an occulted sector, from 120 to 150° recognizable in the map. Good visibility in the North West sector allows the monitoring of precipitation over the Tyrrhenian Sea, which is very important in order to understand the advection of the precipitation to the urban area of Rome and to predict incoming precipitation cells over that area. In spite of mountains, which determine the limitation in radar visibility of the region in some sectors, it is possible to achieve a good monitoring of precipitation in the Apennines Mountains, where interesting observations of convective storms, which frequently occur there during the summer, can be made. Figure 5.3 provides an example of reflectivity map observed at an elevation angle of 1.50° on 19 September 2008.

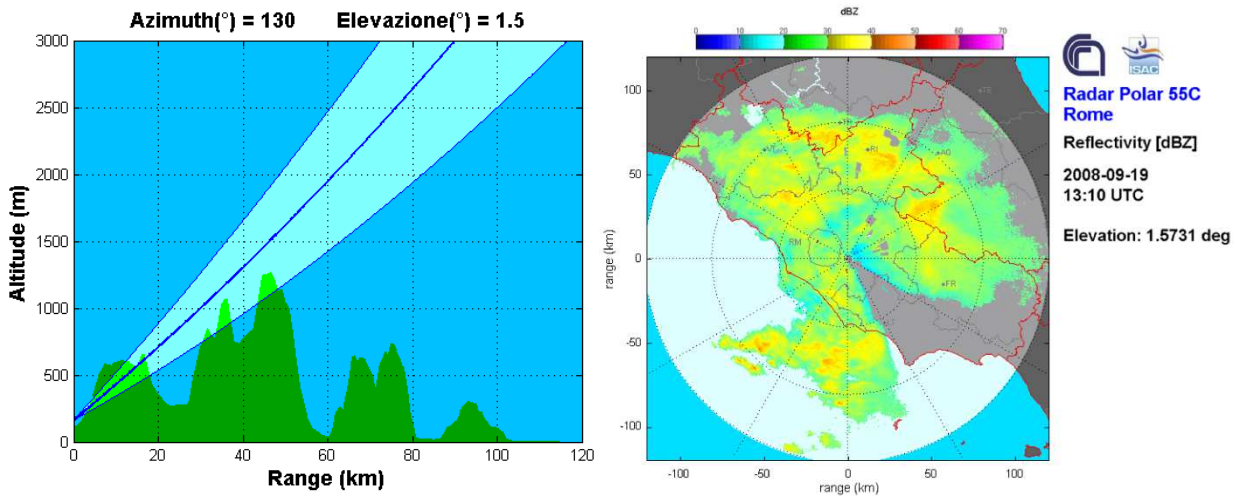

Figure 5.3 – Total beam-blocking (right panel) and a reflectivity map (PPI) oh the 19th September 2008, collected by the Polar 55C weather radar. It is evident the beam-blockage phenomenon in the South-Eastern region caused by the Cavo mountain.

5.3 – Data acquisition

In the considered data sets, radar measurements are obtained by averaging from 48 to 64 pulses transmitted with a 1200 Hz pulse repetition frequency with a range-bin resolution of 75 m, up to 120 km away from the radar location (Gorgucci et al., 2002).

Since Polar 55C is not an operational weather radar, different scanning strategies are adopted, depending on the information requested about the hydrometeors. The Polar 55C can acquire data

through two different observation methods: the Plan Position Indicator (PPI) observation, based upon the cyclical repetition of a certain number of sweeps, each one with a constant elevation, ranging upward from two bounds, and the Range Height Indicator (RHI) observation, when the azimuth is kept constant while at the same time the elevation angle changes. In this work, only the first one is employed and the number of sweeps as well as the antenna angles is scheduled; elevation angles and scanning time are set according to the priorities of the ongoing research activity. This study considers positive antenna elevation angles that allow satisfying the need to minimize the influence of ground-clutter and the contrasting need to keep the radar beam close to the ground (Gorgucci et al., 1995; Russo et al., 2005; Lombardo et al., 2006; Russo et al., 2006). Furthermore, the radar operational elevation angles for precipitation estimation are chosen so that the effect of both the melting layer contamination and the beam geometry could be studied.
Figure 5.3 shows an example of PPI, which returns on a plane the images of the received signals in a polar coordinate system (Russo, 2004). On a PPI it can be viewed in real time the position of a meteorological target, in terms of both distance from radar and azimuth, and, moreover, the precipitation is represented by different colors depending on the rainfall intensity.
The time needed to acquire a PPI is about 40 sec, as the antenna moves with a constant velocity of about 12 deg/sec. As a consequence, the time that passes between the acquisitions of two consecutive PPI with the same elevation depends on the number of elevation angles scheduled.

5.4 - Ground clutter and noise rejection

To process radar data two essential steps must be carried out, which are necessary to allow the use of the information given by the radar data, that is the distinction between both meteorological echoes and noise, and meteorological echoes and ground clutter. To reach these aims, apposite methodologies are developed. The potentiality of the dual-polarized weather radar is employed, in order to reject the ground-clutter, using differential reflectivity (Lombardo et al., 2006).
Polar 55C radar data are collected without filtering out noise. In this way it is possible to determine the level of background noise in each radar reflectivity map by considering that at far distances from the radar, and even for small elevations, the radar samples in an atmospheric region above the layer of precipitation. As a consequence, the modal value in the last two range-bins can be used as a reference to determine the noise level at the receiver. Therefore, using reflectivity factor at such distances, the noise level Z_S in dBZ at a given range r can be expressed for a given azimuth by Eq. (5.1) as follows:

$$Z_s(r) = Z_f + 20 \cdot \log_{10}\left(r / r_{end} \right) \quad (5.1)$$

where in the second term in the right side r_{end} is the maximum range (120 km) and Z_f is the modal value (determined as described previously) at the farther two range bins (1 range-bin = 75 m) of each record. Along a ray, each measured Z_h value at the distance r is compared with the Z_S value at the same distance, and the range-bins whose reflectivity does not exceed the noise level by a threshold of 4 dB are considered as affected by noise. This method allows both monitoring of the noise level of the system and identifying of returns with a signal to noise ratio above a given threshold T. If $Z_h(r) < Z_s(r) + T$, being T = 4 dB (used to take into account residual fluctuations and quantization error), the measurements at range r are suppressed. Figure 5.4 shows an example of reflectivity trend (in blue) and noise level trend (in red) against range along a generic ray. After removing noise, it needs to identify the cells contaminated by ground clutter. Ground clutter is generally defined as an intense radar return from non-meteorological, ground-based targets, such as mountains, buildings or other human artifacts. These obstacles cause locally a rainfall intensity overestimation by the radar with respect to the real rainfall field. Ground clutter effects are more evident when low elevation angles are used since the radar energy travels close to the earth's surface especially at closer ranges. The presence of clutter is easily recognizable on plan position indicators, because its position is fixed.

The method developed to identify and remove range-bins affected by ground clutter is based on the existence of typical values for the standard deviations of the differential reflectivity $\sigma(Z_{DR})$ and of the differential phase shift $\sigma(\Phi_{DP})$ when the radar return is caused by precipitation (Bringi and Chandrasekar, 2001; Russo et al., 2005; Lombardo et al., 2006). In fact, in the presence of meteorological echoes these standard deviations can be expressed in terms of both the Doppler spectrum width (σ_v) and the co-polar correlation coefficient ρ_{hv}. Therefore, using the ranges of σ_v and ρ_{hv} in precipitation it is possible to define the corresponding boundaries for $\sigma(Z_{DR})$ and $\sigma(\Phi_{DP})$. If values of $\sigma(Z_{DR})$ and $\sigma(\Phi_{DP})$ lie outside these boundaries, measurement is considered as belonging to a clutter contaminated volume. The following conditions are established, which are necessary so that the signal at the receiver is scattered by a meteorological target:

$$0.09dB < \sigma(Z_{DR}) < 0.9dB, \sigma(\varphi_{DP}) < 5^{\circ} \quad (5.2)$$

Only the radar data not affected by ground clutter or noise are converted to rainfall rates, as explained in Sect. 5.4.2.

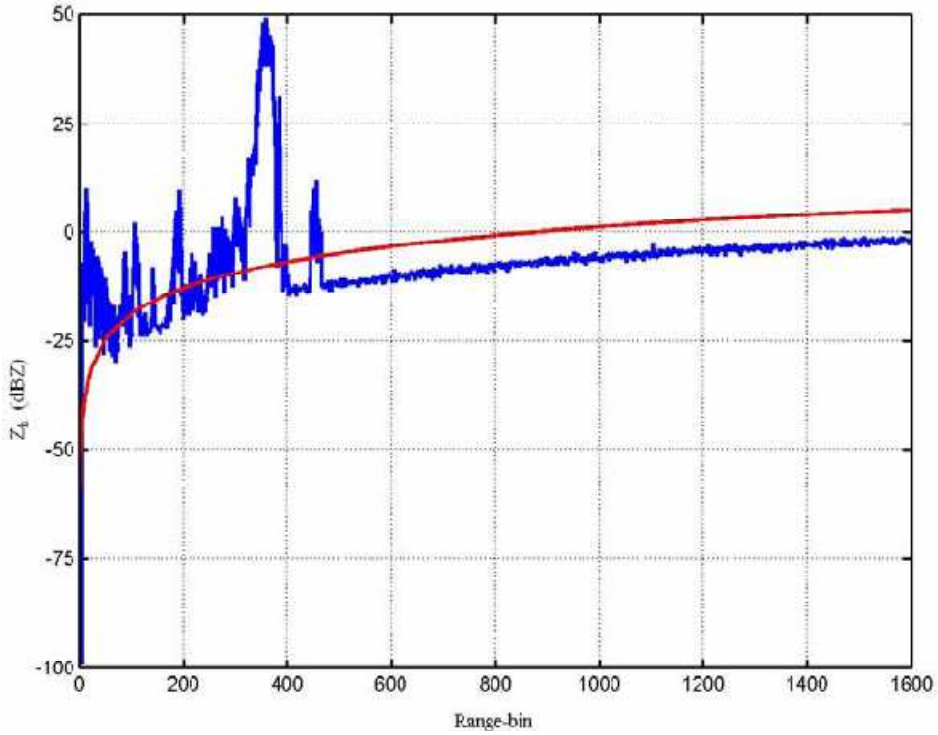

Figure 5.4 – Reflectivity (Z_h) and noise level (Z_S) patterns on a generic azimuth.

Figures 5.5a, 5.5b and 5.5c show reflectivity maps collected at the same time but referring to different processing levels, named row reflectivity, after removing noise and after removing noise and ground clutter. In Figs. 5.5a and 5.5b sectors affected by ground clutter are represented on a PPI through a dark red color. Finally, Fig. 5.5d shows the corresponding rainfall intensity map, in which it can be seen that meteorological echoes are returned with a color ranging from dark blue (drizzle) to light red (heavy rainfall) or dark red (hail).

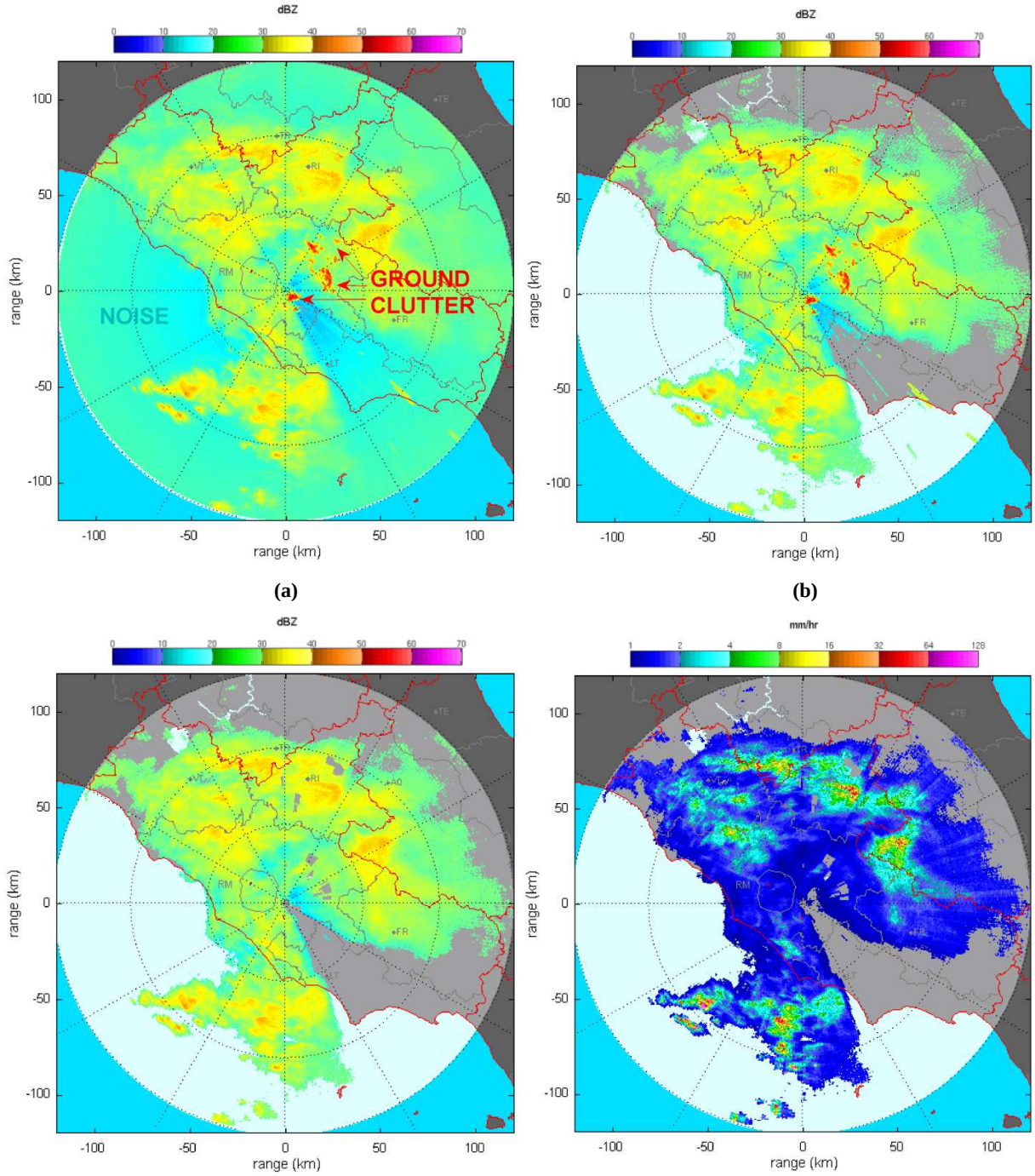

Figure 5.5 – Row reflectivity, reflectivity after removing noise, reflectivity after removing noise and ground clutter and corresponding rainfall intensity map (from the left to the right and from up to bottom), collected during the 19 September 2008 event.

5.5 - From reflectivity to rainfall intensity

5.5.1 – Physically based parametric rainfall intensity estimation algorithms

Two kinds of methodologies used to estimate rain rate from radar data exist: physically based and statistical-engineering procedures (Bringi and Chandrasekar, 2001).

Physically based rainfall algorithms are employed to obtain rain rate (which is averaged in each sampling volume) from both physical models of precipitation and corresponding polarimetric measurables, without any feedback from rain gauge measurements. The aim of statistical-engineering solutions is to obtain the better rainfall intensity estimation, by utilizing both radar data and rain gauge data (Zawadzki, 1984; Ehret, 2002; Sinclair and Pegram, 2005). Only the first one is considered in this section.

The drop size and shape distribution is of fundamental importance to obtain the physically based rainfall algorithms. The drop size distribution (DSD) depends on the probability density function of the raindrops. A gamma distribution model is able to adequately describe many natural DSD shape variations (Ulbrich, 1983). The gamma DSD is expressed as follows:

$$N(D) = n_c \, f_D(D) \tag{5.3}$$

where *N(D)* is the number of raindrops in the unit volume and for dimensional interval (*D*, *D*+*ΔD*), n_C is the concentration, and $f_D(D)$ is the probability density function. For a gamma distribution model:

$$f_D(D) = \frac{\Lambda^{\mu+1}}{\Gamma(\mu+1)} e^{-\Lambda D} D^{\mu} \tag{5.4}$$

where Λ and $\mu > -1$ are the gamma probability density function parameters. It can be demonstrate that the polarimetric measurables depend on the raindrop size and shape distribution. To estimate rainfall Z_{DR} and K_{DP} can be expressed as integrals over the DSD of both the back-scattering and forward-scattering amplitudes. Therefore, it has that (Bringi and Chandrasekar, 2001):

$$Z_{DR} = 10\log_{10}\left[\frac{\int \sigma_{hh} N(D) dD}{\int \sigma_{vv} N(D) dD}\right]; [dB] \tag{5.5}$$

where $\sigma_{hh} = 4\pi|s_{hh}|^2$ and $\sigma_{vv} = 4\pi|s_{vv}|^2$ are the radar cross sections at the horizontal and vertical polarization respectively. Similarly, it can demonstrate that:

$$K_{DP} = \frac{180\lambda}{\pi} \int \mathrm{Re}\left[f_h(D) - f_v(D)\right] N(D) dD; \left[^{\circ} km^{-1}\right] \tag{5.6}$$

where f_h and f_v are the forward-scattering amplitudes at the horizontal and vertical polarization respectively. Moreover, being a flow of water per unit area it can demonstrate that also the rain rate depends on the DSD. In fact the rain rate aloft without air motions is equal to:

$$R = 0.6\pi 10^{-3} \int v(D) D^3 N(D) dD \qquad (5.7)$$

where *v(D)* is the drop terminal velocity (see Sects. 2.4.1 and 3.4.4), which depends on the raindrops density, area, and shape. This velocity can be approximated through a power low relation as follows:

$$v(D) = \alpha D^{\beta}; \left[m\, s^{-1}\right] \qquad (5.8)$$

where D is measured in mm and α = 3.78 and β = 0.67 to obtain estimates of R at the sea level (Atlas and Ulbrich, 1977).

Several physically based rainfall algorithms are developed depending on the polarimetric measurements utilized in the estimation. As already mentioned (see Sect. 4.2.2) the DSD varies geographically, depending on the characteristic of the rainfall event and, within the same rain field, on the rainfall intensity. Moreover, the DSD influences the coefficients of the *Z*-*R* relationship (Villarini and Krajewski, 2010). Once a drop size distribution (DSD) is selected, it is possible to express the relation between reflectivity and rainfall rate using a power-law relation. The oldest and simplest physically based rainfall algorithm is the relation *Z*-*R*:

$$R(Z) = a\, Z^{b}; \left[mm\, h^{-1}\right] \qquad (5.9)$$

where Z is the reflectivity factor (mm^6 m^{-3}), R is the rainfall intensity (mm h^{-1}) and the ranges of parameters a and b reported in literature are very large (Battan, 1970). The most well-know relation based on Marshall-Palmer DSD is given by:

$$R_{MP}(Z) = 0.0365\, Z^{0.625}; \left[mm\, h^{-1}\right] \qquad (5.10)$$

$R(Z)$ is the most commonly used algorithm because most radars operate at one polarization.

Radar rainfall algorithm can be classified principally into four categories, namely: $R(Z)$, $R(Z, Z_{DR})$, $R(K_{DP})$, and $R(K_{DP}, Z_{DR})$. Reflectivity-based algorithms require accurate knowledge of the radar constant C (Eq. 3.16) and are prone to errors in absolute calibration (see Sect. 4.5). Since differential reflectivity Z_{DR} is a relative power measurements, it is not affected by absolute calibration errors. But Z_{DR} needs to be used together with Z_h or K_{DP}. Algorithms based on K_{DP} have several advantages (see Sect. 4.2.8) due to the fact that being K_{DP} derived from phase measurements, it is not affected by absolute calibration errors and along-path attenuation (Testud et al., 2000). Moreover it is unaffected also by attenuation due to partial beam-blocking. However, K_{DP} is relatively noisy especially at low rainfall intensities.

5.5.2 – Algorithm used to rainfall estimation with Polar 55C radar data

To convert reflectivity Z_h (dBZ) into rainfall intensity R (mm/h) a Z-R physically based rainfall algorithm is used, as follows:

$$R(Z) = a10^{(bZ_h/10)}; \left[mm\,h^{-1}\right] \quad (5.11)$$

where a = 0.19055 and b = 0.5358. Coefficients of this algorithm are determined through simulations (Russo, 2004; Sebastianelli et al., 2013), assuming a theoretically derived distribution of the Drop Size Distribution (DSD) parameters, the drop shape model of Pruppacher and Beard (1970), a fixed temperature of 20°C and the distribution of canting angle (Bringi and Chandrasekar, 2001). Only reflectivity due to meteorological echoes is converted into rain rate by Eq. (5.5). Whereas, range-bins affected by ground clutter or noise are not considered to estimate the rainfall intensity.

5.5.3 – From Cartesian to polar coordinate

Finally, radar rainfall intensity maps are obtained by remapping radar polar range-bins onto a 1 km^2 Cartesian grid (Sebastianelli et al., 2013). A radar rainfall map consists of 240 x 240 values of rain rate (mm h^{-1}), each of which pertains to one of the pixels of a Cartesian grid. The single pixel is a square of side 1 km. However, the radar obtains a reflectivity value for each sample volume (range-bin). The sampling volume has a fixed length of 75 m, but it has a width and a thickness that depend on the distance from the radar. Consequently, for each pixel the range-bins that pertain to it have been identified. Then, the rain rate of the pixel is determined by calculating the average of the rain values of the sampling volumes including inside it. The calculation of mean value does not take into account the range-bins affected by ground clutter or noise.

Chapter 6

Applied methodology to improve Polar 55C estimates' quantitative accuracy

6.1 – Gauge adjustment of radar data techniques

The adjustment to rain gauge measurements methods are widely used to improve the radar estimate's quantitative effectiveness. All of them are based on the calculation of the ratio between rain gauge readings (*G*) and the corresponding radar estimates (*R*), which is used to correct the errors induced by various sources of uncertainties, such as the incorrect *Z-R* relationship, beam-blocking, attenuation, radar miscalibration, and VPR. Gauge adjustment includes any procedure whereby the characteristics of radar data are modified such that they correspond as well as possible with the quantity given by gauge measurements (Gjertsen et al., 2004). In fact, the radar provides information on the spatial distribution while the gauge provides a point measurement of relatively high quantitative accuracy (see Chapter 3). The gauge adjustment changes the multiplicative factor in the *Z-R* relationship, which depends on precipitation type (Saltikoff et al., 2000; Seo et al., 2000; Gjertesen et al., 2004). Therefore, the initial choice of the *Z-R* relationship is not critical when a gauge adjustment is applied. Gauge adjustment approaches vary throughout Europe. They are based on various assumptions. It is crucial for the success of the adjustment that the gauge data used as reference are of good quality. Radar successfully measures relative spatial and temporal variability of precipitation, by identifying and removing noise, clutter, and correcting for missing echoes where the beam is blocked or overshooting the precipitation. Gauge and radar measurements must be valid for the same locations in time and space. Although the latter is not true, the influence of the temporal and spatial sampling errors (Villarini and Krajewski, 2010) can be minimized by selecting the appropriate spatial and temporal scale for the adjustment. In fact, the *G*/*R* factor (Sect. 6.3.2) becomes naturally more stable for longer integration periods and more gauge data available. Relationships based on comparisons between gauges and radar must be valid for other locations in space and/or time. This assumption also is not true due to the fact that the reflectivity profile is highly variable in time and space, especially in convective situations. Moreover, as already explained in Sects. 2.5 and 4.1, in mountainous regions, the spatial representativeness of a gauge

may be low due to the dominating influence of topography on the precipitation distribution (Gjertsen et al., 2004).

The ratio between rain gauge readings and the corresponding radar estimates has been often employed to correct the main field bias due to uncertainties in the *Z-R* relationship and system non-optimal calibration. Main field bias adjustment is the simplest method. However, its use is reasonable only at short ranges, where the effects of range degradation are negligible and, therefore, the *G*/*R* ratio is relatively low and constant, or if a dense rain gauge network is available in the radar domain. If the *G*/*R* ratio varies too rapidly with distance other compensating procedures must be applied, like the VPR correction.

Because of the geometric characteristics of the radar sampling and the non-uniform VPR, radar rainfall estimates are subject to biases that are necessarily range dependent (Seo et al., 2000; Borga and Tonelli, 2000; Vignal et al., 2000; Vignal et Krajewski, 2001; Krajewski et al., 2011). As already mentioned in Sect. 4.2.3, the VPR describes the ratio between reflectivity at a given altitude and reflectivity at the ground (that is at lowest elevation), and it is usually employed to characterize vertical variability. It can be deduced from radar data recorded at different elevation angle, combining various measurements altitudes. The VPR structure depends on seasonal and regional regimes, precipitation type, and atmospheric conditions (Krajewski et al., 2011). The sources of non-uniform VPR are: phase change of hydrometeors (i.e., from frozen to liquid) in stratiform storms, low-level growth of liquid hydrometeors in ''tropical'' storms, bright band enhancement at close–range, beam overshooting, evaporation below the cloud base, orographic enhancement, and sampling of ice particles above the freezing level at far-range which causes a radar underestimation of rainfall (Seo et al. 2000). These errors can be corrected by using the VPR to extrapolate radar data to the ground level. The VPR is frequently utilized to compute a multiplicative correction factor which must be applied to the rain rate measured by the radar at a certain location and elevation angle, to obtain the true radar rainfall value extrapolated to the lowest radar beam for the same location (Borga and Tonelli, 2000; Vignal et al., 2000; Vignal et Krajewski, 2001; Krajewski et al., 2011). The basic assumption of this method is the spatial invariance of the VPR over the studied domain, which permits separation of horizontal and vertical variations of the reflectivity. Moreover, the method allows taking care of variations of the profile in space as well as in time. Local profiles are retrieved in areas of about 20 x 20 km^2, which differ from the true profiles due to the smoothing effect of the radar beam at farther range. Then, the true profile can be retrieved using an inverse method described by Andrieu and Creutin (1995). The net effect sought by the procedure is equivalent to estimating and applying, as a

function of elevation angle and range, a multiplicative adjustment factor to the multiplicative constant in the reflectivity–radar rain rate (*Z–R*) relationship in real time (Seo et al. 2000; Borga and Tonelli, 2000). The literature offers a number of procedures for real-time adjustment of range-dependent biases in radar rainfall estimates due to non-uniform VPR (Seo et al. 2000; Borga and Tonelli, 2000; Vignal et al., 2000; Vignal et Krajewski, 2001; Gjertsen et al., 2004; Zhang et al., 2008; Zhang and Qi, 2010; Krajewski et al., 2011).

Because range-dependent bias adjustment is based solely on radar data, the adjusted radar rainfall estimates in general are subject to mean-field bias due to uncertainties in the *Z–R* relationship and, if it exists, the lack of radar hardware calibration. For this reason, the procedure for removing range-dependent bias, in general, must be followed by a procedure for mean-field bias removal based on real-time rain gauge data, which is equivalent to real-time adjustment of the multiplicative constant in the *Z–R* relationship. Therefore, accurate prior knowledge of the *Z–R* relationship is not as critical (Seo et al. 2000). For this reason, mean errors can be removed from the adjusted radar rainfall accumulations with respect to the corresponding rain gauge measurements by multiplying the radar rainfall accumulations by the ratio of the sum of gauge rainfall accumulations to that of adjusted radar rainfall accumulations. Then, from this ratio the multiplicative constant in the *Z–R* relationship can be estimated (Seo et al., 2000; Borga and Tonelli, 2000; Gjertsen et al., 2004; Krajewski et al., 2011).

To mitigate the effects of orography on radar estimates a Weighted Multiple Regression (WMR) method allows the correction of each radar pixel by analyzing the space variability of an assessment factor, in terms of distance from radar, the minimum height above the sea level that a target must reach to be visible from the radar and the ground height (Gabella and Amitai, 2000; Gabella et. al., 2001; Ozturk and Yilmazer, 2007). The assessment factor is calculated for each radar-gage data pair as the ratio between radar rainfall amount and the corresponding rain gauge rainfall amount, collected during a given integration interval.

Range dependent gauge adjustment techniques classify the *G*/*R* pairs into range bins (see Chapter 4) and derive the adjustment factor as a function of distance from the radar. The underlying assumption is that the differences between radar and gauge precipitation totals contain an inherently strong range dependency, according to the latter assumption above-mentioned. Therefore, issues like the beam blockages, the signal attenuation, the VPR related error, the bright band, the water phase of precipitation are implicitly treated with this type of method. The performance of a range dependent adjustment method depends, like the performance of a VPR correction, on the maximum height of the precipitation with respect to the

radar sampling altitude at the rain gauge locations, which depends on the scan elevations. For example, a limiting factor is the shallowness of stratiform precipitations, which occur especially in cold season (Gjertsen et al., 2004).

The topic of the present work is the assessment of the overall range-dependent error (RDE) which can be expressed as a function of the slant range through an adjustment factor (*AF*), that can be used as a range error pattern, allowing to correct the mean error affecting long-term quantitative precipitation estimates (QPE). Processing of data is performed by two separate analyzes. A range dependent gauge adjustment technique is applied in combination with other processing of radar data (Gjertsen et al., 2004) for both analyses.

A first analysis computes RDE as a function of slant range due to the effects of the range degradation (beam broadening and sampling precipitation at increasing altitude, which include beam overshooting and sampling of ice particles above the freezing level), as well as of other sources of uncertainties such as path attenuation, radar sampling precipitation within the melting layer, and the VPR structure. The methodology is coupled with a radar calibration performed with rain gauge data. A subsequent analysis is performed to highlight the effect of the attenuation, and consists of a gauge adjustment technique coupled with two processing of radar data performed previously, that is firstly a procedure to remove the signal attenuation, and, subsequently, a radar calibration with rain gauges. In both analyses, the overall error can be modeled through an *AF* depending on the range. In order to reach this objective, comparison between radar and rain gauges rainfall fields is done, based on the assumption that gauge rain is real (see Chapter 3). This hypothesis is formulated because a rain gauge can directly measure the rain, whereas weather radar derives rain rate from back-scattered power measurements. As a consequence, radar error is determined with respect to rain gauges measurements. The *G*/*R* ratio computation between radar estimates and corresponding rain gauge measurements (mm) is made at different distances from radar (see Sect. 6.3). Since the spatial differences between radar and rain gauges samplings (radar samples in a volume aloft while rain gauge data are collected in a point when the raindrops reach the ground) affect the comparison between the two devices, a whole year of measurements is used to estimate the *G*/*R* ratios. In fact, as above-mentioned, the *G*/*R* ratio becomes more stable for longer accumulation times, because the influence of uncertainty caused by mismatches in time and space performed by the two devices is reduced (Gabella and Amitai, 2000; Gabella et al., 2001; Gjertsen et al., 2004; Ozturk and Yilmazer, 2007). Errors arising from orography are not considered.

6.2 – Adjustment procedure

The adjustment procedure of radar data considered in this section consists of three different processing levels, namely without any correction, after radar calibration and after the adjustment procedure. After having identified and removed ground clutter and noise, radar calibration with rain gauges is performed. Finally, the gauge adjustment method is employed to find the *AF*, which takes into account the effects of the range degradations (due to the radar beam geometry), the signal attenuation, as well as residual sources of uncertainties such as radar sampling precipitation within the melting layer and the non-uniform VPR. For each processing level, the correspondence between pairs of rainfall processes observed at the same time by the radar and by each rain gauge at the rain gauge location is investigated through the analysis of trend with distance from Polar 55C of *G*/*R* ratio (defined as in Eq. (6.1)) between the rain gauge (*G*) and the corresponding radar (*R*) rainfall amounts (mm). Therefore, errors are found that depend on the location of the rain gauges (Sebastianelli et al., 2013). Gauge rain is compared with radar estimates mapped onto 1 x 1 km^2 grid. Each pixel of the grid includes a number of range-bins (radar polar samples) that depends on the distance from radar. To verify the effectiveness of the methodology, the behaviors of the FSE index, slope of the scatter plots' regression lines and *G*/*R* ratio trends against range relative to each processing level are compared. Those variables are calculated between pairs of rainfall time series collected by Polar 55C and each rain gauge (see Chapter 6).

6.2.1 – Processed data

This analysis takes into account 148 rainfall events which occurred during 2008 and 2009 years. Pairs of rainfall time series are observed by Polar 55C as well as by each rain gauge at the rain gauge location during each of these events.

Zero rainfall values can be found in the time series of both the radar and the rain gauges. Yoo and Ha (2007) and Ha and Yoo (2007) have showed that zero measurements cannot be used for characterizing a rainfall field from rain gauge measurements, because they decrease the spatial variability of the data by producing a high variability of the correlation between pairs of time series, with several abnormally high estimates. However, considering pairs of radar and gauge rainfall series, zero radar rainfall estimates occur especially at great ranges, when the radar returns from precipitation can be quite close to the minimum detectable signal due to range degradation or attenuation. On the other hand, if there are no rainy areas smaller than a radar

pixel, it is possible that a rain gauge included in that pixel does not detect rainfall, even though the relative radar rainfall value is greater than zero (Villarini et al., 2008a). Moreover, during the warm season, when convective events occur, rain gauges could not detect rainfall, depending on the not uniform density of the rain gauge network (Maheepala et al., 2001) and on the small extension of precipitation areas (Moisello, 1999). So, couples of homologous values with at least an intensity value different from zero (namely mixed couples), in corresponding radar and rain gauge time series, are useful for highlighting the differences between radar estimates and rain gauges measurements. For this reason, they have been also considered to characterize radar error against range unlike couples of homologous null values.

This analysis considers measurements collected at 1.5° elevation because this angle minimizes the influence of ground-clutter and the contrasting need to keep the radar beam close to the ground (Gorgucci et al., 1995; Russo et al., 2005; Lombardo et al., 2006a; Russo et al., 2006). All the case studies of the collected data sets contain a sweep at 1.5° elevation (plan position indicator) collected with a repetition time of five minutes. Radar rainfall estimates are compared with the rain measured by a set of 40 tipping bucket rain gauges located inside the radar scanning area and managed by Regione Lazio - Ufficio Idrografico e Mareografico. Rain gauges have time resolutions of 10 or 15 min and a rain resolution of 0.2 mm/h. Only the rain gauges located in sectors with good radar visibility are considered, to avoid cases of partial or total beam-blocking, which would invalidate locally the radar error trend with distance estimation. This is done by estimating the radar visibility using the digital elevation model (DEM) with a resolution of 800 m x 600 m, produced by the Servizio Geologico Nazionale.

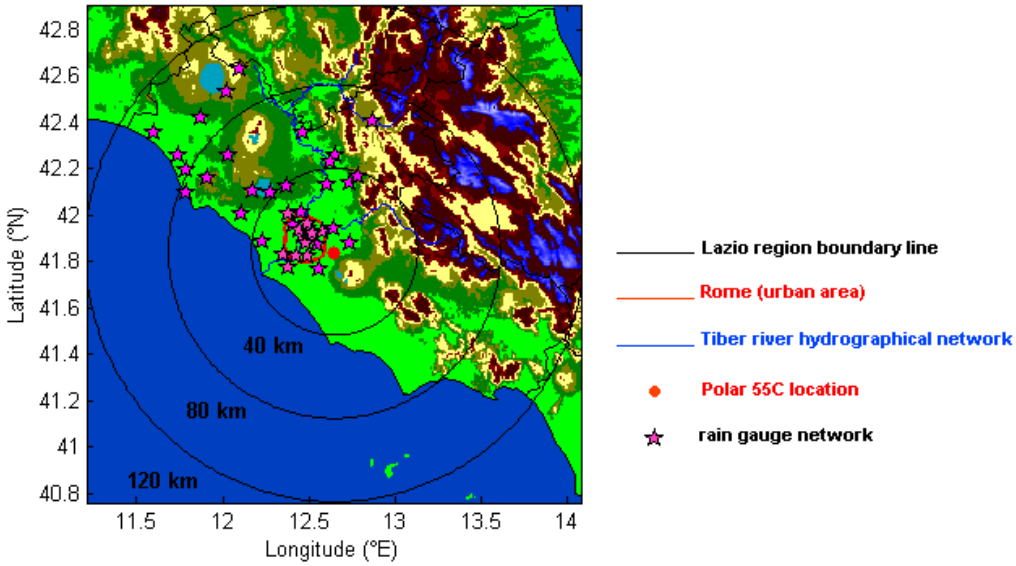

Figure 6.1 – Polar 55C location, rain gauge positions, Rome urban area and hydrographical network inside the test area.

Figure 6.1 shows the case-study region and the positions of the rain gauges of the network with respect to the Polar 55C location.

6.2.2 – Polar 55C calibration with rain gauges

The effects of radar miscalibration are corrected by adding a correction factor *C* to each recorded Z_h value. For this study, *C* is obtained from rain gauges calibration (Koistinen and Puhakka, 1986; Saltikoff et al., 2000). To calibrate the Polar 55C, a comparison is made between the radar rainfall amount and the rain gauges rainfall amount, by considering the latter as real, and the 2008 rain gauge data set is selected. However, only six rain gauges are chosen to calculate bias (namely Ostiense, Acqua Acetosa, Cassiodoro, Roma Sud, Roma Nord and Monte Mario), so that radar errors in rain gauges sites are likely due only to radar miscalibration, to avoid the influence of the other kinds of errors on bias calculation, as suggested by Sebastianelli et al. (2013). According to this purpose, only rain gauges located in areas with good visibility of the radar beam are chosen to avoid errors due to partial or total beam-blocking. Moreover, rain gauges are chosen in a range from 15 to 20 km to minimize range degradation effects (temporal and spatial sampling differences between the two devices), or errors due to attenuation, and to avoid antenna side lobe effects (urban clutter).

Referring to each rain gauge site, the *G*/*R* ratio is computed by utilizing only radar and rain gauge data that are collected in 2008. A multiplicative error *M* (dimensionless) is obtained by applying Eq. (4.7). Then, *M* is utilized to calculate radar bias *C* (in dB) by applying Eq. (4.8). Adding *C* to the reflectivity data (dBZ) is the same as multiplying radar rain (mm/h) by *M*. But, in the presence of range-dependent errors, also an *AF* depending on the distance must be added to reflectivity data, as explained in Sect. 6.3.3. Figure 6.2 shows the locations of the rain gauges employed for calibrating Polar 55C inside the radar scanning area.

So as it is calculated, *M* is an average bias within the range of distances in which the rain gauges are chosen. Differently from what is done by the other Authors (Sect. 6.1), we have estimated *M* only to correct systematic error due to radar miscalibration. Moreover, rain gauge data utilized for this issue are collected only at short ranges, as above mentioned. This is because rain fields are often composed of cores of convection embedded in larger stratiform precipitation regions, as described in the literature (Houze, 1997; Vignal et al., 2000; Zhang et al., 2008; Zhang and Qi, 2010). On the other hand, *Z*-*R* relation coefficients depend on the DSD and, therefore, they vary in time and space, as well as *Z*-*R* relation varies geographically depending on the type of precipitation (Koistinen and Puhakka, 1986; Saltikoff et al., 2000; Villarini and Krajewski,

2010). Thus, the error introduced by *Z-R* relationship is a random error which varies in space. Therefore, in this work, it has not been represented through an invariant with space multiplicative bias *M*, namely main field bias.

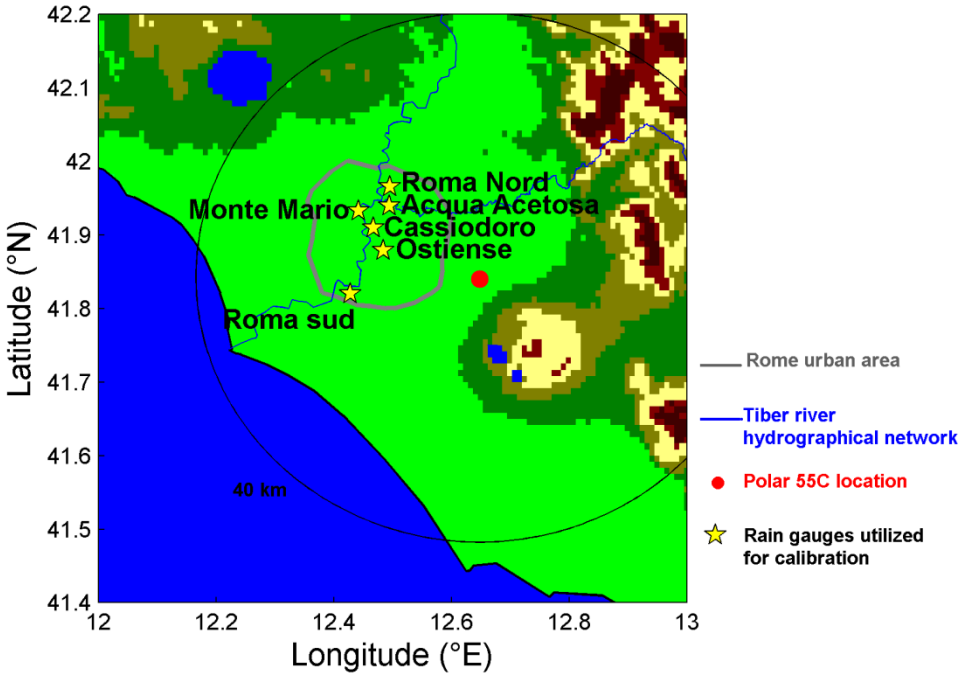

Figure 6.2 – Rain gauge utilized to perform Polar 55C calibration.

6.2.3 – Adjustment Factor estimate

Once the Polar 55C calibration has been performed, the overall radar range error is corrected by adding an *AF* to each recorded Z_h value. The *AF* is computed by utilizing rainfall events collected during 2008 by Polar 55C and 40 rain gauges placed in the radar scanning area (Sebastianelli et al. 2013). Data observed during 2008 are used to estimate the *G*/*R* ratios. The *G*/*R* ratio between the rainfall amount at each gauge site (*G*) and the respective radar rainfall amount (*R*) is computed. A vector of *G*/*R* ratios is created, whose components are defined as follows:

$$\left(G/R\right)_j = \sum_{i=1}^{E} G_i \Big/ \sum_{i=1}^{E} R_i \; ; j = 1,2,\ldots,N \qquad (6.1)$$

where G_i and R_i are the rain gauge and the radar rainfall amounts for the *i*-th event respectively, *E* is the number of rainfall events observed during 2008, the subscript *j* refers to a specific rain gauge, and *N* is the number of rain gauges (40). Since rain gauges are located at different distances from Polar 55C, the trend of logarithm of *G*/*R* as a function of the range is

subsequently evaluated and two different behaviors are found depending on the distance. The plot on the left in Fig 6.3 shows a comparison between the log*(G/R)* obtained before (row data) and after the radar calibration. Within the range of about 50 km the behavior of log*(G/R)* is influenced by the presence of the bright band, which causes a radar overestimation of rain, as better detailed in Chapter 7. Whereas, at the same time, the effect of attenuation and range degradation are reduced, the latter due to the fact that at an elevation of 1.5 degrees, the 1-degree beam of Polar 55C is sampling precipitation sufficiently close to the ground (in fact, at an elevation of 1.5°, at a distance of 50 km the height of the center of the radar beam is situated at an altitude of about 1.5 km above the ground). But, beyond this range, an about increasing linear trend of logarithm of the *G*/*R* ratios occurs (up to a value of 2 after radar calibration), and this means that radar error increases with range, indicating an increasing underestimate of rainfall by the radar as a function of the range. In consequence, radar estimates need to be corrected through a proper *AF*.

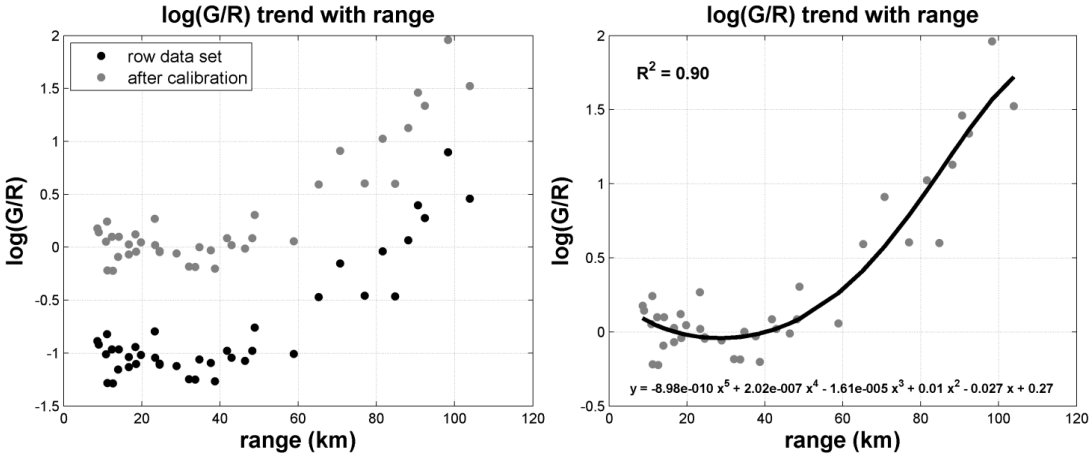

Figure 6.3 – Logarithm of the *G*/*R* ratio as a function of the range before any processing of data coupled with the same quantity trend obtained after radar calibration (left plot). Logarithm of the *G*/*R* ratios as a function of the range after radar calibration and best fitting line (right plot).

Therefore, after calculating the logarithm of *G*/*R* as a function of range, the best fitting line showed in the right plot of Fig. 6.3 is used to find the isotropic range dependent bias *AF* by applying the following empirical relation:

$$AF(r) = \frac{10}{b}\log_{10}\left(e^{X}\right) \qquad (6.2)$$

where r is the range, R^2 is the coefficient of determination, b has the same value as in Eq. (4.8), and X is the regression model of the logarithm of *G*/*R*, given by Eq. (6.3):

$$X = p_1 r^5 + p_2 r^4 + p_3 r^3 + p_4 r^2 + p_5 r + p_6 \qquad (6.3)$$

where p_1, p_2, p_3, p_4, p_5 and p_6 are the coefficients of the best fitting line whose values are showed in the figure above. The *AF* trend is showed in Fig. 6.4.

The *AF* is utilized to model the range-dependent error due to range degradation and signal attenuation, and it depends on the distance. Therefore, the *AF* can be utilized to correct the reflectivity maps and consequently the radar rainfall estimates derived from radar reflectivity.

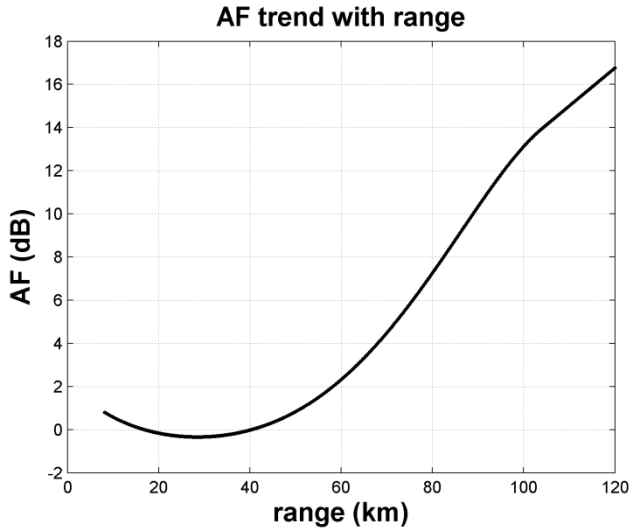

Figure 6.4 – *AF* trend with range.

6.3 – Adjustment procedure with correction of path attenuation

Unlike the previous case, here the adjustment procedure consists of four different processing levels, namely without any correction, after correction of signal attenuation, after radar calibration and after the adjustment procedure. After having identified and removed ground clutter and noise, radar data are corrected for signal attenuation. Then, radar calibration with rain gauges is performed. Finally, the gauge adjustment method is employed to find an *AF*, which takes into account the effects of range degradations (due to the radar beam geometry), the radar sampling precipitation within the melting layer, and the non-uniform VPR. As has already been said about the first method of analysis, for each processing level, corresponding rainfall processes observed by the two devices are compared through the analysis of the *G*/*R* ratio trend with range (Eq. (6.1)). In this way, the radar errors due to the different sources of uncertainties are found one by one depending on the slant range (Sebastianelli et al., 2013) and removed. Gauge rain is compared with radar estimates mapped onto a Cartesian grid consists of 1 x 1 km^2

pixels. Each pixel of the grid includes a number of range-bins (radar polar samples) that decreases as the distance from radar increases. At each rain gauge site, the *G*/*R* ratio is computed and plotted against range for each considered elevation angle. To verify the effectiveness of the methodology trends of *G*/*R* ratio relative to each processing level are compared. To perform this comparison, only rain gauges approximately aligned along a radius are chosen, in order to emphasize the effects of the signal attenuation, as better detailed in Chapter 7.

6.3.1 – Correction of the signal attenuation

The signal attenuation depends on both the path's length of the signal within the medium and the rain rate. Before the radar calibration, to correct the radar error due to the signal attenuation the differential phase shift (Φ_{DP}) is utilized, as it is a cumulative quantity with the distance. Moreover, since it is a measurement of a phase angle, it is immune from attenuation. The Φ_{DP} is generated by the overlapping of the transmitted wave and the forward scattered wave (see Sect. 4.2.8). The differential phase shift is utilized to estimate the cumulative attenuation along a path of any length. For each ray, the cumulative attenuation calculation is based on the variation of Φ_{DP} calculated between the first and the last range-bin corresponding to meteorological echoes (Testud et al., 2000; Wang and Chandrasekar, 2009). Since the relation *Z*-*R* is a power law, being equal the cumulative attenuation, the increase of the rain rate obtained with the correction depends on the initial reflectivity value to be corrected. As already mentioned in Sect. 5.3, radar rainfall values equal to zero refer to range-bins in which the reflectivity does not exceed the noise level. Since the noise is identified and removed before considering the attenuation (See Sect. 6.4), radar values equal to zero in range-bins affected by noise are not corrected by the signal attenuation effects.

6.3.2 – Processed data

This analysis takes into account 61 rainfall events which occurred during 2008. Pairs of rainfall time series are observed by Polar 55C as well as by each rain gauge at the rain gauge location during each of them. Figure 6.5 shows trends against the slant range of the various types of couples of homologous values in radar and rain gauges time series pairs. For each rain gauge location, each percentage refers to the total number of couples in radar and rain gauge time series pair. Figure 6.5 shows that couples with both homologous null values in radar and rain gauge time series pairs are always greater in number regardless of the distance depending on the characteristics of the rain fields. For this reason and as discussed in Sect. 6.2.1, couples of

homologous null values in corresponding radar and rain gauge time series are not considered. Due to the range degradation and the path attenuation couples with both homologous null values (blue) are more frequent at a great distance from radar rather than near the radar. For the same reasons, beyond a range of about 90 km from the radar the most part of couples with only one null value, namely mixed couples, are formed by a null radar value (red). This means that away from the radar location both the couples of homologous non-zero values (magenta) and mixed couples with null values of gauge (green) tend to decrease with increasing range (as showed by Fig. 6.5). For this reason and since null radar values are not corrected for path attenuation (see Sect. 6.3.1), this analysis does not even consider the mixed couples. Moreover, this analysis considers antenna elevation angles ranging from 1.5 to 4.5°, because most of the used scanning strategies of Polar 55C includes these angles. It must be remark that positive elevation angle allows satisfying the need to minimize the influence of ground-clutter and the contrasting need to keep the radar beam close to the ground (Gorgucci et al., 1995; Russo et al., 2005; Lombardo et al., 2006; Russo et al., 2006). The rainfall maps which refer to the same elevation angle are acquired with a temporal resolution of 5 minutes.

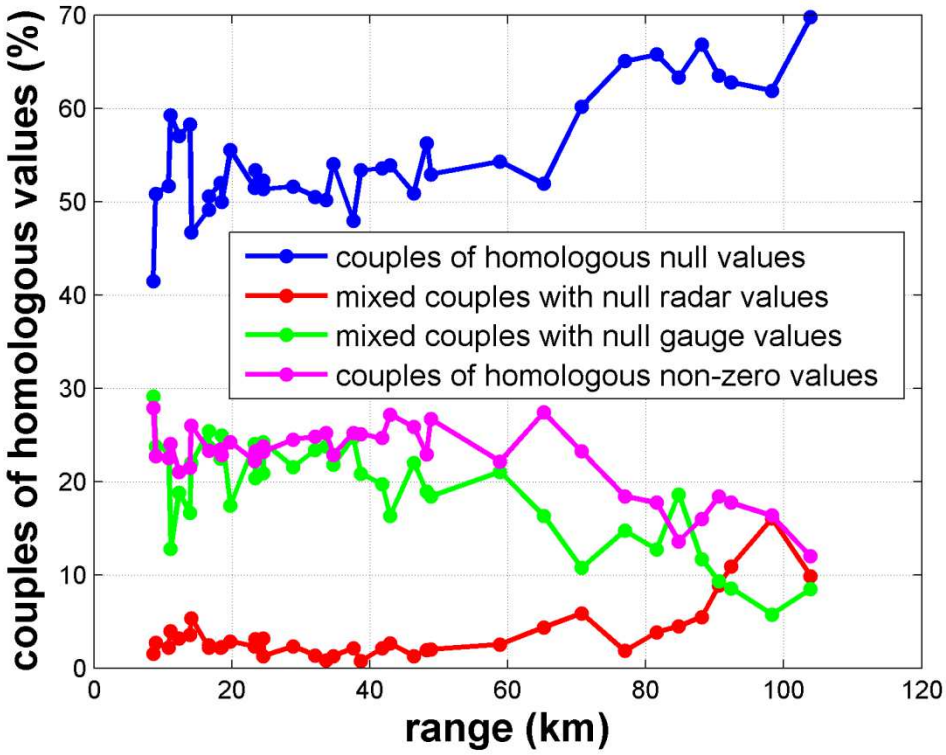

Figure 6.5 – Trends with range of couples of homologues components in radar and rain gauge time series pairs. Blue dots refer to couples of homologous null values. Magenta dots refer to couples of homologous non-zero values. Red (green) dots refer to mixed couples with radar (rain gauge) values equal to zero.

6.3.3 – Polar 55C calibration with rain gauges

After having corrected the signal attenuation, the radar calibration is carried out as in the previous analysis, and also the rain gauges used are the same. But this time all the values equal to zero in corresponding radar and rain gauge time series are not considered as already said.

6.3.4 – Adjustment Factor estimate

Once the Polar 55C calibration has been performed, the overall range error is corrected by adding an *AF* depending on the elevation angle to each recorded Z_h value. The *AF*s are computed by utilizing rainfall events collected during 2008 by Polar 55C and 40 rain gauges placed in the radar scanning area (Sebastianelli et al. 2013). Data observed during 2008 are used to estimate the *G*/*R* ratios. The *G*/*R* ratio between the rainfall amount at each gauge site (*G*) and the respective radar rainfall amount (*R*) is computed, and a vector of *G*/*R* ratios is created as is done in the previously analysis (Eq. (6.1)).

Then, the trend of logarithm of *G*/*R* as a function of the range is evaluated for each elevation angle and two different behaviors are found depending both on the distance and on the elevation angle. The curves showed in Fig 6.6 refer to radar data sets obtained after the attenuation correction and radar calibration, and for each antenna angle. Within a certain range (depending on the elevation angle), the behavior of log(*G*/*R*) is influenced by the presence of the bright band, which causes a radar overestimation of rain, as better detailed in Chapter 7. But, beyond these ranges, increasing linear trends of logarithm of the *G*/*R* ratios occur (up to a value ranging from about 0.5 to about 4.5 depending on the elevation angle) and this means that radar error increases with range, indicating an increasing radar underestimate of rainfall as a function of the range. In consequence, radar estimates need to be corrected through an *AF*.

Therefore, after calculating the logarithm of *G*/*R* as a function of range, the best fitting lines showed in Fig. 6.6 are used to find the *AF*s by applying the same empirical relations, as in Eq. (6.2).

Curves in Fig. 6.7 represent *AF* trends against range obtained at different elevation angles after both attenuation correction and Polar 55C calibration. In agreement with the behavior of the log(*G*/*R*), apart from the elevation angle, the *AF* shows two behaviors depending on the distance, as better detailed in Chapter 7. In fact, due to the bright band which occurs during stratiform precipitations, the *AF* assumes the lowest values belonging to the first concave line of each curves. Instead, the second increasing lines are due to the RDE that increases as the distance increases. Moreover, the slope of the second part of the curves increases as the antenna angle

increases, because of the greater the elevation angle, the greater the effect of the range degradation and non-uniform VPR.

It must to be noted that the greater the elevation angle: (1) the lower the distance at which the radar beam intercept the melting layer; (2) the shorter the path needed to the radar beam to pass through the melting layer, and (3) the bigger the part of the radar sampling volume within the melting layer. As a consequence, as the elevation angle increases the length of the concave part become shorter and the minimum value moves to the origin of the coordinate system, which corresponds to the radar site (see also Chapter 6 for more details).

The *AF*s in Fig. 6.7 are utilized to model the range-dependent error due to range degradation and its depend both on the distance and on the elevation angle.

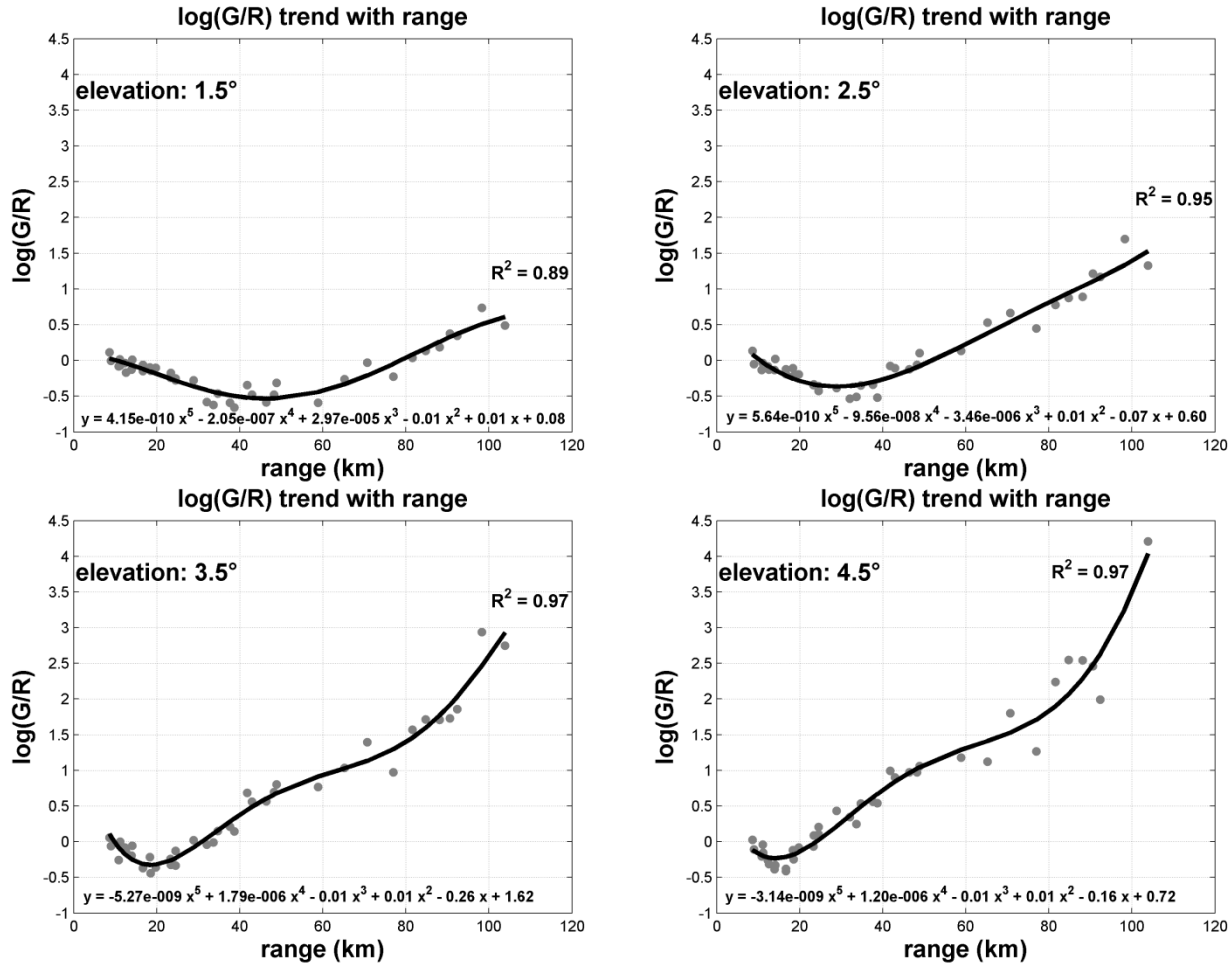

Figure 6.6 – Logarithm of the *G*/*R* ratios as a function of the range and best fitting lines. Each plot refers to a specific elevation angle.

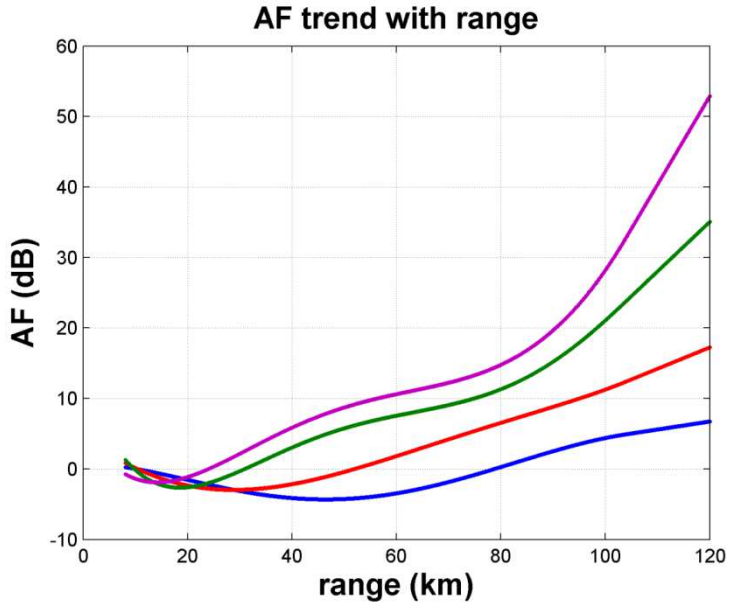

Figure 6.7 – Trends of *AF* as a function of the slant range for each elevation angle.

6.3.5 – Flowsheet

Each processing of data has been carried out utilizing algorithms written in Matlab language. The followed methodology is organized according to the scheme showed in Fig. 6.8. Every 5 minutes the Polar 55C weather radar repeats a sweep with the same elevation angle. Each scan lasts about 1 minute. During a scan, the radar acquires a matrix of 240 x 240 values of rain rate (mm h^{-1}). Each value is relative to a pixel of the radar Cartesian grid. Subsequently, values are converted to mm. The matrices acquired during the same event (or measurement session) which correspond to the same elevation angle form a three-dimensional matrix called rain event. Knowing the positions of each rain gauge within the grid, it is possible to extract from each rain event the rainfall time series observed by the radar in the pixel where a considered sensor is located. Then, the cumulative rain calculated from the values of the series is compared with the cumulative precipitation of the corresponding rain gauge series.

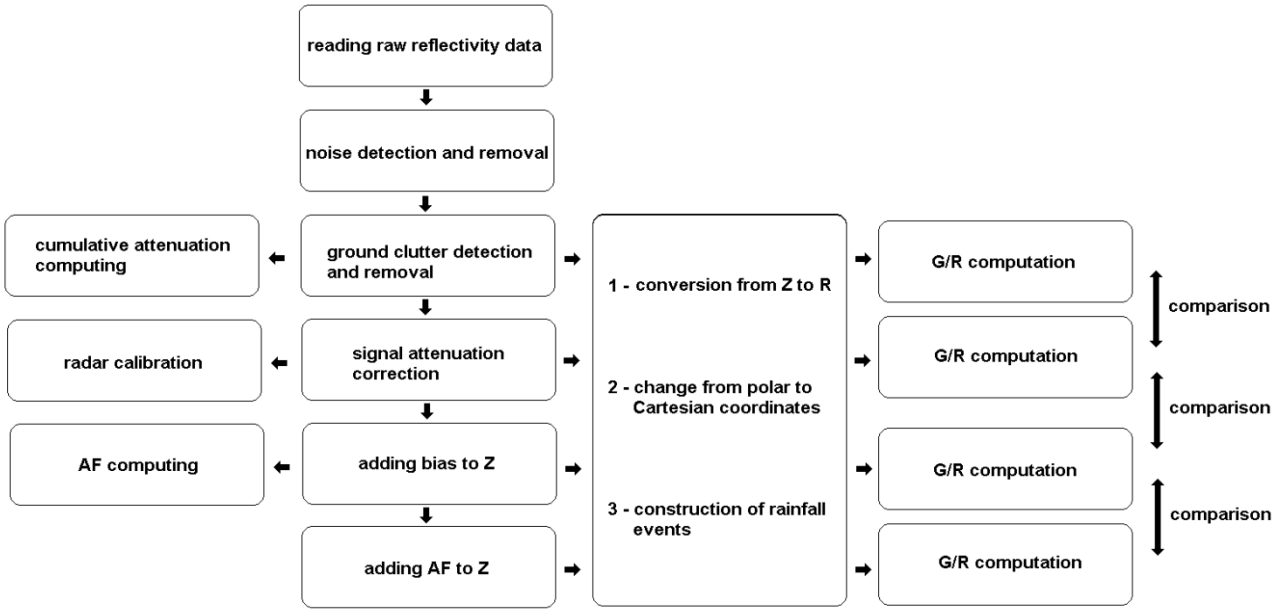

Figure 6.8 – Adjustment procedure scheme.

Chapter 7

Data processing

7.1 – Verification of gauge adjustment of radar data technique

In this section, the effectiveness of the gauge adjustment of radar data technique introduced in Sect. 6.2 is verified. The correspondence of rainfall processes observed by radar and by each rain gauge at the rain gauge site is investigated through the analysis of trend with range from Polar 55C of: (1) FSE index; (2) slope of the scatter plots' regression lines and (3) *G*/*R* ratio between rain gauge and radar rainfall amounts, defined as in Eq. (6.1). Each index value can be defined by choosing a pair of rainfall processes observed at the same time by the radar and by a rain gauge at the rain gauge location. In particular, FSE index values are calculated by computing the differences between homologous components of pairs of rainfall time series. The two rainfall time series are compared also in a scatter plot. The slope of the regression line is then calculated for each scatter plot. Since the single scatter plot concerns comparison between data from radar and only one rain gauge, and as each rain gauge is located at a different distance from radar, it has been possible to relate the regression lines' slope to the range. At each rain gauge site, the *G*/*R* ratio between a rain gauge rainfall amount *G* and the corresponding radar rainfall amount *R* is computed and plotted against the distance from radar of each rain gauge. The FSE is here used as a measure of the differences between the values predicted by a model (radar data) and the values actually observed from a rain gauge, or to quantify the radar error. It is defined as:

$$FSE = \frac{\sqrt{\sum_{i=1}^{N}\left(x_r - x_g\right)^2 / N}}{\sum_{i=1}^{N} x_g / N} \qquad (7.1)$$

where x_r and x_g are the radar and the rain gauge data respectively, while N is the number of the observed values.

To verify the effectiveness of the methodology, the range dependence of rainfall radar field is characterized by analysis of behavior (in relation to the slant range) of the above mentioned variables, which are calculated both for the 2008 data sets and for the 2009 data sets. Trends against range, obtained both before and after the adjustment procedure, are compared to show the improvement of radar estimates. Each comparison is performed by considering a fixed accumulation time, ranging from 30 to 90 min. Moreover, we analyse the scatter plots for two

ranges of distances where different radar errors prevail, namely 0-40 km and 40-120 km. Radar data sets are used with different processing levels, namely without any correction, after radar calibration and after the adjustment procedure.

Scatter plots in Figs. 7.1 and 7.2 concern rain gauges located within the range of distances from 25 to 40 km away from Polar 55C, where the radar beam intercepts the melting layer most frequently during the cold season at the elevation angle of 1.5°. Rainfall time series of Fig. 7.1 and Fig. 7.2 have been observed during 2008 and during 2009, respectively. These figures concern accumulation times of both 30 min (upper panels) and 90 min (lower panels). The plots on the left represent the initial radar data set without any correction. The plots in the middle and the plots on the right are obtained after radar calibration and after adding the *AF* to the reflectivity, respectively. Since the effects of sampling uncertainties and attenuation are negligible close to the radar, it must to be noted that prior to calibration Polar 55C overestimates rainfall with respect to rain gauges, due to radar miscalibration and the presence of melting layer. Then, calibration strongly reduces radar overestimation. In fact, by comparing left panels and graphs in the middle both in Fig. 7.1 and in Fig. 7.2, the regression line's slope strongly increases after calibration. After applying *AF* to reflectivity maps, rainfall radar estimates slightly improve again, because also the effect of melting layer is corrected. Therefore, a further increase of the slope occurs when the *AF* is added to reflectivity.

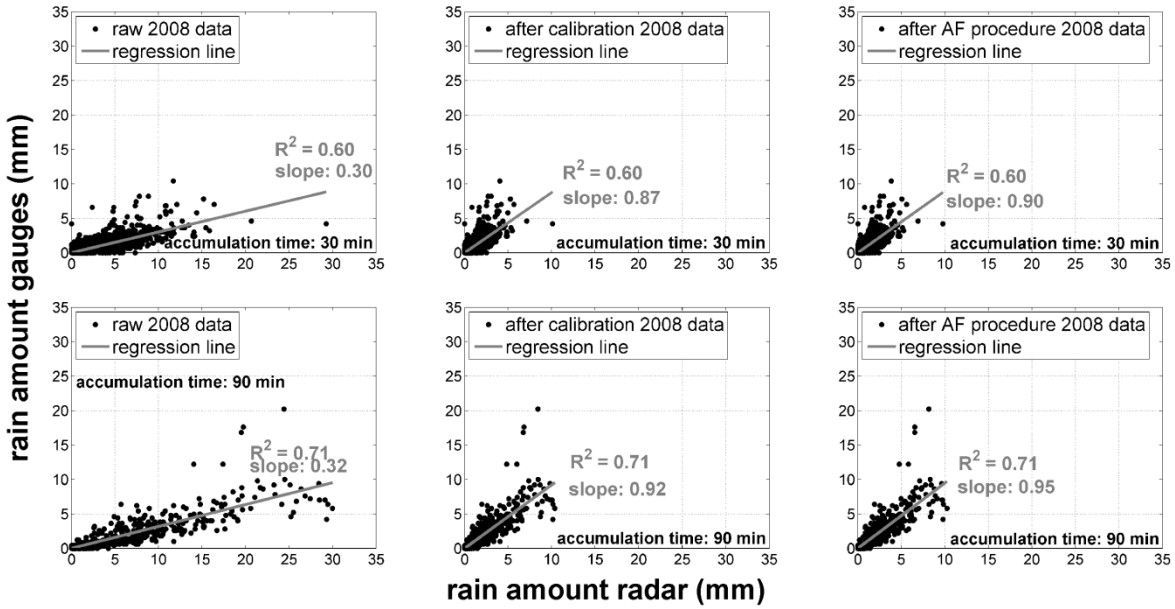

Figure 7.1 – Scatter plots of rainfall time series' pairs, obtained during 2008 by Polar 55C and by each rain gauge located from 25 to 40 km away from Polar 55C. These refer to a time aggregation of 30 and 90 min (upper panels and lower panels, respectively) for the initial data sets (left panels), after calibration (middle panels) and after the adjustment procedure (right panels).

In Fig. 7.1, when accumulation time ranges from 30 min to 90 min, the slope increases from 0.30 to 0.90 (upper panels), and from 0.32 to 0.95 (lower panels). At the same time, in Fig. 7.2 the regression line's slope changes from 0.28 to 0.83 (upper panels), and from 0.30 to 0.91 (lower panels).

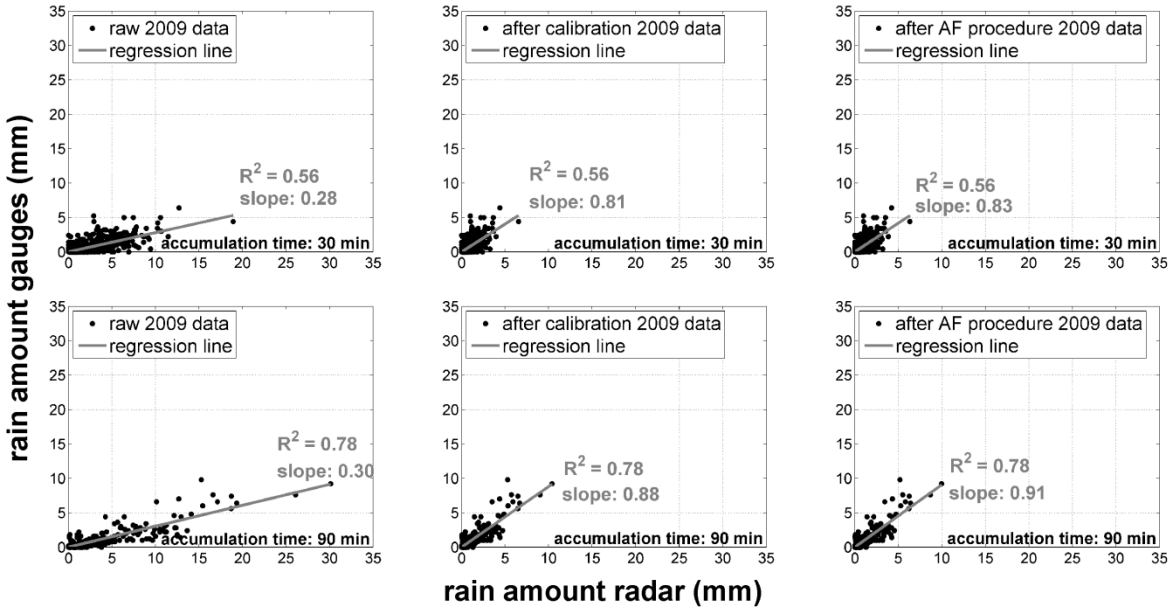

Figure 7.2 – Scatter plots of rainfall time series' pairs, obtained during 2009 by Polar 55C and by each rain gauge located from 25 to 40 km away from Polar 55C. These refer to a time aggregation of 30 and 90 min (upper panels and lower panels, respectively) for the initial data sets (left panels), after calibration (middle panels) and after the adjustment procedure (right panels).

At longer distances and prior to calibration, radar miscalibration effects are compensated for by the effects of sampling errors and attenuation (which would lead to rainfall underestimation). Moreover, effects of melting layer do not exist. Therefore, before calibration, radar overestimates rain less than in the previous case, when it samples beyond a distance of 40 km. This may be observed by comparing left plots in Figs. 7.1 and 7.3, or left plots in Figs. 7.2 and 7.4. Rainfall time series in Figs. 7.3 and 7.4 refer to measurements collected beyond a distance of 40 km far from Polar 55C in 2008 and in 2009, respectively. In particular, left, middle and right panels refer to different processing levels, namely raw reflectivity, calibrated reflectivity, and after applying the adjustment procedure, respectively. Upper and lower panels refer to 30 and 90 min accumulation times, respectively. Once calibration is performed, at farther distances the effects of range errors are no more compensated for, and radar underestimates rainfall. In particular, by comparing left and middle panels in Fig. 7.3, it results that the slope of the regression lines increases by about 1 or 1.1, depending on the accumulation time. Instead, for

2009 data, it increases by about 1 or 1.2, referring to 30 min and 90 min accumulation time, respectively (compare corresponding plots in Fig. 9).

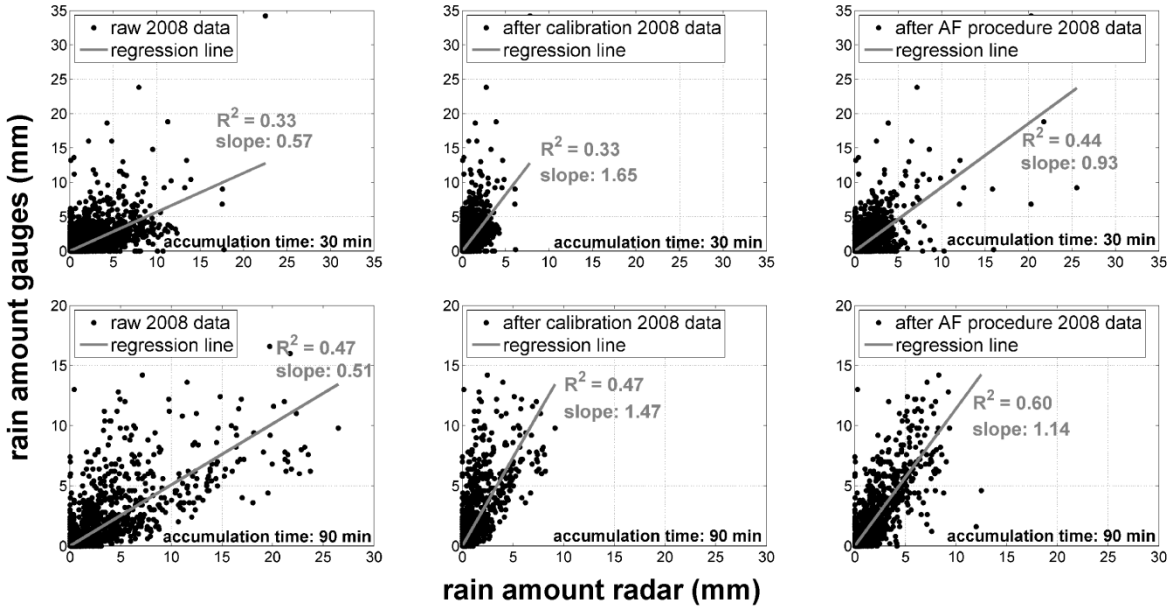

Figure 7.3 – Scatter plots of rainfall time series' pairs, obtained during 2008 by Polar 55C and by each rain gauge located close to the border of the scanning circle. These refer to a time aggregation of 30 and 90 min (upper panels and lower panels, respectively) for the initial data sets (left panels), after calibration (middle panels) and after the adjustment procedure (right panels).

Then, by comparing the slopes of the regression lines in middle and right panels in Figs. 7.3 and 7.4, it can be seen that after adding the *AF* to reflectivity, rainfall radar estimates always improve due to the correction of the effects of range errors. Therefore, in Fig. 7.3 slope values pass from 1.65 to 0.93, and from 1.47 to 1.14 for 30 min and 90 min accumulation times, respectively. Correspondingly, in Fig. 7.4, they pass from 1.40 to 1.07, and from 1.83 to 1.46.

In addition to what has been already said about Figs. 7.3 and 7.4, it can be noted that coefficient of determination R^2 increases when the *AF* is added to reflectivity. This is due to the fact that *AF* increases as the distance from radar increases (see Fig. 6.4). So, rain values estimated by the radar close to the edge of the scanning circle (where the underestimation is greatest) increase more than other values. Thus, at the end of the adjustment procedure, dots are less scattered and this means that correlation increases, and, therefore, R^2 increases (Kottegoda and Rosso, 2008).

Vice versa, close to Polar 55C, as showed by Figs. 7.1 and 7.2, R^2 does not increases when the *AF* is added to reflectivity, because the *AF* is not so variable within the range of distances considered, as showed in Fig. 6.4. Moreover, the correlation between radar and rain gauges rainfall time series always increases as the accumulation time increases.

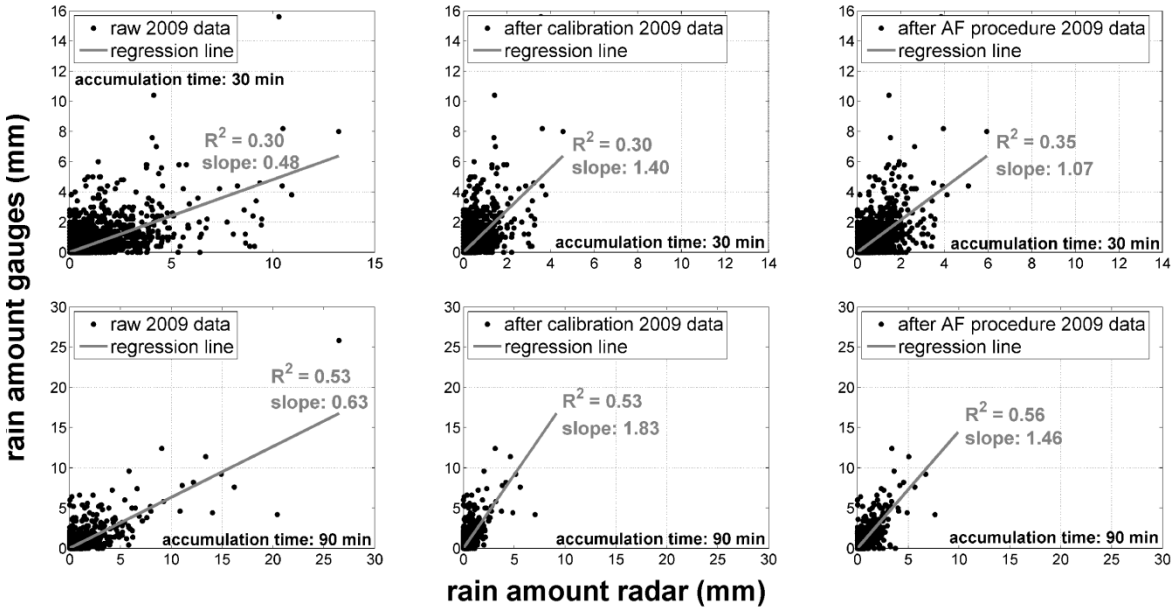

Figure 7.4 – Scatter plots of rainfall time series' pairs, obtained during 2009 by Polar 55C and by each rain gauge located close to the border of the scanning circle. These refer to a time aggregation of 30 and 90 min (upper panels and lower panels, respectively) for the initial data sets (left panels), after calibration (middle panels) and after the adjustment procedure (right panels).

Figure 7.5 shows trends of synthetic index FSE, slope of the scatter plots regression lines and *G*/*R* ratio as a function of the slant range, estimated for radar and rain gauges data sets collected during 2008 (upper panels) and 2009 (lower panels). Each plot shows three curves, each of them relative to a different radar data set, obtained before any correction, after radar calibration and after the adjustment procedure (blue, green and red dots respectively). Notably, the slope of the scatter plots' regression lines always has the same trend with range as with the *G*/*R* ratio.

As mentioned above, before calibration Polar 55C overestimates rainfall (especially close to the radar) due to radar miscalibration, to the sampling within the melting layer, and to the negligible effects of range errors (beam broadening and path attenuation). As a consequence, FSE index and *G*/*R* ratio (or slope of the scatter plots' regression lines) have the greatest and the lowest values respectively (blue dots) at closer ranges. But, sampling errors and attenuation effects become more and more important as the distance increases until the radar miscalibration effect is balanced. Therefore, close to the edge of the scanned area, Polar 55C can underestimate rainfall. In fact, FSE reaches the maximum value for distances where more frequently the radar beam has intercepted the melting layer during the year. Similarly, the corresponding *G*/*R* and slope values reach a minimum value for the same distances. Then, FSE begins to decrease up to a value of 2 or less, whereas, *G*/*R* and slope begin to increase up to a value of 1 or more. For distances that range from about 70 to 90 km, slope and *G*/*R* ratio are close to 1 because radar miscalibration

effect is balanced by the effects of path attenuation and radar sampling geometry. Beyond these distances slope and *G*/*R* ratio are slightly greater than 1 because range errors increase with distance exceeding bias. For this reason, beyond 70 km from radar, FSE trend is not so clear (as showed by blue dots in left panels in Fig. 7.5).

Moreover, through calibration FSE decreases where bias is prevalent with respect to range errors, while it increases where range errors exceed bias (comparison between blue and green dots in Fig. 7.5). At a fixed distance, *G*/*R* ratio and slope always increase after performing calibration. As a result, they are about equal to 1 close to the radar (in correspondence of the Rome urban area), where the effects of sampling errors and attenuation are negligible. However, they assume values lower than 1 within the area more subject to the bright band occurrence. But, beyond the range which corresponds to the presence of the melting layer, their values begin to increase up to a value of 5 or more, due to range errors. At the end of the adjustment procedure, they are close to 1 all along the path, due to the improvement of radar estimates. In fact, when the *AF* is added to reflectivity, *G*/*R* and slope decrease far from radar due to the correction of range errors, and they tend to increase, albeit slightly, where the bright band is corrected. Correspondingly, FSE index has the lowest values, as showed by red dots in Fig. 7.5, which demonstrate the increased agreement between radar and rain gauge rainfall fields. In particular, close to the radar, FSE values become close to 2 or less after the adjustment procedure, whereas they can be up to 5 or more before calibration where the radar beam most probably intercepts the melting layer. At far distances, FSE values range from 1 to 2, after calibration, but they decrease after the adjustment procedure. Curves in Fig. 7.5 are obtained by considering an accumulation time of 30 min. The improvement of radar estimates is confirmed also by the slopes of the best fitting lines (referring to red dots) represented in black, which are very close to 1.

As above mentioned, rainfall radar estimates slightly improve when the effect of the melting layer is corrected by adding the *AF* to the reflectivity. To highlight this improvement Fig. 7.6 shows the differences between the values that the variables represented in Fig. 7.5 take before and after *AF* is added to the reflectivity, within the range of distances where the bright band signature is recognizable. The figure concerns 2009 year data. The subscripts *C* and *AF* refer to two different processing levels, namely after calibration and at the end of the adjustment procedure. It can be seen that, after the addition of the *AF* to reflectivity, *G*/*R* ratio and scatter plots' regression lines slope increase, whereas FSE index decreases because of the correction of radar overestimation due to the sampling within the melting layer.

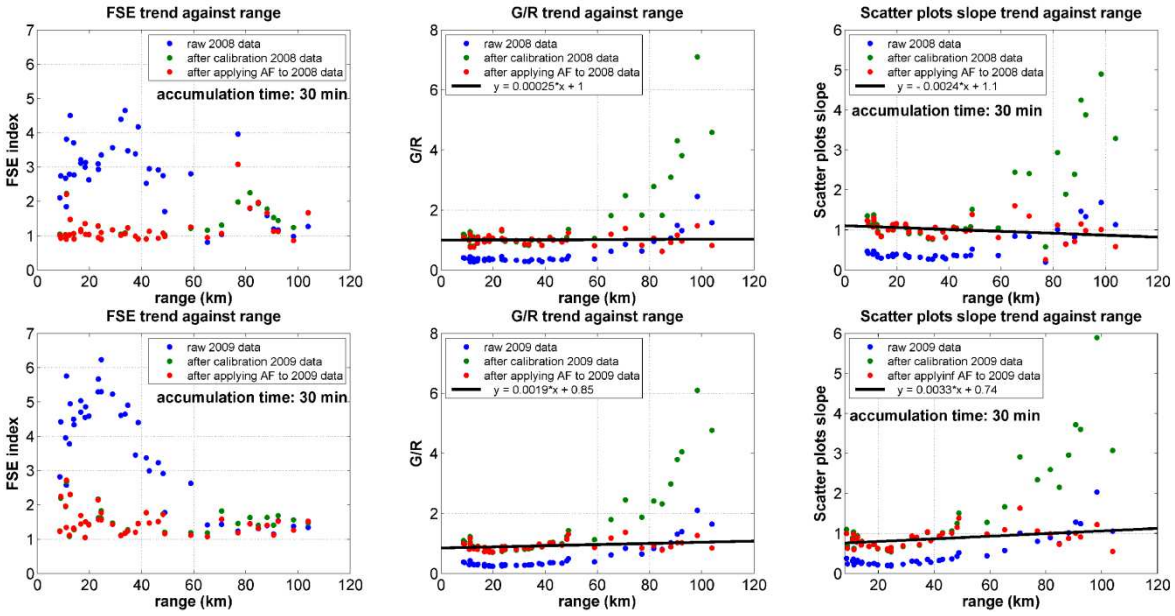

Figure 7.5 – FSE index, *G*/*R* ratio and slope of the scatter plots' regression lines trends with distance (left, middle and right panels respectively) of rainfall time series pairs obtained during 2008 (upper panels) and 2009 (lower panels) by Polar 55C and each rain gauge, for the initial data sets (dots in blue), after calibration (dots in green) and after adding *AF* (dots in red). Black lines are best fitting lines referring to red dots.

Figure 7.7 shows the FSE (top) and the slope of the scatter plots' regression lines (bottom) trends against range of rainfall time series pairs obtained during 2009 by Polar 55C and each rain gauge, for the initial data set, after calibration and after the adjustment procedure (left, middle and right panels respectively). Dots colors refer to different accumulation times (30, 60 and 90 min). Figure 7.7 shows that both the slope of the scatter plots' regression lines and the FSE index maintain the same trend against range for each accumulation time. So, the improvement of radar estimates is obtained for all the considered accumulation times (as already illustrated in Figs. 7.1, 7.2, 7.3, and 7.4).

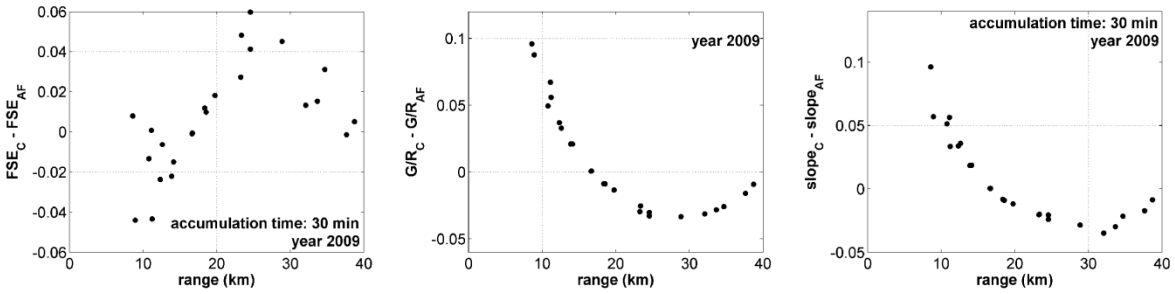

Figure 7.6 – Differences between FSE, *G*/*R*, and slope values before and after the addition of the *AF* to reflectivity, within the range of distances 0-40 km. Figure refers to 2009 year. Subscripts *C* and *AF* refer to two different processing levels, namely after calibration and at the end of the adjustment procedure.

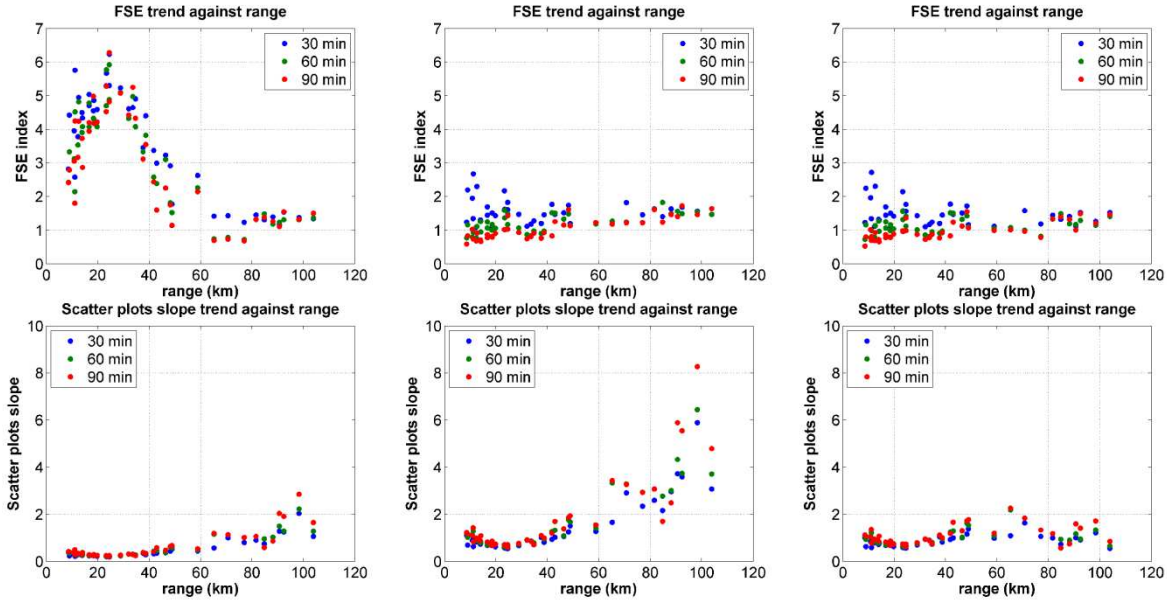

Figure 7.7 – FSE trend and slope of the scatter plots' regression lines trend with range (plots on the top and on the bottom respectively) of rainfall time series pairs obtained during 2009 by Polar 55C and each rain gauge for the initial data sets, after calibration, and after the adjustment procedure (left panels, middle panels and right panels respectively). Dots in blue, in green and in red correspond to an accumulation time of 30, 60 and 90 min respectively.

7.2 – Verification of adjustment procedure including path attenuation correction method

In order to verify the effectiveness of the methodology a subset of 17 rain gauges appears as aligned along a given direction from radar along a range of almost 120 km free from beam blocking effects is used. This direction, which is almost parallel to the Tyrrhenian coast line, is also that along which intense convective cells tend to organize themselves as a squall line. A set of five rainfall events observed during 2008 is used to this purpose. Pairs of rainfall time series have been observed by Polar 55C and by each rain gauge at the rain gauge location during each of them. Moreover, events are chosen so that a squall line almost covers fully the path from radar to rain gauges, or this path is contained in a very intense rainy area during the whole of the considered event. In this way, an optimal rain gauge network configuration for highlighting the effects of the signal attenuation is carried out. Figure 7.8 shows the case-study region and the rain gauges positions respect to Polar 55C location.

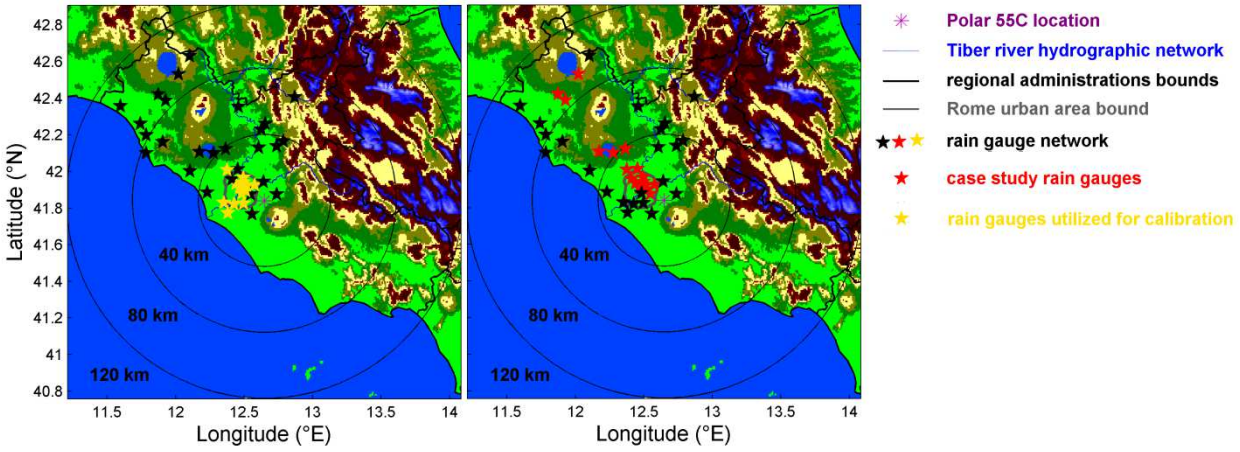

Figure 7.8 – Rain gauge network inside Polar 55C scanning area. In yellow (left panel) and red (right panel) are the rain gauges selected for calibration and to verify the correction procedure, respectively.

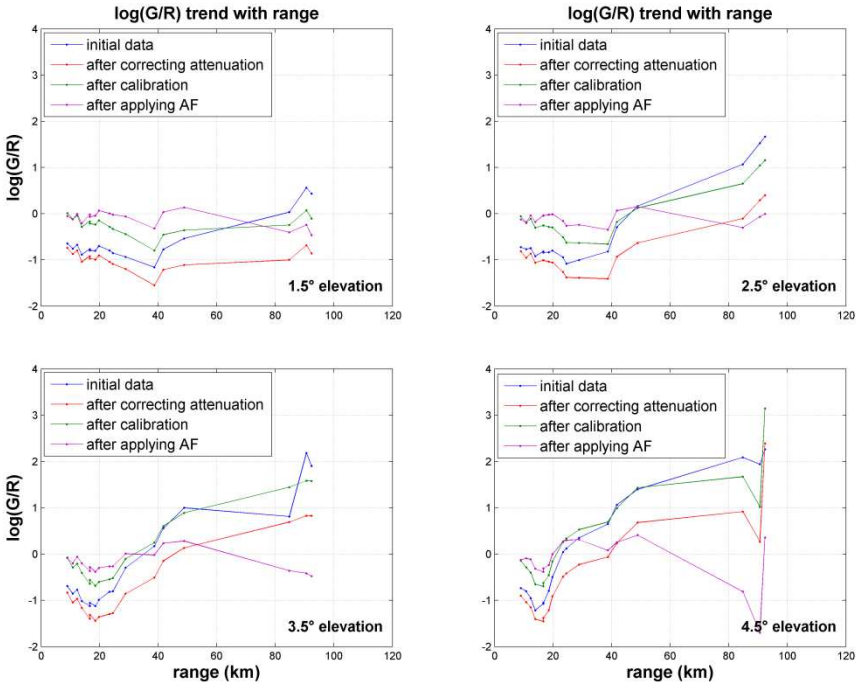

Figure 7.9 - *G*/*R* logarithm trends with range from Polar 55C evaluated for the initial radar data set, after signal attenuation correction, after radar calibration and after the adjustment procedure (blue, red, green and violet lines respectively); each plot is referred to a different elevation angle.

The correspondence between pairs of rainfall processes observed, at the same time, by the radar and by each rain gauge at the rain gauge site is investigated through the *G*/*R* ratio trend as a function of slant range. As already said in Chapter 5, trends obtained before and after each processing of radar data are compared to show the improvement of radar estimates, and only pairs of positive radar and rain gauge precipitation data are considered. This comparison is made

referring to the initial data set (without any correction) and repeated for different processing stages (Fig. 7.9).

Before any correction, due to the negligible effects of range errors and to the presence of the melting layer, Polar 55C overestimates rainfall close to its location, where log(*G*/*R*) assumes the lowest values. But, when the radar beam passes beyond the melting layer, sampling errors and attenuation effects become more important as the range increases. Therefore, beyond a certain range, depending on the elevation angle, log(*G*/*R*) values begin to increase up to a value which depends on the elevation angle. Fixed the distance, the greater the elevation angle, the greater the maximum value of log(*G*/*R*). At first, the effect of RDE is balanced by radar miscalibration effect. Therefore, Polar 55C underestimates rainfall especially close to the edge of the scanned area. After the attenuation correction, the improvement of *G*/*R* (red curves in Fig. 7.9) is evident only at far ranges. Whereas, close to the radar, due to the negligible effects of the range degradation, the radar overestimate strongly rain because of both sampling through the melting layer and radar miscalibration. A further improvement of radar estimates is obtained by calibrating radar (see Sect. 6.2.2). Finally, after the adjustment procedure log(*G*/*R*) values are close to 0 all along the path, verifying the effectiveness of the followed methodology. Also the concavity of the initial portion of the curve is reduced. However, at great distance from radar, it is not verified for the highest elevation angle, for which the number of couples of homologous non-zero components, in corresponding pairs of rainfall processes, is so small that the curves are not meaningful.

7.3 – Variability of the *AF*

The range dependent error model called *AF* introduced in Chapter 6 is used as a range error pattern allowing to correct the error affecting long-term QPE. It is achieved by post processing data. The global correction based on a year of measures has been applied to individual radar observations. Then, the testing of the methodology is performed by comparing the pairs of radar and rain gauge yearly series of rainfall in correspondence of each rain gauge location, as is done in Sects. 7.1 or 7.2.

To be applied at shorter time scales, *AF* variability, depending on the event type, is investigated. As is done in Chapter 6, range error is characterized by examining trend of ratio *G*/*R* as a function of the range, obtained for each rain gauge location, using calibrated radar data collected during a single event. Initially, rainfall events collected by Polar 55C during the 2008 – 2009 period, are split into convective and stratiform cases. The distinction is based on a Radar

Convective Parameter (*RCP*), which takes into account the VPR distribution (see Sect. 4.2.3) that characterizes each type of event (Steiner et al., 1995; Bechini et al., 2012). In each pixel in which pertains one of the rain gauge of the network, the VPR is estimated through the use of a cycle of antenna elevation angles ranging from 1.5 and 5.5°. In this way, 40 VPR are acquired (i.e. as many as the rain gauges available) at time intervals of about 5 min, concerning a sampling volume between two isotherms, corresponding to 0 and -15°C. For each observed event a *RCP* value is estimated, based on the reflectivity profiles obtained for each sample volume, and defined as follows (Bechini et al., 2012):

$$RCP = \mathrm{RMSE}\big(\mathrm{E}(Z) - \mathrm{median}(Z)\big) \tag{7.2}$$

where E(*Z*) and median(*Z*) are respectively the mean and the median of the reflectivity values collected in the sampling volume during a single sweep, and the RMSE is the root mean square error, defined as follows:

$$RMSE = \sqrt{\textstyle\sum_{i=1}^{N}\left(x_r - x_g\right)^2 \big/ N} \tag{7.3}$$

For each sweep, the difference is computed between the mean and the median of the reflectivity values collected in the sampling volume. Then, *RCP* is calculated as the RMSE of the differences calculated at each sweep. These differences (and so *RCP*) are smaller for stratiform cases than for convective ones. Therefore, events are divided into two classes (convective and stratiform) identified by the median of the parameter values set. In particular, an event is considered as stratiform if its *RCP* is less than the 50^{th} percentile. Vice versa it is considered as convective. All events are chosen in such a way that each rain gauge available is able to record rainfall, to avoid that lack of data does not allow plotting the *AF*'s curves with continuity. As a consequence, despite several convective events are recognized (following the method above mentioned) during the summer season, we did not consider them because they are formed by sparse rain cells and the sampling by gauges is not sufficient. However, the methodology above explained allows to classify as convective others events occurring during cold season. Investigating these events, we found that they are frequently formed by young cores of convective precipitation embedded into very wide stratiform rain areas, as it is largely confirmed in the literature (Yuter and Houze, 1994; Houze, 1997; Vignal et al., 2000; Zhang et al., 2008; Zhang and Qi, 2010). Therefore, while a stratiform rain field is almost homogeneous, a convective one is very variable in space. This explains the fact that the differences in Eq. (7.2), and so the *RCP*, are greater in case of convective events than for stratiform ones. Moreover, during each event at least a radiosonde that describes the vertical profile of the temperature is available.

Figures 7.11-7.19 describe some case studies concerning events classified as stratiform or convective by the methodology illustrated above. Solid and dashed lines showed in Figs. 7.11 and 7.15 are carried out after calibration, for each elevation angle, from logarithm of G/R ratio trend with range, by using a polynomial fit of the fifth order and a method of moving averages with a window of 15 km, respectively. Subsequently, values assumed by each curve are converted to dB. Moreover, curves have been drawn up to the limit of the rain field detectable by the radar, in order to avoid that the interpolation process could generate a non meaningful estimation of the corrective term.

Figure 7.14 shows reflectivity measurements collected at vertical incidence by Polar 55C during a stratiform event, whereas, Figs. 7.17 and 7.19 show VPR collected by Polar 55C during two convective events. In the convective cases VPR refers to the stratiform part of precipitation, as we are interested in melting layer effects (see Sect. 7.3.2), namely bright band. In fact, inside convective cells the bright band signature is not defined because the intense updraft stops the formation of melting layer (Steiner et al., 1995; Bordoy et al., 2010). All figures show that the bright band peak is below the freezing level, which is showed taking into account the 162 m altitude of the radar antenna. The 0° isotherm heights are obtained by interpolating two consecutive temperature profiles carried out by the Pratica di Mare sounding station, located 27 km south of the radar site. Moreover, bright band thickness is a few hundred meters, as is largely explained in the literature (Mittermaier and Illinghworth, 2003; Baldini and Gorgucci, 2006; Zhang et al., 2008; Zhang and Qi, 2010; Bordoy et al., 2010; Krajewski et al., 2011). Above the freezing level, the reflectivity decreases with height due to the sampling of ice particles and beam overshooting (Seo et al., 2000). Below the bright band, reflectivity decreases until the DSD reaches a balance due to the ice melting and the hydrometeors' volume decreases as the altitude decreases. Furthermore, vertical observations are considered as valid only from 800 meters, due to the transient of polarization switch (Baldini and Gorgucci, 2006). For these reasons, following Zhang et al. (2008) and Krajewski et al. (2011) the VPR is considered to be independent from the altitude below the bright band where the DSD has reached balance. The reflectivity peak's altitude corresponds to the maximum in the VPR, while the top and the bottom bright band's borders are individuated by the minimums of the curvature of the Z_h profile below and above the peak's altitude (Baldini and Gorgucci, 2006).

7.3.1 – Stratiform events

During stratiform events, if the radar beam passes through the melting layer (see Sect. 4.2.3), radar overestimates rain in a range of distances which depends on the elevation angle. This range is relatively close to the radar location, where the effects of attenuation and range degradation are negligible. Vice versa, at farther distances, the probability that radar samples in a region above the precipitation or filled by ice particles increases, because of the radar beam propagation geometry. Furthermore, attenuation due to rain or to the presence of mixed phase in the melting layer reduces the signal power. As a consequence, prior to correction, radar tends to underestimates rainfall. It follows that two different *AF* behaviors could be recognizable when stratiform events occur. Thus, *AF* curves showed in Fig. 7.11 consist of two parts: a concave portion at closer ranges due to the presence of the bright band (where the lowest values are found), and an almost increasing linear one due to range errors. It must to be noted that the greater the elevation angle: (1) the lower the distance at which the radar beam intercepts the melting layer; (2) the shorter the path needed to the radar beam to pass through the melting layer, (3) the bigger the part sampled by the radar within the melting layer, and (4) the greater the slope of the second part of the curves, because the greater is the effect of range degradation. As a consequence, as the elevation angle increases the length of the concave part becomes shorter and the minimum value decreases and moves to the origin of the coordinate system, which corresponds to radar site. In Fig. 7.10 a schematization of VPR is showed, in which samplings are simulated with different elevation angles (in the figure are represented the corresponding radar beams). At each sampling, logarithm of G/R ratio curves (where G is the rainfall amount collected by the radar at the lower elevation) are obtained depending on the ground distance (right plot of Fig. 7.10). Trends of these curves confirm what has been said above.

Figures 7.11 and 7.15 also show the coefficient of determination R^2 concerning to the polynomial fit. R^2 increases as the accumulation time increases, according to what already has been said about Figs. 7.1, 7.2, 7.3, and 7.4. For each elevation angle, the high values of R^2 mean that the best fitting lines are very suitable to represent trend of $\log(G/R)$ (dB) as a function of range. There is also a substantial agreement between solid and dashed lines in both Figs. 7.11 and 7.15. Furthermore, the lightest grey curves in Fig. 7.11 do not show a concave part because the bright band is intercepted at a distance less than that between the first rain gauge and the radar.

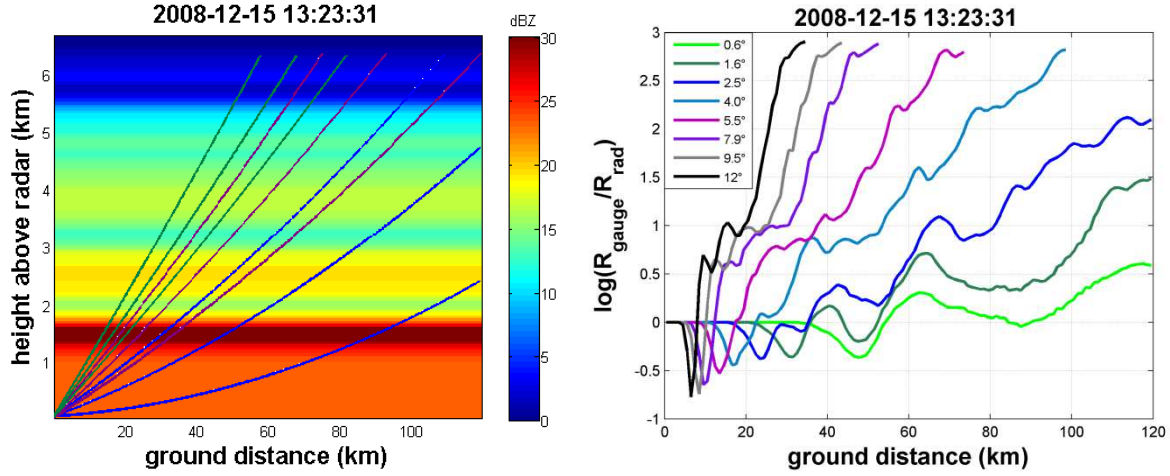

Figure 7.10 - VPR collected during the 15 December 2008 rainfall event and corresponding trends with distance from Polar 55C of log(G/R) obtained referring on different elevation angles ranging from 0.5 to 12°.

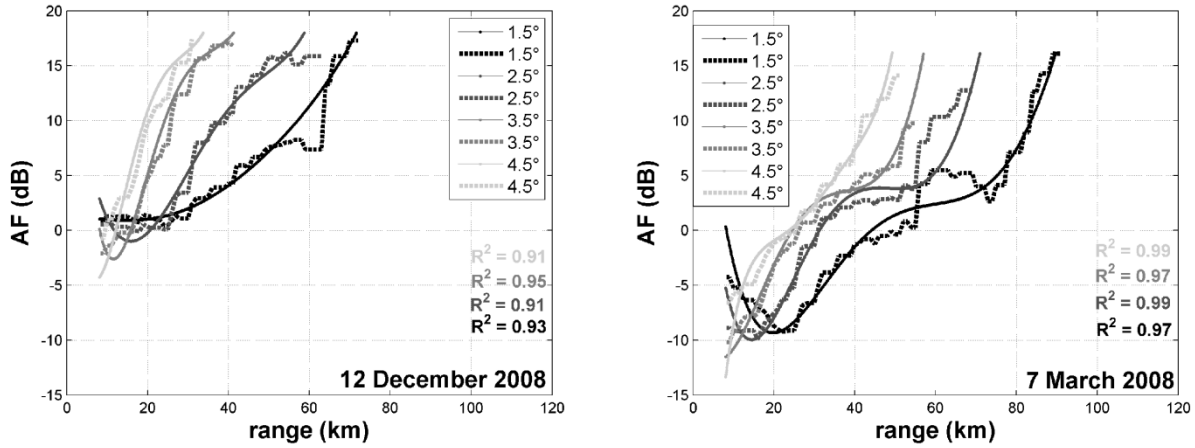

Figure 7.11 – *AF* computed for two stratiform cases, which are the 12 December 2008 and the 7 March 2008 events, from logarithm of *G*/*R* ratio trend with distance, by using both a polynomial fit of the fifth order (solid lines) and a method of moving averages with a window of 15 km (dashed curves).

The first considered event occurring on 7 March 2008 is a cool season wide spread stratiform precipitation system, which duration is of little more than 8 hours, from 7:40 am to 16:15 pm. Figure 7.12 shows rain rate (mm h^{-1}) maps obtained by converting reflectivity factor measured at different sweeps composing a volume scan at 10:55 a.m. The highest rain rate ring-shaped region showed by Fig. 7.12 indicate the bright band, which is situated inside a nearly uniform horizontally vertical structure of precipitation. Soundings collected by the Pratica di Mare show that freezing level is located at a height of 1070 m ASL at 10:55 a.m. Unfortunately, there are no Polar 55C observations collected at vertical antenna for this event. But, as already-mentioned above (see page 94), the freezing level height is located above the bright band, since below the freezing level is the melting layer. So, by observing right plot in Fig. 7.11, it can be found that

the ranges (which depend on the elevation) between which *AF* curves present their concavity upwards are consistent with the freezing level height.

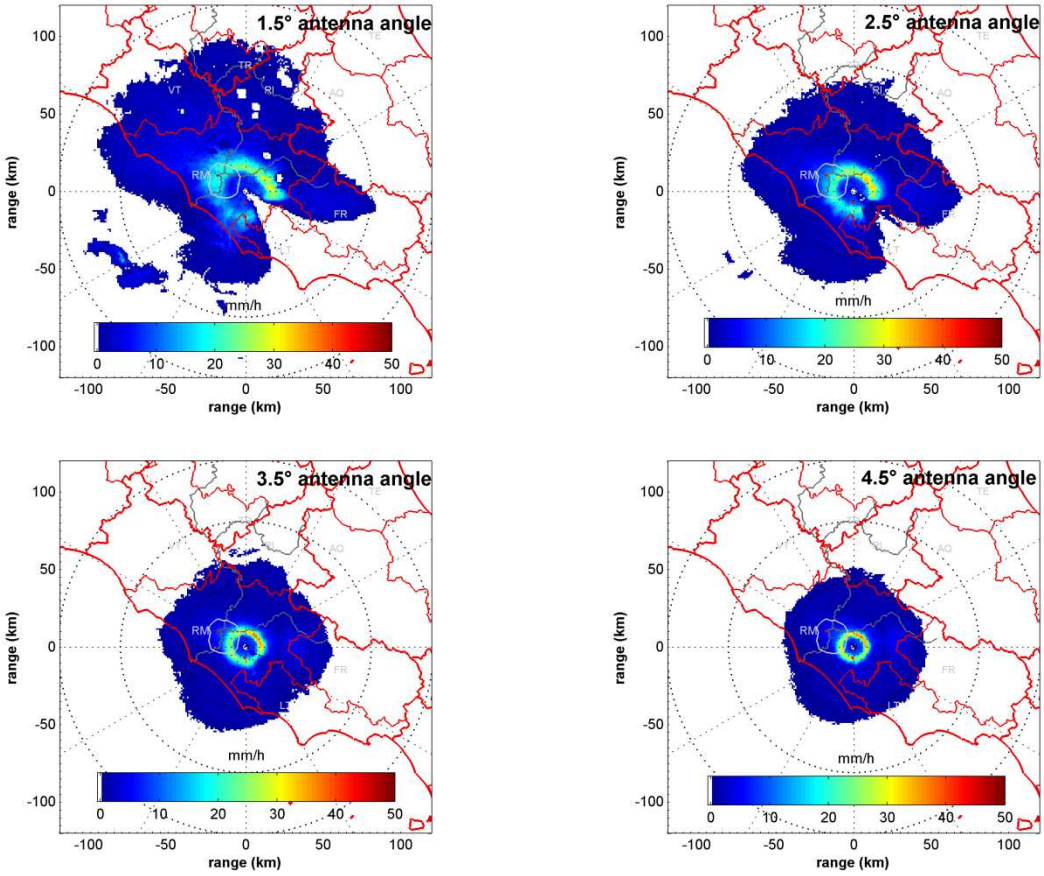

Figure 7.12 – Rain rate (mm h^{-1}) maps obtained during a volume scanning at 10:55 a.m. during the stratiform event of 7 March 2008.

The event occurring on 12 December 2008 is a cool season wide spread stratiform precipitation system lasting from midnight to 7:15 a.m. Figure 7.13 shows rain rate (mm h^{-1}) maps obtained by converting reflectivity factor measured at the different sweeps composing a volume scan at 3:10 a.m. As showed by this figure, the vertical structure of precipitation is nearly uniform horizontally, except for the highest rain rate ring-shaped region indicating the bright band. By comparing the rainfall maps in Fig. 7.13 with the corresponding curves in Fig. 7.11, it can be seen that the locations of the bright band with respect to the radar site closely correspond to the ranges where *AF* curves present their concavity upwards (regarded that Fig. 7.13 refers only to a PPI, whereas Fig. 7.11 to the whole event). Figure 7.14 shows the 0°C isothermal, located at a height of 1650 m ASL and the VPR, both referred to 3:10 a.m. Bright band is between 0.75 km and 1.3 km above the antenna.

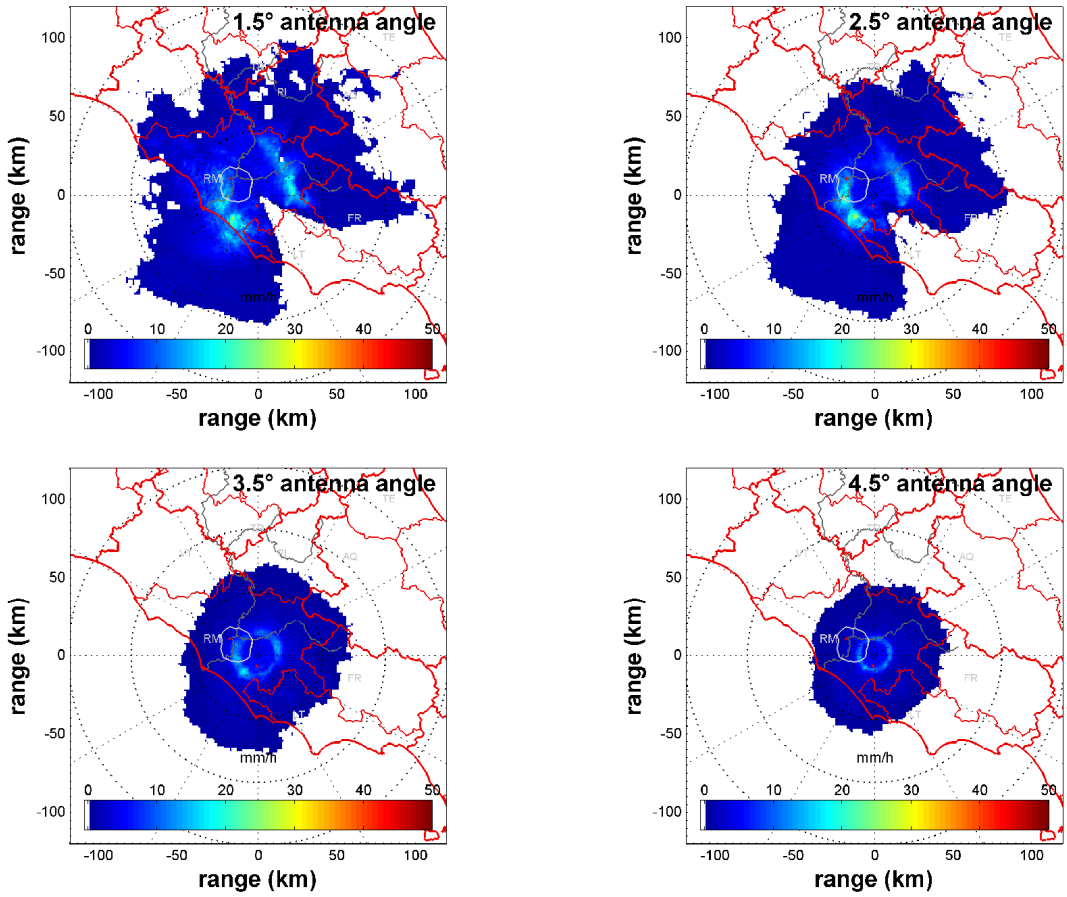

Figure 7.13 – Rain rate (mm h^{-1}) maps obtained during a volume scanning at 3:10 a.m. during the stratiform event of 12 December 2008.

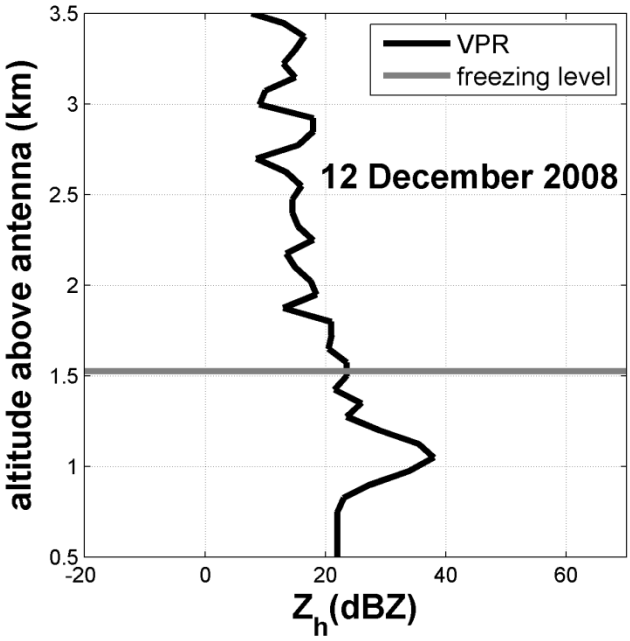

Figure 7.14 – Reflectivity trend with altitude (km) and 0°C isothermal height (with respect to the antenna) determined from soundings collected at Pratica di Mare at 3:10 a.m. both relative to the stratiform event of 12 December 2008.

When the antenna angle passes from 1.5 to 4.5° the distances in which the radar beam intercepts the melting layer calculated from the bright band bounds altitudes ranges from about 20 to 61 km, 14 to 35 km, 10 to 24 km, and 8 to 18 km, respectively. These ranges of distances correspond to the thickness of the reflectivity rings in Fig. 7.13.

7.3.2 – Convective events

Convective events here considered occur in the cold season as young cores of convective rain embedded inside a wide stratiform precipitation region, as above described. Depending on the vertical profile of temperature, stratiform part of precipitation could determine an occurrence of distinctive melting layer signature, as it happens in the cases in point. For these reasons, curves in Fig. 7.15 obtained for cold season convective events have trends qualitatively similar to those in Fig. 7.11, related to stratiform events.

However, by comparing plots of Figs. 7.11 and 7.15, it can be noted that, generally, *AF* curves length is greater for convective cases than for stratiform ones. This is due to the fact that radar can more easily sample above the stratiform precipitation, because the clouds top during stratiform events is lower than the cumulonimbus clouds top of convective events (Yuter and Houze, 1994; Steiner et al., 1995; Houze, 1997).

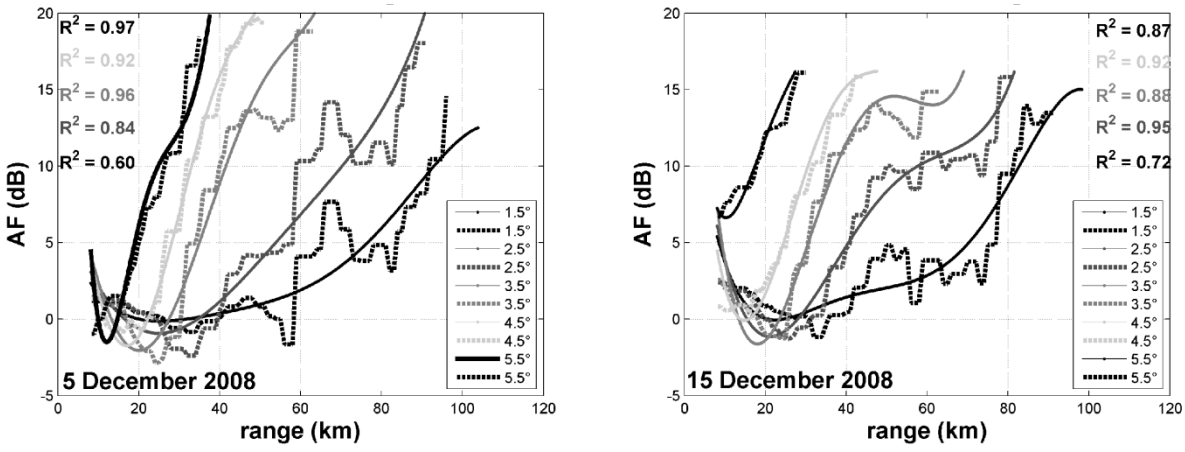

Figure 7.15 – *AF* computed for two convective cases, which are the 5 December 2008 and the 15 December 2008 events, from logarithm of *G*/*R* ratio trend with distance, by using both a polynomial fit of the fifth order (solid lines) and a method of moving averages with a window of 15 km (dashed curves).

Furthermore, the coordinates of the minimum point of concave part does not have a clear dependence on the elevation. Unlike the stratiform cases, as the elevation increases the ordinate can also increases. Instead, the abscissa becomes progressively smaller, as already showed for

stratiform cases, even if in some convective cases it slightly decreases, as it happens for the event of 15 December 2008. This is probably due to the fact that the stratiform part of the rainfall field is discontinuous and non-uniform in space. Similarly, the behavior of the minimum value depending on the antenna angle appears not so clear even in Fig. 6.7, because data utilized refer to both stratiform and convective events.

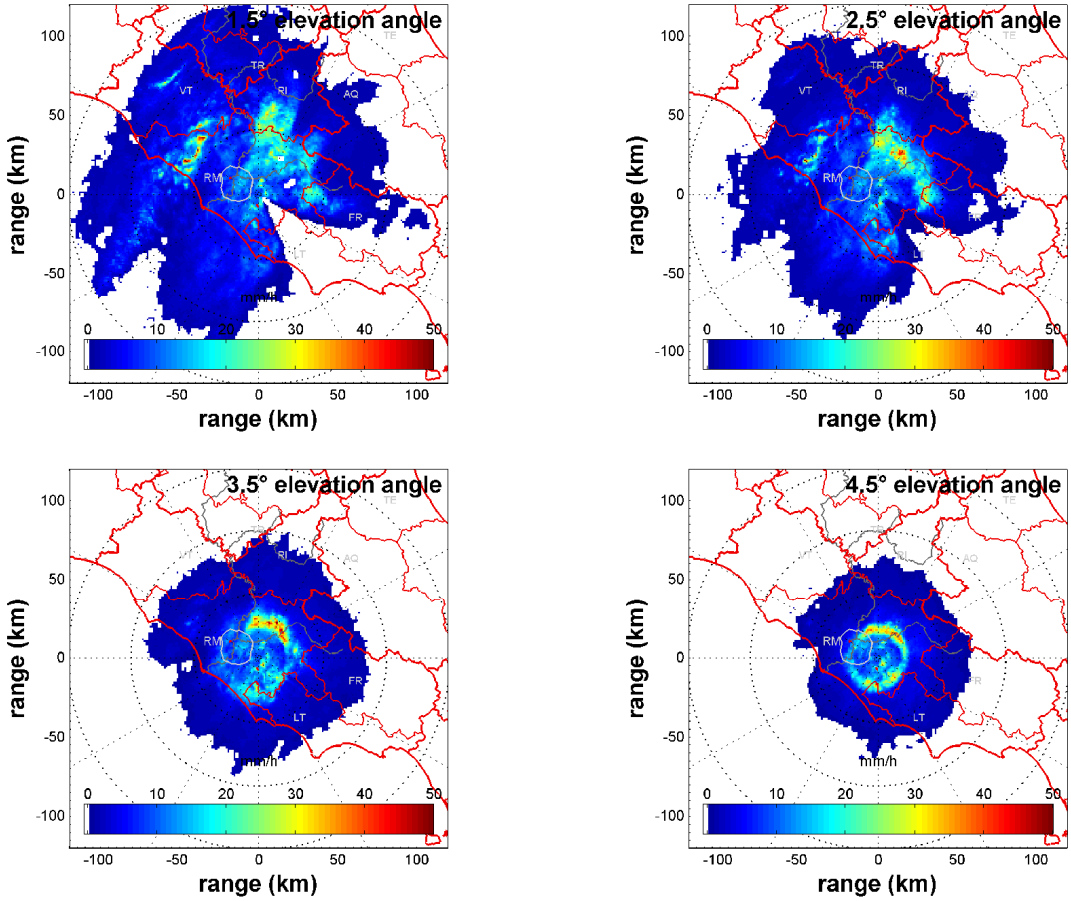

Figure 7.16 – Rain rate (mm h^{-1}) maps obtained during a volume scanning at 15:40 p.m. during the convective event of 5 December 2008.

The convective event occurring on 5 December 2008 has a length of 8 hours, from 10:00 a.m. to 18:00 p.m. The precipitation is formed by a convective part situated both to the north east and to the north west with respect to the Rome urban area, and convective cells are embedded in a larger stratiform precipitation region. By comparing each curve in Fig. 7.15 with the relative rainfall map (Fig. 7.16), it can be seen that the positions of the bright band with respect to the radar site roughly correspond to the ranges where *AF* curves present their concavity upwards. The freezing level is located at a height of 2055 m ASL at 15:40 p.m., which is the time corresponding to the PPIs in Fig. 7.16. The VPR collected at the same time by Polar 55C at

vertical antenna is represented in Fig. 7.17, together with the 0 °C isothermal height. The figure shows that the bright band is between 1.2 km and 1.9 km above the antenna. The distances where the radar beam intercepts the melting layer are calculated from the top and the bottom altitudes of the bright band. When the elevation angle moves from 1.5 to 4.5° they range from about 32 to 84 km, 22 to 50 km, 17 to 34 km, and 13 to 26 km, respectively, corresponding to the reflectivity rings thickness showed in Fig. 7.16.

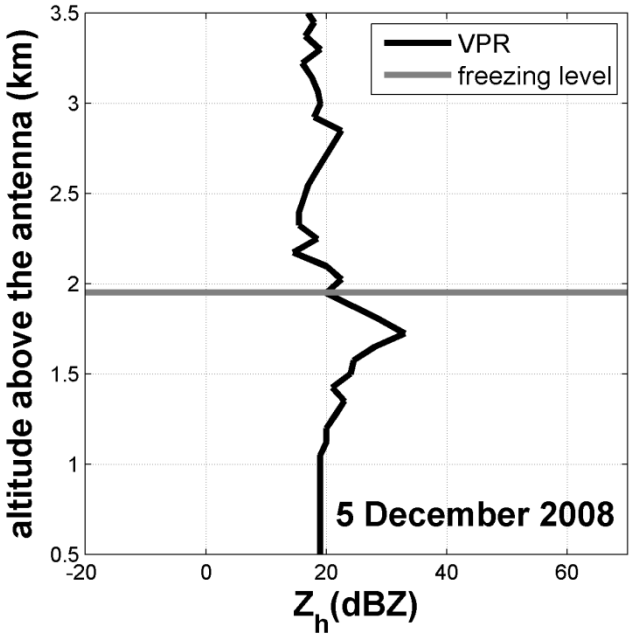

Figure 7.17 – Reflectivity trend with altitude (km) and 0°C isothermal height (with respect to the antenna) determined from soundings collected at Pratica di Mare at 15:40 p.m. both relative to the convective event of 5 December 2008.

The convective event occurring on 15 December 2008 has a length of 4 hours, from 9:40 am to 13:40 pm. Fig. 7.18 shows convective cells embedded in larger stratiform precipitation regions. Cells are located both to the north of Rome and above the coastline. But, when the radar beam passes through the stratiform field a bright band occurs, as it is showed by the last two plots in Fig. 7.18. By comparing each curve in Fig. 7.15 with the relative rainfall map (Fig. 7.18), it can be seen that the positions of the bright band with respect to the radar site roughly correspond to the ranges where *AF* curves present their concavity upwards. Pratica di Mare soundings show that freezing level is located at a height of 1958 m ASL at 13:30 p.m., which is the time corresponding to the PPIs in Fig. 7.18. Figure 7.19 shows the VPR collected at the same time by the Polar 55C and the 0 °C isothermal height. The figure shows that the bright band is located between about 1.3 km and 1.8 km above the antenna. As in the previous cases, the distances where the radar beam intercepts the melting layer are calculated from the top and the bottom

altitudes of the bright band. When the elevation angle moves from 1.5 to 4.5° they range from about 35 to 81 km, 24 to 47 km, 18 to 33 km, and 14 to 25 km, respectively, corresponding to the reflectivity rings thickness showed in Fig. 7.18.

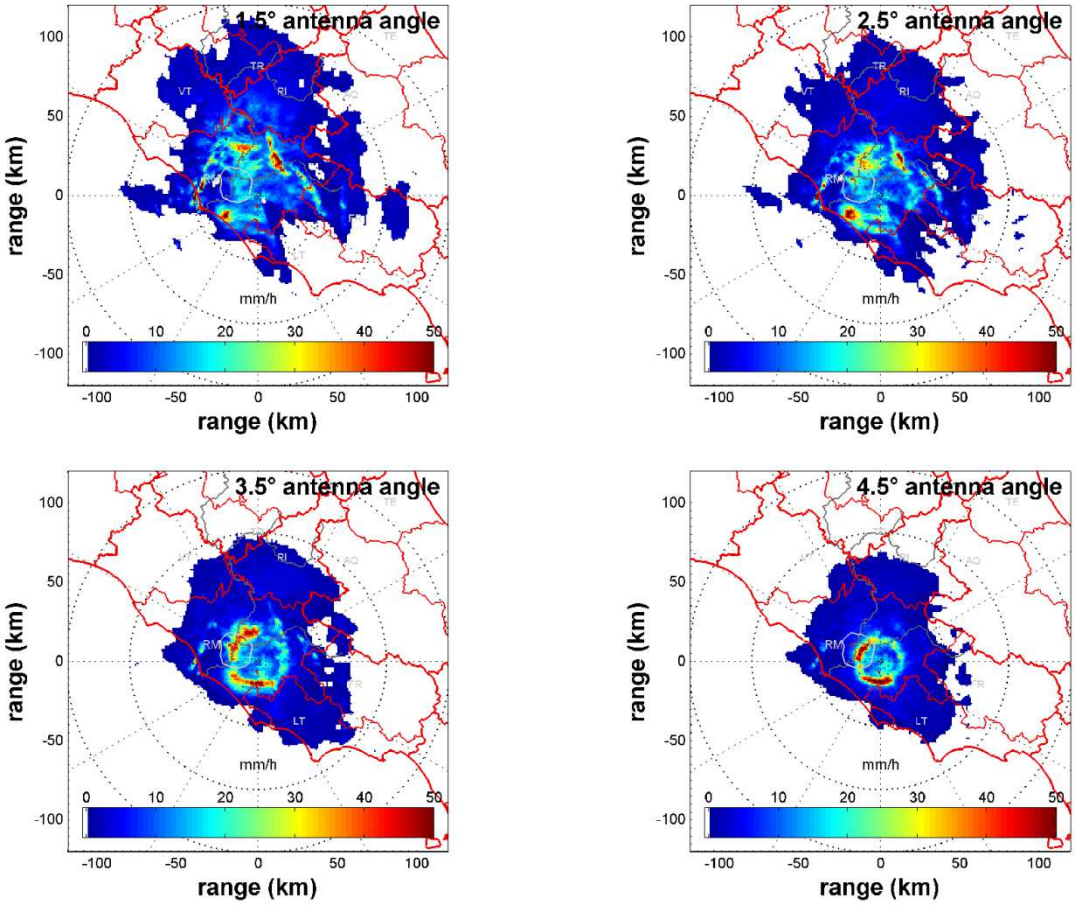

Figure 7.18 – Rain rate (mm h^{-1}) maps obtained during a volume scanning at 13:30 p.m. during the convective event of 15 December 2008.

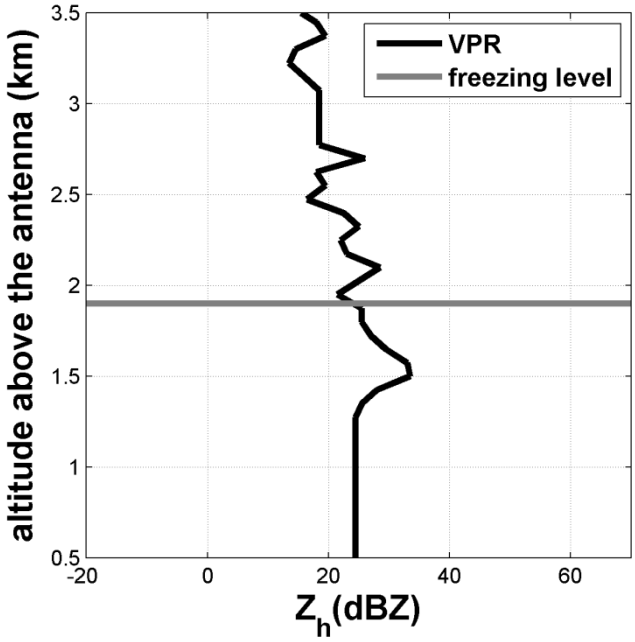

Figure 7.19 – Reflectivity trend with altitude (km) and 0°C isothermal height (with respect to the antenna) determined from soundings collected at Pratica di Mare at 13:30 p.m. both relative to the convective event of 15 December 2008.

7.3.3 – A global adjustment factor

The *AF* shows a trend with range that is qualitatively similar for events of the same category. However, at a given range there are significant quantitative differences between the values it assumes for events of the same type. So, there is not an univocal range error pattern at the scale of event. *AF* depends not only on the event type, being also a function of the spatial extension of the event, of the antenna elevation angle, of the vertical profile of temperature, and of the presence and characteristics of bright band. All these characteristics vary with time within the same event and would require a correction at very short time scales, if not in real time. Since our goal is long term rainfall amount quantification, *AF* has been evaluated as a function of corresponding radar and rain gauge annual rainfall amounts calculated at each rain gauge location, as showed in Eq. (6.1). Consequently, also the verification of the effectiveness of the proposed methodology is performed by calculating the annual rainfall amounts at each rain gauge location.

This choice is based on the observation that the *AF* tends to become gradually more stable with increasing accumulation time, at equal elevation angle, as can be observed from the figure below, which shows a substantial agreement between *AF* curves estimated for longer accumulation times.

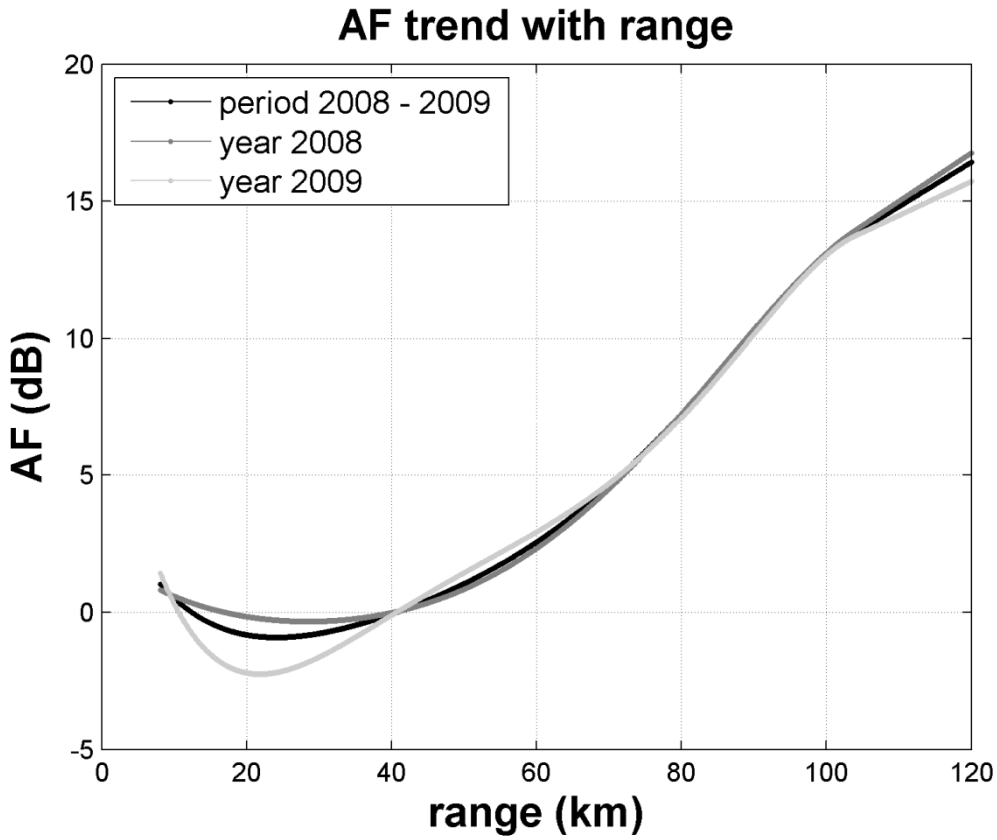

Figure 7.20 – *AF* trends with range evaluated for longer accumulation times (black, dark grey and light gray refer to 2008-2009 period, 2008 year, and 2009 year, respectively) and an elevation angle of 1.5°.

Therefore, at equal elevation, on the one hand the *AF* is extremely variable depending on the type of event (even among the same type), but on the other hand it tends to stabilize for large time aggregations order of one year or greater. As a consequence, the models proposed in Sects. 6.2 and 6.3 are suitable for applications that require long-term precipitation estimates, such as the quantitative estimation of precipitation necessary to evaluate the water budget of a basin, for water management or flood risk assessment.

Chapter 8

Conclusions

There are several error sources that influence the accuracy of rainfall estimates: error is expected, on average, to increase as the distance from radar increases. This work has characterized the overall radar error as a function of the distance from radar, to improve rainfall radar estimates in the absence of orographic effects. This technique, intended to quantify radar error, considers rain gauges direct rainfall measurements as “ground truth”. The proposed methodologies have been developed and evaluated using radar data sets of measurements collected by the Polar 55C radar located in Rome and data from the rain gauge network within the radar coverage. Areas where residual influence of ground clutter or beam-blocking can affect radar estimates are excluded, in order to address the error sources that can lead to characterization as a function of the distance from the radar.

To reach this objective, first a radar calibration with rain gauges is performed by choosing six rain gauges, whose distances from Polar 55C range from 15 to 20 km, and taking into account the visibility of the radar beam.

The *G/R* ratio between the rain gauges rainfall amounts and the respective radar rainfall amounts is then calculated as a function of range. Within the range of about 50 km *G*/*R* trend is influenced by the presence of the bright band, which causes a radar overestimation of rain. But, beyond this range, an approximately logarithmic trend against distance of *G/R* ratio occurs. A *G/R* logarithm trend best fitting line is used to defined an *AF* depending on the distance, which takes the overall radar error into account. *AF* trend with range is composed of a concave portion relative to less ranges and an about monotonically increasing for great distances.

A subsequent analysis is performed to highlight the effect of signal attenuation. In this case, correction of path attenuation is carried out before radar calibration, and the *AF* is evaluated for different antenna elevations.

Furthermore, the *AF* variability is investigated at the scale of event, both for convective and stratiform event. We found that *AF* trend for both categories of event is qualitatively similar. The minimum point of each curve tends to move towards the origin of the axes and the concave portion becomes less wide as the elevation angle increases. In addition, only for the stratiform cases, the minimum value decreases as the antenna elevation increases. The latter fact does not occur for convective cases because of the discontinuity of the bright band. Therefore, on the one

hand the model is extremely variable depending on the particular characteristics of the considered event. On the other hand, it tends to stabilize for large time aggregations order of one year or greater. As a consequence, radar data are corrected by means of the isotropic range dependent bias, *AF*, estimated by using data collected in 2008.

In a first analysis, radar calibration is performed using the 2008 radar data set without any correction. Whereas, the second analysis utilizes radar data obtained after correcting the path attenuation to perform calibration. Then, radar data are corrected by means of the isotropic range dependent bias, *AF*, estimated by using the 2008 calibrated radar data set. The verification of the adjustment procedure is carried out by considering both 2008 and 2009 radar data sets.

The behaviours of FSE index, slope of the scatter plots' regression lines and *G/R* ratio of rainfall time series pairs, obtained during 2008 or 2009 by Polar 55C and each rain gauge, are analysed as a function of distance to evaluate the adjustment procedure. The slope of the scatter plots' regression lines and the *G/R* ratio have the same trend against distance for each accumulation time. Before calibration, FSE reaches the maximum value (greater than 4) for distances where more frequently the radar beam intercepts melting layer. Similarly, the corresponding *G*/*R* and slope values reach a minimum value for the same distances. Then, FSE begins to decrease up to a value of 2 or less, whereas, *G*/*R* and slope begin to increase up to a value of 1 or more. After the adjustment procedure, all along the path the *G/R* ratio and the slope of the scatter plots regression lines are scattered about 1 and the FSE index gives the lowest values for each accumulation time, due to the reduction of the discrepancies between radar and rain gauge rainfall fields.

Instead, for the second methodology, events are selected so that the path from radar to the rain gauges is always located in a very intense rainy area. Moreover, only rain gauges approximately aligned along a radius are chosen, in order to emphasize the effects of the signal attenuation. After the adjustment procedure including path attenuation correction method, the *G*/*R* logarithm values are close to 0 all along the path, verifying the effectiveness of the methodology.

The proposed model is suitable for applications that require long-term quantitative precipitation estimates, such as the quantitative estimation of precipitation necessary to evaluate the water budget of a basin.

Bibliography

Amorocho J. and Wu B.: Mathematical models for the simulation of cyclonic storm sequences and precipitation fields, *J. Hydrol.*, 32, 329-345, 1977.

Atlas D. and Ulbrich C.W.: Path- and area-integrated rainfall measurement by microwave attenuation in 1-3 cm band, *J. Appl. Meteor.*, 16, 1322-1331, 1977.

Andrieu H., and Creutin J.D.: Identification profiles of radar reflectivity for hydrological applications using an inverse method. Part. I: formulation, *J. Appl. Meteor.*, 34, 225-239, 1995.

Andrieu H., Delrieu, G., and Creutin J.D.: Identification profiles of radar reflectivity for hydrological applications using an inverse method. Part. II: sensitivity analysis and case study, *J. Appl. Meteor.*, 34, 240-259, 1995.

Austin P.M. and Houze R.A. Jr.: Analysis of the structure of precipitation patterns in New England, *J. Appl. Meteor.*, 11, 926-935, 1972.

Baldini, L. and Gorgucci, E.: Identification of the Melting Layer through Dual-Polarization Radar Measurements at Vertical Incidence, *Journal of Atmospheric and Oceanic Technology* 23(6), 829-839, 2006.

Bacchi B. and Ranzi R.: On the derivation of the areal reduction factor of storms, *Atmos. Res.*, 42, 123–135, 1996.

Battan L. J.: Radarmeteorologia, Zanichelli publisher, Bologna, Italy, 1970.

Beard K. V. and Chuang C.: A new model for the equilibrium shape of raindrops, *J. Atmos.*, 44, 1509-1524, 1987.

Bechini, R., Baldini, L., and Chandrasekar, V.: Polarimetric radar observations in the ice region of precipitating clouds at C-band and X-band radar frequencies, *J. Appl. Meteorol. Clim.*, doi: 10.1175/JAMC-D-12-055.1, 2012, in press.

Berenguer, M. and Zawadzki, I.: A Study of the Error Covariance Matrix of Radar Rainfall Estimates in Stratiform Rain, *Weather Forecast.*, 23, 1085-1101, 2008.

Berenguer, M. and Zawadzki, I.: A Study of the Error Covariance Matrix of Radar Rainfall Estimates in Stratiform Rain. Part II: Scale Dependence, *Weather Forecast.*, 24, 800-811, 2009.

Bordoy, R., Bech, J., Rigo, T., and Pineda, N.: Analysis of a method for radar rainfall estimation considering the freezing level height, *Journal of Mediterranean Meteorology & Climatology*, 7 (25-39), 25-39, 2010.

Borga, M. and Tonelli, F.: Adjustment of range-dependent bias in radar rainfall estimates, *Phys. Chem. Earth*, 25 (10-12), 909-914, 2000.

Bringi V.N. and Chandrasekar V.: Polarimetric Doppler weather radar: principles andapplications, Cambridge University Press, 2001, 636 pp.

Calenda G. and Margaritora G.: Corso di Costruzioni Idrauliche, vol. I, EUROMA – Editrice Universitaria di Roma – La Goliardica, 1993.

Chow V.T., Maidment D.R., and Mays L.W.: Applied Hydrology, New York, McGraw-Hill, 1988.

Clothier, A. and Pegram, G.: Space-time modelling of rainfall using the String of beads model: integration of radar and raingauge data, Water Research Commission, WRC Report No. 1010/1/02, Durban, South Africa, 166 pp., 2002.

Delrieu, G., Braud, I., Berne, A., Borga, M., Buodevillain, B., Fabri, F., Freer, J., Gaume, E., Nakakita, E., Seed, A., Tabary, P., and Uijlenhoet, R.: Weather radar and hydrology, *Adv. Water Resour.*, 32 (7), 969-974, 2009.

Dirks, K. N., Hay, J. E., Stow, C. D., and Harris, D.: High-resolution studies of rainfall on Norfolk Island. Part II: Interpolation of rainfall data, *J. Hydrol.*, 208, 187-193, 1998.

Doviak R.J. and Zrnić D.S.: Doppler Radar and Weather Observations, Academic Press, 1993, 562 pp.

Eheret U.: Rainfall and flood nowcasting in small catchments using weather radar, PhD Thesis, University of Stuttgart, 2002.

Gabella, M. and Amitai, E.: Radar rainfall estimates in an Alpine environment using different gage-adjustment techniques, *Phys. Chem. Earth*, 25 (10-12), 927-931, 2000.

Gabella M., Joss J., Perona G., and Galli G., Accuracy of rainfall estimates by two radars in the same alpine environment using gage adjustment, *Journal of Geophysical Research,* 106(D6), 5139-5150, 2001.

Gans R.: Ube die form ultramikroskopischer goldteilchen, *Ann. Phys. (Leipzig),* 37, 881-900, 1912.

Gjertsen, U., Salek, M., and Michelson, D. B.: Gauge adjustment of radar-based precipitation estimates in Europe, in: Proceedings of the 3rd European Conference on Radar in Meteorology and Hydrology ERAD, Visby, Sweden, 6-10 September 2004, 7-11, 2004.

Goddard, J. W. F., Cherry, S. M., and Bringi V. N.: Comparison of dual-polarization radar measurements of rain with ground-based disdrometer measurements, *J. Appl. Meteor.,* 21, 252–256, 1982.

Gorgucci E., Scarchilli G. and Chandrasekar V.: Calibration of radars using polarimetric techniques, IEEE Trans. Geosci. Remote Sens., 30, 853-858, 1992.

Gorgucci E., Scarchilli G., and Chandrasekar V.: Radar and surface measurements of rainfall during CaPE, *J. Appl. Meteorol.,* 34, 1570– 1577, 1995.

Gorgucci E., Scarchilli G., and Chandrasekar V.: A procedure to calibrate multiparameter weather radar using properties of the rain medium, *IEEE Trans. Geosci. Remote Sens.*, 37, 269-276, 1999.

Gorgucci E., Baldini L. and Volpi A.: Polar 55C: an upgraded instrument for polarimetric radar research, Proceedings of the 2nd European Conference on Radar Meteorology ERAD, 18–23 November Delft, The Netherlands, 394–399, 2002.

Gorgucci E., Baldini L., and Chandrasekar V.: What Is the Shape of a Raindrop? An Answer from Radar Measurements, *J. Atmos. Sci.,* 63, 3033-3044, 2006.

Gorgucci E. and Baldini L.: Analysis of the mean raindrop shape model for dual polarization radar rainfall estimation, in: Proceedings of the Geoscience and Remote Sensing Symposium, 2009 IEEE International, IGARSS 2009 (Vol. 3, pp. III-113), Cape Town, 2009.

Green A.W.: An approximation for the shape of large raindrops, *J. Appl. Meteor.*, 14, 1578-1583, 1975.

Ha, E. and Yoo, C.: Use of mixed bivariate distributions for deriving inter-station correlation coefficients of rainfall, *Hydrol. Process.*, 21(22), 3078–3086, 2007.

Houze J.R.A.: Cloud Dynamics, Academic Press, 1993.

Houze J.R.A.: Stratiform Precipitation in Regions of Convection: A Meteorological Paradox?, *B. Am. Meteorol. Soc.*, 78(10), 2179-2196, 1997.

Jameson A.R.: Microphysical interpretation of multiparameter radar measurements in rain. Part III: Interpretation and measurement of propagation differential phase shift between orthogonal linear polarizations, *J. Atmos. Sci.*, 42, 607-614, 1985.

Kirstetter, P.E., Andrieu, H., Delrieu, G., and Boudevillain, B.: Identification of vertical profile of reflectivity for correction of volumetric radar data using rainfall classification, *J. Appl. Meteor. Climatol.*, 49, 2167-2180, 2010.

Koistinen, J. and Puhakka, T.: Can we calibrate radar with raingauges, *Geophysica*, 22 (1-2), 119-129, 1986.

Kottegoda, N. T. and Rosso, R.: Applied statistics for civil and environmental engineers, Blackwell Publishing, Oxford, UK, 2008.

Krajewski, W. F.: Rainfall estimation using weather radar and ground stations, in: Proceedings of the III Intemational Symposium on Weather Radars, San Paulo, Brazil, 1995.

Krajewski W.F. and Smith J.A.: Radar hydrology: rainfall estimation, *Advances in Water Resources*, 25(8-12), 1387–1394, 2002.

Krajewski, W.F., Vignal, B., Seo, B.C., and Villarini, G.: Statistical model of the range-dependent error in radar-rainfall estimates due to the vertical profile of reflectivity, *Journal of Hydrology*, 402, 306–316, 2011.

Ioannidis G.A. and Hammers D.E.: Optimum antenna polarizations for target discrimination in clutter, IEEE Trans. Antennas Propag., AP-27, 357-363, 1979.

Lombardo F., Napolitano F., Russo F., Scialanga G., Baldini L., and Gorgucci E.: Rainfall estimation and ground clutter rejection with dual polarization weather radar, *Adv. Geosci.*, 7, 127–130, 2006.

Lombardo F., Napolitano F., and Russo F.: On the use of radar reflectivity for estimation of the areal reduction factor, *Nat. Hazards Earth Syst. Sci.*, 6, 377-386, 2006.

Lombardo F.: Analisi e Modellazione della Distribuzione Spazio-Temporale della Precipitazione da Dati Radar, PhD Thesis, "Sapienza" University of Rome, 2007.

Lopez, V., Napolitano, F., and Russo, F.: Calibration of a rainfall run-off model using radar and raingauge data, *Adv. Geosci.*, 2, 41-46, doi: 10.5194/adgeo-2-41-2005, 2005.

Maheepala, U. K., Takyi, A. K., and Perera, B. J. C.: Hydrological data monitoring for urban stormwater drainage systems, *J. Hydrol.*, 245, 32-47, 2001.

Mittermaier M.P. and Illingworth A.J.: Comparison of model-derived and radar-observed freezing-level heights: implications for vertical reflectivity profile-correction schemes, *Q. J. R. Meteorol. Soc.*, 129, 83-95, 2003.

Moisello U.: Idrologia Tecnica, La Goliardica Pavese, 1999.

Ozturk, K. and Yilmazer, A. U.: Improving the accuracy of the radar rainfall estimates using gage adjustment techniques: Case study for west Anatolia, Turkey, *Atmos. Res.*, 86, 139-148, 2007.

Paoletti A. 1993: Effects of rainfall areal distribution on runoff volumes and peak flows, In Proceedings U.S.–Italy Bilateral Seminar, Water Resources Publications.

Peebles P.Z.: Radar Principles, Wiley-Interscience, 1998, 386 pp.

Pegram, G. and Clothier, A.: High resolution space-time modelling of rainfall: the “String of beads” model, Water Research Commission, Durban, South Africa, WRC Report No. 752/1/99, 115 pp.,1999.

Pegram, G.G.S.: Spatial interpolation and mapping of rainfall: 3. Optimal integration of rain gauge, radar & satellite-derived data in the production of daily rainfall maps, Progress report to the Water Research Commission, for the period April 2001 to March 2002 on contract K5/1153, 2002.

Pruppacher H. R. and Beard K. V.: A wind tunnel investigation of the internal circulation and shape of water drops falling at terminal velocity in air, *Quart. J. Roy. Meteor. Soc.*, 96, 247-256, 1970.

Rinehart R.E.: Radar for Meteorologists, Rinehart Publications, 1997, 428 pp.

Russo F.: Sull’uso dei campi di riflettività radar per la stima e la simulazione spazio-temporale della precipitazione, PhD Thesis, “Sapienza” University of Rome, 2004.

Russo F., Napolitano F., and Gorgucci E.: Monitoring systems over an urban area: the city of Rome, *Hydrol. Process.*,19(5), 1007-1019, 2005.

Russo F., Lombardo F., Napolitano F., and Gorgucci E.: Rainfall stochastic modelling for runoff forecasting, *Phys. Chem. Earth*, 31(18), 1252– 1261, 2006.

Saltikoff, E., Koistinen, J., and Hohti, H.: Experience of real time spatial adjustment of the *Z-R* relation according to water phase of hydrometeors, *Phys. Chem. Earth*, 25, 1017-1020, 2000.

Sauvageot H.: Radar meteorology, Artech House, 1992, 366 pp.

Scarchilli G., Gorgucci E., Chandrasekar V., and Dobaie A.: Self-consistency of polarization diversity measurement of rainfall, *IEEE Trans. Geosci. Remote Sens.*, 34, 22-26, 1996.

Sebastianelli S., Russo F., Napolitano F., and Baldini L.: On precipitation measurements collected by a weather radar and a rain gauge network, *Nat. Hazards Earth Syst. Sci.*, 13, 605-623, doi:10.5194/nhess-13-605-2013, 2013.

Seo D.J., Breidenbach, J., Fulton R., O'Bannon, T., and Miller D.: Real-time adjustment of range-dependent biases in WSR-88D rainfall estimates due to nonuniform vertical profile of reflectivity, *J. Hydrometeorol.*, 1, 222-240, 2000.

Sinclair, S. and Pegram, G.: Combining radar and rain gauge rainfall estimates using conditional merging, *Atmospheric Science Letters*, 6(1), 19-22, 2005.

Steiner M., Houze J.R.A., Yuter S.E.: Climatological characterization of three-dimensional storm structure from operational radar and rain gauge data, *J. Appl. Meteorol.*, 34, 1978– 2007, 1995.

Steiner, M., Smith, J. A., Burges, S. J., Alonso, C. V., and Darden, R. W.: Effect of bias adjustment and rain gauge data quality control on radar rainfall estimation, *Water Resour. Res.*, 35 (8), 2487-2503, 1999.

Testud J., Le Bouar E., Obligis E., and Ali-Mehenni M.: The rain profiling algorithm applied to polarimetric weather radar, *Journal of Atmospheric and Oceanic Technology*, 17, 332– 356, 2000.

Todini E.: The role of rainfall measurements and forecasts in real-time flood forecasting and management, In Proceedings of the III International Symposium on Weather Radars, San Paulo, Brazil, 1995.

Ulbrich C.W.: Natural variations in the analytical form of the raindrop-size distribution, *J. Climate Appl. Meteor.*, 22, 1764-1775, 1983.

Vaes, G., Willems, P., and Berlamont, J.: Rainfall input requirements for hydrological calculations, *Urban Water J.*, 3, 107-112, 2001.

Vignal, B., Andrieu, H., and Creutin, J.D.: Identification of vertical profile of reflectivity from volume scan radar data, *J. Appl. Meteorol.*, 38, 1214-1228, 1999.

Vignal, B., Galli, G., Joss, J., and Germann, U.: Three methods to determine profiles of reflectivity from volumetric radar data to correct precipitation estimates, *J. Appl. Meteorol.*, 39, 1715-1726, 2000.

Vignal, B. and Krajewski, W.F.: Large-sample evaluation of two methods to correct range-dependent error for WSR-88D rainfall estimates, *J. Hydrometeor.*, 2, 490-504, 2001.

Villarini, G., Mandapaka, P. V., Krajewski, W. F., and Moore, R. J.: Rainfall and sampling uncertainties: A rain gauge perspective, *J. Geophys. Res.*, 113, D11102, 2008a.

Villarini, G., Serinaldi, F., and Krajewski, W. F.: Modeling radar-rainfall estimation uncertainties using parametric and non-parametric approaches, *Adv. Water Resour.*, 31, 1674-1686, 2008b.

Villarini, G. and Krajewski, W. F.: Review of the different sources of uncertainty in single polarization radar-based estimates of rainfall, *Surv. Geophys.*, 31 (1), 107-129, 2010.

Wang, Y. and Chandrasekar, V.: Algorithm for estimation of the specific differential phase, *J. Atmos. Ocean. Tech.*, 26, 2565-2578, 2009.

Wilson J.W. and Brandes E.A.: Radar measurement of rainfall – A summary, *Bull. Amer. Meteor. Soc.*, 60, 1048-1058, 1979.

Yoo, C. and Ha, E.: Effect of zero measurements on the spatial correlation structure of rainfall, *Stoch. Env. Res. Risk. A.*, 21(3), 287-297, 2007.

Yuter S.E. and Houze J.R.A.: Three-dimensional kinematic and microphysical evolution of Florida cumulonimbus. Part. I: spatial distribution of updrafts, downdraft and precipitation, *Monhtly Weather Review*, 123, 1921-1940, 1994.

Zhang, J., Langston, C., and Howard, K.: Brightband identification based on vertical profiles of reflectivity from the WSR-88D, *J. Atmos. Ocean. Tech.*, 25, 1859-1872, 2008.

Zhang, J. and Qi, Y.: A real-time algorithm for the correction of brightband effects in radar-derived QPE, *J. Hydrometeor.*, 11, 1157-1171, 2010.

Zawadzki, I.: On radar-raingauge comparison, *J. Appl. Meteorol.*, 14, 1430-1436, 1975.

Zawadzki I.: Factors affecting the precision of radar measurements of rain, In *Preprints, 22nd Radar Meteorology Conference*, Boston, MA, American Meteorological Society, 251-256, 1984.